



University
of Glasgow

Humphreys, Mark (2019) *Real-time video rate terahertz digital holographic imaging system*. PhD thesis.

<http://theses.gla.ac.uk/75048/>

Copyright and moral rights for this work are retained by the author

A copy can be downloaded for personal non-commercial research or study, without prior permission or charge

This work cannot be reproduced or quoted extensively from without first obtaining permission in writing from the author

The content must not be changed in any way or sold commercially in any format or medium without the formal permission of the author

When referring to this work, full bibliographic details including the author, title, awarding institution and date of the thesis must be given

Enlighten: Theses

<https://theses.gla.ac.uk/>
research-enlighten@glasgow.ac.uk



University | School of
of Glasgow | Engineering

Real-Time Video Rate Terahertz Digital Holographic Imaging System

Mark Humphreys

Thesis for award of Doctor of Philosophy

Final Draft: September 2019

Supervisors: Prof David R.S. Cumming, Dr James P. Grant

Abstract

Terahertz (THz) radiation describes electromagnetic (EM) radiation with a frequency of between 0.1-10 THz. There has been widespread interest in THz imaging which has been demonstrated in numerous applications from medical to non-destructive evaluation (NDE) due to the unique properties of radiation at these wavelengths.

Current THz imaging systems suffer many drawbacks including the requirement of expensive components, slow imaging frame-rates and poor resolution.

In this thesis, a digital THz holography system is demonstrated which could offer a high-performance and potentially low-cost alternative.

The design and implementation of the first full video-rate (50 Hz) THz digital holography system is presented in this thesis. The system operates with coherent radiation of 2.52 THz (118.8 μm) and features low-cost optical components. The system's ability for imaging concealed objects is shown which suggests potential as a NDE tool. The potential to be used as a 3D depth imaging tool is also shown.

The publication relating to this work along with the movies and data-set can be found from the following reference along with in the thesis data-set:

M. Humphreys, J. Grant, I. Escorcia-Carranza, C. Accarino, M. Kenney, Y. Shah, K. Rew, and D. Cumming, "Video-rate terahertz digital holographic imaging system," *Opt. Express* 26, 25805-25813 (2018).

Acknowledgements

Finishing this PhD would never have been possible without the amazing amount of support and help I've been given.

Thank you to Prof David Cumming for giving me the opportunity and resources to do this.

My parents have always supported me and motivated me to do the best I can and to do the right things. Without their constant support and guidance, I would never be in such a privileged position as to complete this PhD. Any good I do come from them.

I'd like to thank my supervisors Dr James Grant and Dr Ivonne Escorcia-Carranza for everything they have done. Without them I would never have stayed the PhD. Their constant help, patience and belief in me allowed me to carry on until the end. They have been the biggest positive influences on my life over the past 3 years. They have been fantastic role-models and I hope I can become more like them, not just as an engineer/scientist but as a better person.

I am grateful for all of the academic support from my postdoc and PhD friends- particularly Dr Mitch Kenney, Dr Yash Shah and Claudio Accarino to name just a few. Their help has been invaluable

I am very grateful to my line manager Stuart Henderson at Leonardo for hiring me and giving me an opportunity to work in such a great environment. My colleagues Alison Lucie and Richard Hebb for helping me settle in, giving me help and advice. I'm especially grateful to my supervisor Dr Agata Pawlikowska for being such an excellent mentor, teaching me and being so kind and patient.

The personal growth I've experienced over these three years has been down to all of these people. The biggest thing I take from this experience is I no longer fear challenges- we can achieve anything if we really want it, just put the time in and it will come.

Thank you to the llamas of Peru



Table of Contents

<u>Section</u>	<u>Page</u>
Abstract	2
List of Figures	6
List of Tables	9
List of Abbreviations	10
1. Introduction	12
2. Terahertz Imaging Technology:	14
2.1 Terahertz Radiation and Applications	14
2.2 Terahertz Imaging Systems	21
2.3 Continuous-Wave Terahertz Sources	23
2.4 Terahertz Detectors	25
2.5 State of the Art Terahertz Imaging Systems	29
3. Background Theory of Light Waves and Holography:	34
3.1 Diffraction	34
3.2 Coherence	35
3.3 Holography	37
4. THz Digital Holography System Design	48
4.1 Terahertz Coherence	48
4.2 Terahertz Holography Laser Source	50
4.3 Terahertz Holography Detector Resolution and Choice	58
4.4 Terahertz Optical Components	63
4.5 Terahertz Holography System Set-Up	64
5. Terahertz Digital Holography System Performance	68
5.1 Recording an Interferogram	71
5.2 Reconstructing Holograms	75
5.3 Angular Spectrum Reconstruction	78
5.4 Performance	88
6. Real Time Reconstruction and Holography System Applications	94
6.1 Real-Time Video-Rate Terahertz Holography	94
6.1.1 Hologram Multiplexing Algorithm	95
6.1.2 Enhancing Performance with GPU	101
6.2 Terahertz Holography Application: Scanning Concealed Objects	104
6.3 THz Holography Application: 3D Depth Imaging	109
7. Conclusion	115
7.1 Summary of Thesis	115
7.2 Limitations and Possible Improvements	115
7.3 Further Work	118
	119

Appendices:	
Appendix 1.1: Matlab 1/e Divergence Beam Profile Code	119
Appendix 1.2: Matlab 1/e ² Divergence and Roundness Code	123
Appendix 2: UoG Fourier Hologram Sim Matlab Code	127
Appendix 3: Angular Spectrum Hologram Reconstruction Matlab Code	129
Appendix 4: Real Time Video-Rate Hologram Reconstruction Matlab Code	137
References	143

List of Figures

Figure	Page
Figure 1- General set-up of the THz holography system used in this thesis. Data read from FPA (detector) is read by computer and reconstructed into holographic image	13
Figure 2.1- Visualisation of the THz region of the EM spectrum, having wavelengths between IR and Microwave regions.	15
Figure 2.2- Images using THz radiation of rat burn with ‘+’ brand mark. Time after burn shown in red box in hours:minutes. After ~10 minutes the stasis damage becomes visible and ~7 hours the coagulation mark becomes clear (from [4]).	16
Figure 2.3- THz-TDS image of chocolate with defects hidden in polythene packaging illustrating THz use as NDE tool (from[10]).	18
Figure 2.4- (Left) Visible and (Right) image at EM frequency ~0.3 THz of concealed weapon hidden behind newspaper. The weapon is hidden in visible but the newspaper is transparent at 0.3 THz allowing the weapon (which is highly reflective at 0.3 THz) to be detected (from [15]).	19
Figure 2.5- General block diagram illustrating the difference between (a) an active imaging system- where a systems own source of illumination is used, and (b) a passive system where an external source is used and not needed within the system.	21
Figure 2.6- Commercially Available LWIR Microbolometer FPA camera. This model is a Xenics Gobi 640-CL and is designed for LWIR radiation of wavelengths 8-14 μm , but can also be used with THz radiation. This is the same camera model used for the THz holography system in this thesis (image from [53])	29
Figure 2.7- Thruvis TS4-C mm-Wave System demonstrating its stand-off detection capabilities for finding concealed weapons in a train station environment [image from 47]	30
Figure 2.8- I2s THz microbolometer FPA which features 320x256 pixels and is specifically designed for operation with THz radiation (image from [57])	32
Figure 3.1- Typical in-line (Gabor) arrangements to record a hologram using (a) transmission holography and (b) reflection holography setups where a photographic film is the recording medium	39
Figure 3.2- Typical arrangements to record a hologram using (a) off-axis reflection and (b) off-axis transmission holography setups where a photographic film is the recording medium	42
Figure 3.3- In-line THz holography setup for imaging hepatocellular carcinoma using an optically pumped gas laser and pyroelectric camera by Rong et al (image from [73])	45
Figure 3.4- Off-axis THz holography set-up with single pixel Schottky diode detector scanned to detect hologram as used by Heimbeck et al (image from [62])	46
Figure 4.1 – Ideal laser beam profile which shows a Gaussian distribution of intensity (image from [83])	53
Figure 4.2- Laser beam profile images recorded on LWIR microbolometer FPA showing (a) Best obtainable profile with TEM00 mode showing fairly round	55

profile and (b) a sub-optimal beam profile that has poor roundness and non-Gaussian distribution	
Figure 4.3- Beam Profiles from Figure 4.2 analysed with Matlab to find the roundness (0.98), and show (a) 1/e divergence=0.1 μ rad and (b) 1/e2 divergence=0.13 μ rad	57
Figure 4.4- Tydex HRFZ-Si beam-splitter reflection (green)/transmission (red) vs wavelength plot. There is 54/46% transmission/reflection at $\lambda=118.8 \mu\text{m}$ (image from [89])	64
Figure 4.5 - THz Holography Off-Axis Reflection Set-Up Chosen for the system where an optically pumped laser with $\lambda=118.8 \mu\text{m}$, an HRFZ-Si beam-splitter, planar silver mirror, and Xenics Gobi 640-CL FPA. Off-axis angle of $\theta=55.3^\circ$ and distance of $d=15\text{mm}$ between detector and sample were also chosen.	67
Figure 5.1- Off-Axis Reflection Mode Set-up for Digital THz holography as could be set-up on an optical bench with sample mounted on an x,y,z stage at a distance of $d=15\text{mm}$ from detector. An off-axis angle of $\theta=55.3^\circ$ between reference and object beam was used	70
Figure 5.2- CAD drawing of the aluminium sample object used in the THz holography experiments	71
Figure 5.3- Interferogram of ‘UoG’ sample object in reflection mode stitched from 2 interferograms to increase FoV. The fringes are caused by the interference between the object and reference beams.	75
Figure 5.4 – Fourier reconstruction of simulated hologram of ‘UoG’ sample showing the first order term (green circle top left), zero order mode (yellow circle centre) and second order mirror image (red circle bottom left).	77
Figure 5.5- FFT of Hologram and Reference Wave Product (1st order mode (green circle, top left), zero order (yellow circle, center)) and 2nd order mode term (red circle, bottom right right) for simulated hologram.	80
Figure 5.6- Filtered Wave-field of Object and Back-Propagation Kernel product for simulated hologram.	82
Figure 5.7- Angular Spectrum Reconstruction of Simulated Interferogram of ‘UoG’ object with features $< 1 \text{ mm}$ clearly resolved.	82
Figure 5.8- Angular Spectrum Hologram Reconstruction of Experimentally Obtained Hologram of ‘UoG’ sample with features $<1 \text{ mm}$ clearly resolved.	85
Figure 5.9- Comparison of Simulated (top) – Interferogram (left), Frequency Spectrum (mid) and Reconstruction (right). Experimental (bottom) – Interferogram (left), Frequency Spectrum (mid) and Reconstruction (right). Experimental data varies slightly from simulated due to combination of the laser beam not being fully Gaussian, noise from dead pixels and cross-talk and unwanted reflections at the detector.	86
Figure 5.10- Hologram with correct distance $z = 15 \text{ mm}$ (left) and incorrect distance $z = 10 \text{ mm}$ (right) illustrating the effect this has on focus.	87
Figure 5.11 - USAF Clear Path Target used to determine lateral resolution limit	88
Figure 5.12- Reconstructed hologram of USAF target (a) shows full target stitched together from 8 holograms (and featuring some unwanted stitching artefacts due to unstable laser) and (b) a zoom of highlighted region showing where a cross-section was taken for measurement.	90
Figure 5.13- Cross-section plot of USAF target from the region marked with dotted line in Figure 5.13 (b)	91
Figure 5.14- MTF of Holography System illustrating the system performance over range of spatial frequencies. Red dotted line gives the cut-off frequency 4	93

lines/mm equating to a lateral resolution limit of 250 μm	
Figure 6.1- Taking two frames (hologram 1 and 2) and multiplexing them together. (a) shows Hologram 1 and (b) the corresponding FFT. Hologram 2 is rotated 90° and shown in (c) along with the corresponding FFT (d).	97
Figure 6.2- FFT of multiplexed Hologram 1+ Hologram 2 (after it is rotated 90°)	98
Figure 6.3- Step by step guide of the hologram multiplexing algorithm as first conceived by Girshovitz [98] and used to speed up reconstruction speed in system by an order of magnitude.	100
Figure 6.4- Comparison of reconstruction algorithm speeds with no multiplexing (original hologram reconstruction method), multiplexing without a GPU, multiplexing with a GPU and multiplexing with a GPU reading straight from the frame-grabber (as would be done for real time imaging). The multiplexing algorithm makes it significantly more efficient than without and using this with a GPU gives a massive performance increase allowing the system to comfortably operate at 50 fps when reading from the frame-grabber in real-time.	103
Figure 6.5- Reconstruction of hologram of 'UoG' object concealed in polythene (top) and paper (bottom) packaging. Both of these materials are easy to detect the metallic sample object through	108
Figure 6.6- HRFZ-Si Wafer with 40 μm Deep Etched USAF Target Pattern where top image shows optical image of section, the middle id depth profile along x-axis (showing etch depth of 40.6956 μm) and the bottom showing depth profile along y-axis ((showing etch depth of 40.6828 μm)	111
Figure 6.7- optical image of USAF Target Section in (a), a surface profilometer image of the same section on HRFZ-Si etched target in (b) and phase reconstruction of the same section of an experimental hologram of the same 40 μm -deep etched HRFZ-Si target in (c)	113

List of Tables

Table	Page
Table 2.1- Comparison of THz Imaging Systems including frame-rate, lateral resolution and operating wavelengths. The mm-wave systems are in red boxes whilst the THz systems that can detect EM frequencies >0.7 THz are in green as this is the region of interest for the system in this thesis.	33
Table 4.1- comparison of QCL and optically pumped laser advantaged and disadvantages. Optically pumped provide higher power at the cost of stability whilst QCLs offer better stability at the cost of power.	52
Table 4.2- Comparison of Detector Performance of two different LWIR	61
Table 5.1- Summary of chosen THz holography system imaging parameters and performance	68
Table 6.1- Refractive indices and absorption co-efficient of materials over 2-10 THz range	105
Table 6.2- List of packaging materials tested with FTIR Spectrometer and corresponding transmission at 2.52 THz	106

List of Abbreviations

<u>Abbreviation</u>	<u>Meaning</u>
BS	Beam-Splitter
CAD	Computer Aided Drawing
CMOS	Complementary Metal Oxide Semiconductor
CONSORTIS	Concealed Object Stand-Off Real-Time Imaging for Security
CW	Continuous Wave
EM	Electro-Magnetic
F	Fourier Transform
FET	Field Effect Transistor
FFT	Fast Fourier Transform
FIR	Far Infrared
FMCW	Frequency Modulated Continuous-Wave
FoV	Field of View
FPA	Focal Plane Array
GaAs	Gallium Nitride
GaN	Gallium Arsenide
GPU	Graphics Processor Unit
HDPE	High Density Polyethylene
HRFZ-Si	High Resistivity Float Silicon
IR	Infrared
KID	Kinetic Inductance Detector
LDPE	Low Density Polyethylene
LWIR	Long Wave Infrared
M	Modulation
MT	Modular Transfer
MTF	Modular Transfer Function
NA	Numerical Aperture
NDE	Non-Destructive Evaluation
NEP	Noise Equivalent Power
NUC	Non-Uniformity Correction
OTF	Optical Transfer Function
PA-6	Polyamide-6
PM	Parabolic Mirror
PTD	Pulsed Time Domain
PTFE	Polytetrafluoroethylene
QCL	Quantum Cascade Laser
RADAR	Range Detection and Ranging
SBD	Schottky Barrier Diode

SNR	Signal to Noise Ratio
SWIR	Short Wave Infrared
TDS	Time Domain Spectroscopy
TEM	Transverse Mode of Electro-Magnetic Radiation
THz-TDS	THz Time Domain Spectroscopy
USAF	United States Air Force
UV	Ultra-Violet

1. Introduction

This thesis will discuss the development of a real-time video rate Terahertz (THz) holography imaging system.

In chapter 2, an overview of current THz imaging technology including a comparison of the state-of-the-art imaging systems is given. Chapter 3 explains the theory and concepts coherence and holography. In chapter 4, the choice of components and system design for the THz holography system are discussed. The implementation of the system is then described in chapter 45 along with choosing a reconstruction algorithm, analyzing the imaging performance and determining the lateral resolution of the system ($250\mu\text{m}$ or $\sim 2\lambda$). In chapter 6, the reconstruction algorithms and computing performance are improved in order to provide real time imaging at video rates (50Hz) along with demonstrating the systems suitability for remotely imaging concealed objects and for 3D depth measurement.

The general set-up for the THz holography system is shown below in Figure 1.

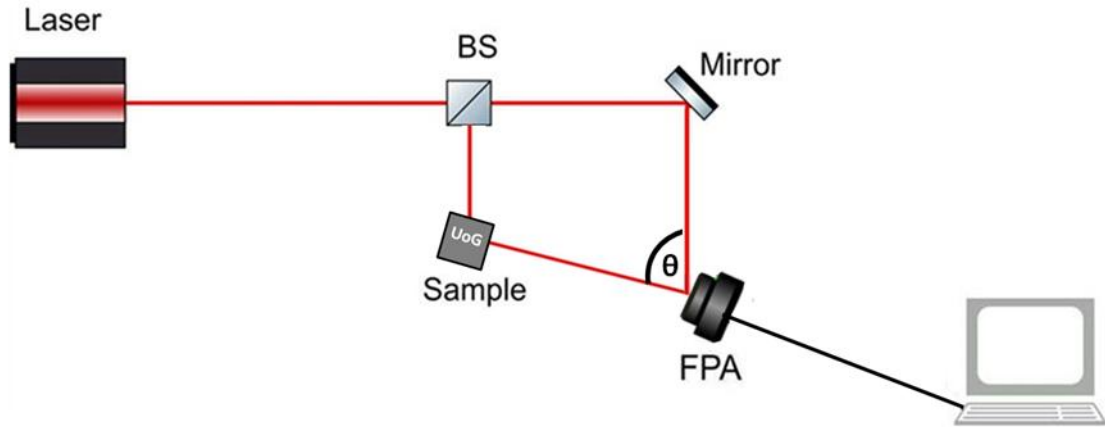


Figure 1 General set-up of the THz holography system used in this thesis. Data read from FPA (detector) is read by computer and reconstructed into holographic image

Here a laser source is used to output THz radiation which is split into 2 paths using a beam-splitter (BS). One of these paths goes to the detector (FPA) via a mirror whilst another reflects off a sample object and then recombines with the first laser beam path at the detector. The information from these 2 paths is then used by the detector and processed using a reconstruction algorithm which obtains a holographic image of the sample. The sample can be controlled using an electronic, motorized stage for scanning purposes and videos of real time reconstructed holograms as the sample is scanned along the x-axis are included in the thesis data-set.

2. Terahertz Imaging Technology

In this chapter, the definition of THz radiation is explained along with its applications. Current THz imaging technology is discussed along with the limitations affecting current THz imaging technology.

2.1 Terahertz Radiation and Applications

Terahertz (THz) radiation describes the region of the EM spectrum- between the infrared (IR) and microwave regions and is usually defined in literature as within the frequency range of 0.1 to 10 THz [1] as shown in Figure 2.1. Within this band, the THz band could be further separated into the frequency ranges of >0.7 THz which typically use optical imaging approaches similar to those employed in visible and IR bands, and frequencies lower than this which use approaches more commonly used in microwave imaging. The band of 0.1-0.7 THz is sometimes referred to as the ‘mm-wave’ band. Within the THz community, there is much debate over what is ‘truly’ THz and what can be thought of as ‘mm-wave’ approaches. For the purpose of this thesis, both will be discussed but the focus of interest will mostly be on radiation with frequencies >0.7 THz (specifically this thesis will be focusing on the development of an imaging system with EM radiation at ~ 2.52 THz).

THz radiation has become of widespread research interest over the past two decades due to its unique properties which have led to numerous applications in

biomedical imaging, non-destructive evaluation in quality control, agricultural, industrial and aerospace applications along with security applications [2].

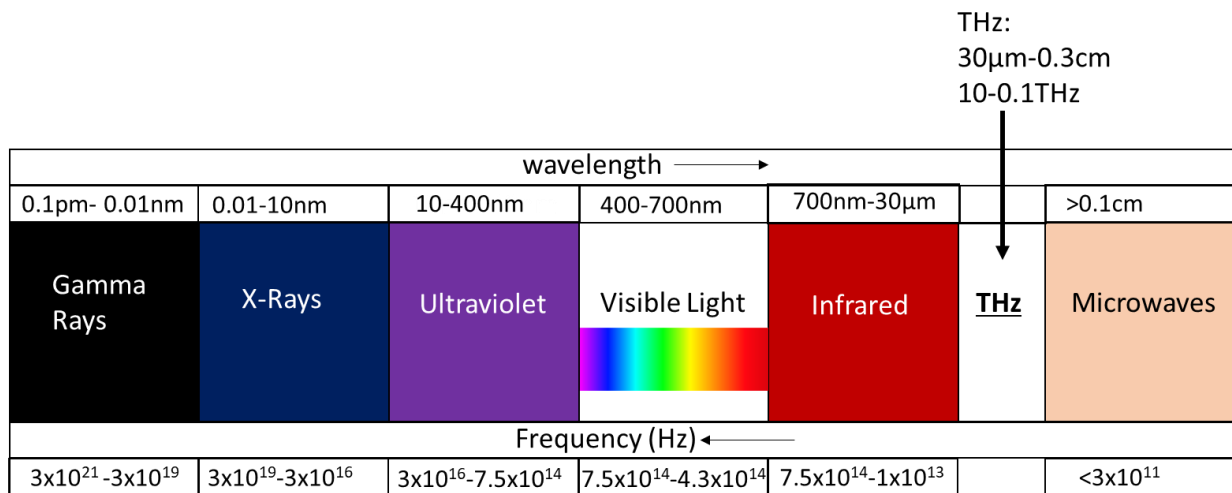


Figure 2.1- Visualisation of the THz region of the EM spectrum, having wavelengths between IR and Microwave regions.

The non-ionizing nature of THz radiation along with the longer wavelength compared to visible and IR allows for deeper penetration of skin and other tissue (such as liver) and make THz imaging a potentially safer alternative to x-rays (which over-exposure to can cause cancer) and other biomedical imaging techniques [3]. Measurements can be made remotely with no sample contact (unlike ultrasound) which can be of benefit when analysing patients with sensitive injuries.

One specific biomedical application that THz imaging is of high interest is in the analysis of skin burns. The penetration depth allowed by THz along with the high absorption by water in this band allow for burn wound detail when tested on rat skin burns [4]. Burn wound pathophysiology typically uses 3 wound regions - coagulation (irreversibly damaged), stasis (hyperhydrated

tissue) and hyperaemia (outer burn with hyperfused tissue) [5]. The amount of fluid changes over time which can help identify the three separate regions. This can be seen in Figure 2.2 where a cross mark is burnt into the abdomen skin of a rat and the THz response is shown over time.

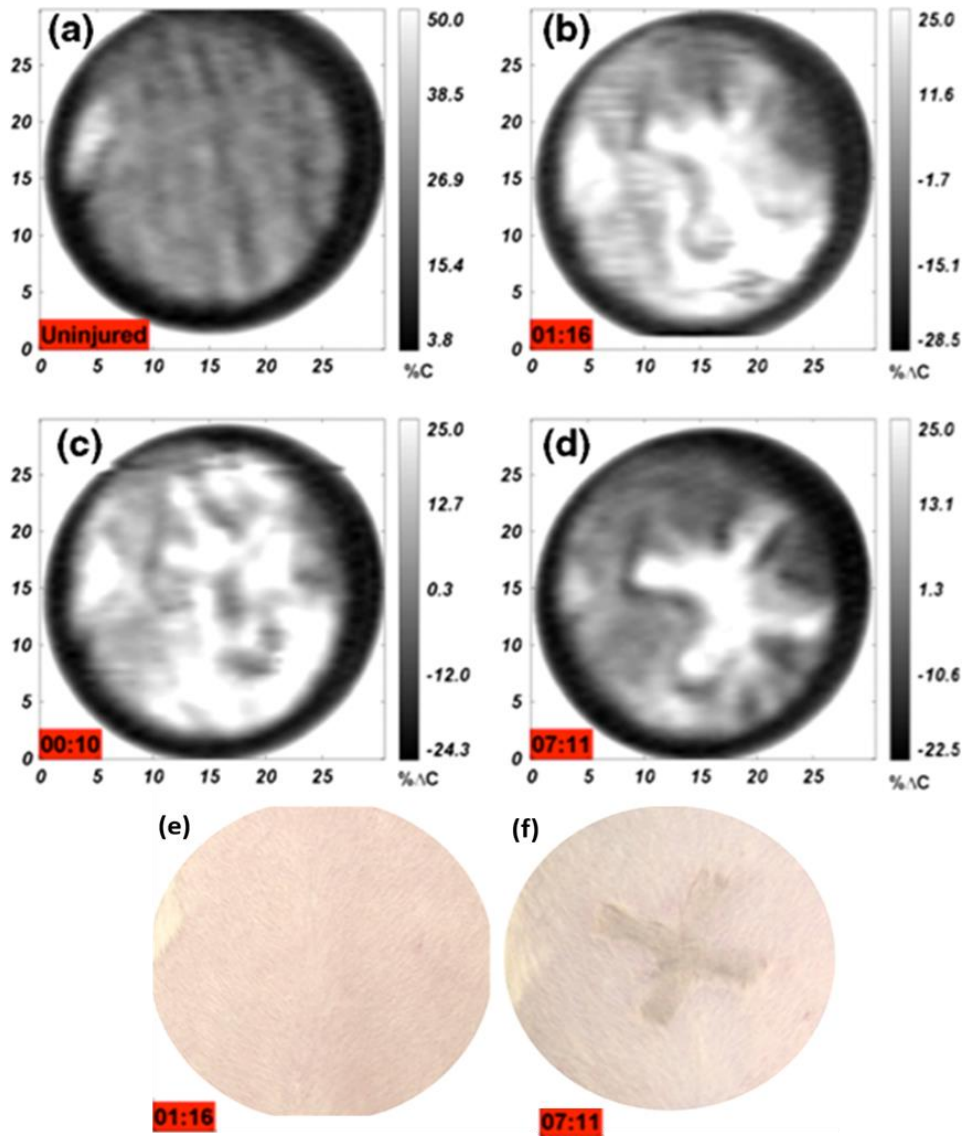


Figure 2.2- Images using THz radiation (a), (b), (c), (d) of rat burn with ‘+’ brand mark. Time after burn shown in the red box in hours:minutes. After ~10 minutes the stasis damage becomes visible and ~7 hours the coagulation mark becomes clear. The visible image of same sample shows no injury after 1 hour and only shows the coagulation mark after 7 hours. (Image from [4]).

It can be seen in Figure 2.2(b) and (c) that the stasis and hyperaemia regions are initially visible but in Figure 2.2(d), after 7 hours only the coagulation mark is present. This knowledge can be used by surgeons to recognise when to use and the extent to use skin grafts and other surgery. Dehydration dynamics studies using THz radiation have also been applied effectively to other types of biological tissue including meat samples to check for quality, freshness and health [6].

Another interesting use of the THz radiation's high water absorption properties has been in agriculture for the examination of crops. THz time-domain spectroscopy (THz-TDS) has been used to analyse the water content of plants in numerous studies [7-9]. This non-invasive procedure could potentially quickly analyse plant health, quality and check for optimal time for harvesting if commercialised.

Non-destructive evaluation (NDE) and quality checks can be performed through packaging materials that cannot be easily penetrated with shorter wavelength light. The longer wavelength of THz radiation (compared to visible and IR) allows transmission through most polymer packaging which allows remote sensing evaluation of quality of packaged goods. One good demonstration of the NDE potential of THz imaging has been in the use of quality testing packaged chocolate bars (in their polythene wrapping) for defects [10]. Contaminants including a glass splinter, stone and metal screw could clearly be identified within the packaged bar as shown in Figure 2.3 using a THz time domain spectroscopy approach (THz-TDS) with a pulsed femtosecond laser.

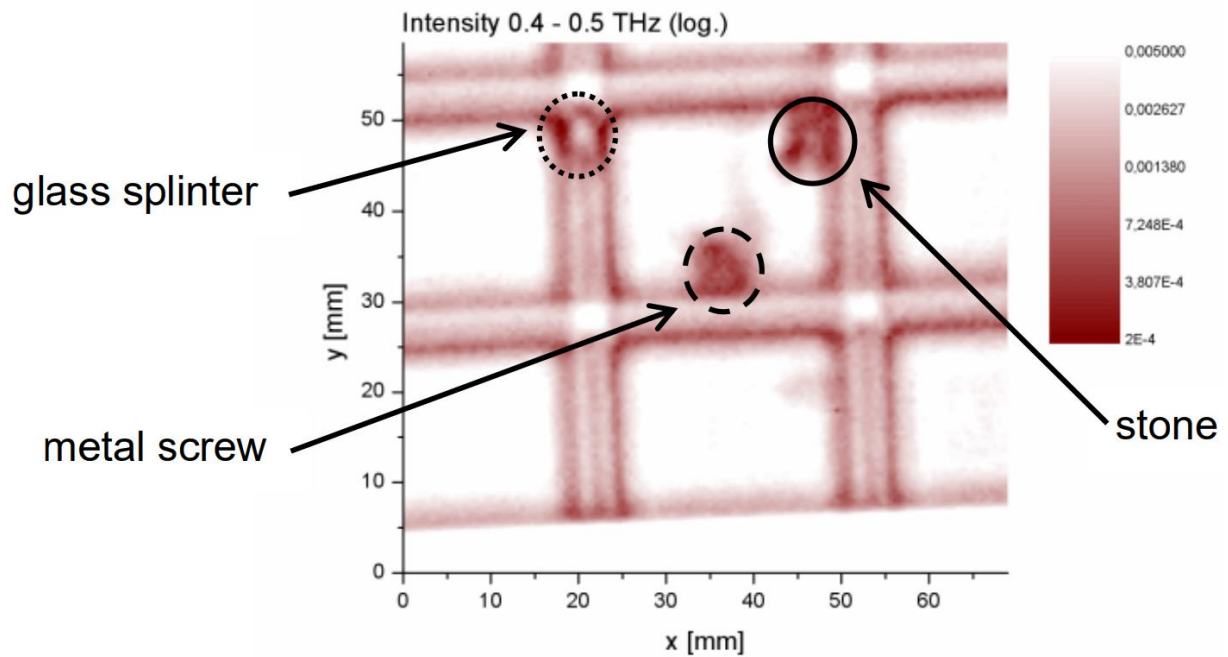


Figure 2.3- THz-TDS image of chocolate with defects hidden in polythene packaging illustrating THz radiation use as NDE tool (from[10]).

Other NDE applications include use as a package inspection tool (this particular application is later visited in the results chapters of this thesis), and for inspection of gas emission filters [11].

One of the most cited and interesting applications for THz imaging has been in the defence industry for security applications. The ability to penetrate through clothing and other materials to see concealed weapons has been one of the most sought-after applications, being successfully demonstrated several times [12, 13, 14, 15]. Figure 2.4 illustrates the potential benefit of THz imaging over visible for personal inspection. THz imaging for personal inspection is also much safer than alternative x-ray systems- especially when highly unstable weapons such as explosives are being identified [16].



Figure 2.4- (Left) Visible and (Right) image at EM frequency ~ 0.3 THz of concealed weapon hidden behind newspaper. The weapon is hidden in visible but the newspaper is transparent at 0.3 THz allowing the weapon (which is highly reflective at 0.3 THz) to be detected (from [15]).

Many explosives, drugs and other illicit materials also have spectroscopic fingerprints in the THz region making it possible to identify these using THz spectroscopy [16-18].

The examples described are some of the potential applications and benefits of using THz radiation for imaging and optical sensing over visible and IR radiation.

There are also many advantages to using THz radiation for some applications over longer wavelength radiation such as microwave. Some of these can come from the shorter wavelength allowing smaller features to be resolved (spatially) than in a conventional imaging system. In traditional cameras and optical systems, the theoretical limit for the smallest feature that can be resolved, is

called the diffraction limit (d). The most common criterion used to describe this is given by the Rayleigh criterion [19] and is given by Eq. 2.1:

$$d=0.61\lambda/NA \quad \text{(Eq. 2.1)}$$

where λ represents wavelength of radiation and NA is the numerical aperture (the range of angles the detector can view). By using a shorter wavelength, a better spatial resolution could be achieved without having to use a larger NA hence the shorter wavelength of THz radiation may allow for better resolution than microwave in conventional imaging system for some applications.

Although conventional diffraction limited imaging systems are still more common in THz and microwave technology, it must be noted there are now many ways to get beyond the diffraction limit such as super resolution microscopy, near-field imaging (when the sample being imaged is a distance of less than λ from the detector) or far-field techniques such as the STED microscopy [20-22]. However, these typically add significant constraints, or cost/complexity over traditional diffraction-limited systems which are still the most common type of imaging systems.

Another advantage of THz radiation is that the detectors typically use arrays of smaller size pixels which allows for the use of narrow laser beam sources if required, which can improve measurement repeatability [23].

THz frequencies also have the advantage over microwave frequencies of having a larger bandwidth (greater range of frequencies useable in a signal)- this allows for faster imaging (at the cost of some noise) which could potentially be very

useful for applications that require higher speed imaging than microwave approaches can achieve [24].

2.2 Terahertz Imaging Systems

Current terahertz imaging systems can broadly be grouped into two types - active imaging systems or passive imaging systems. Active systems have their own source of energy such as a laser to illuminate an object (or RADAR- radio detection and ranging), whereas passive systems use an external (usually naturally occurring) source such as the sun or blackbody object (an object that absorbs all radiation incident on it) [25]. This is demonstrated in Figure 2.5.

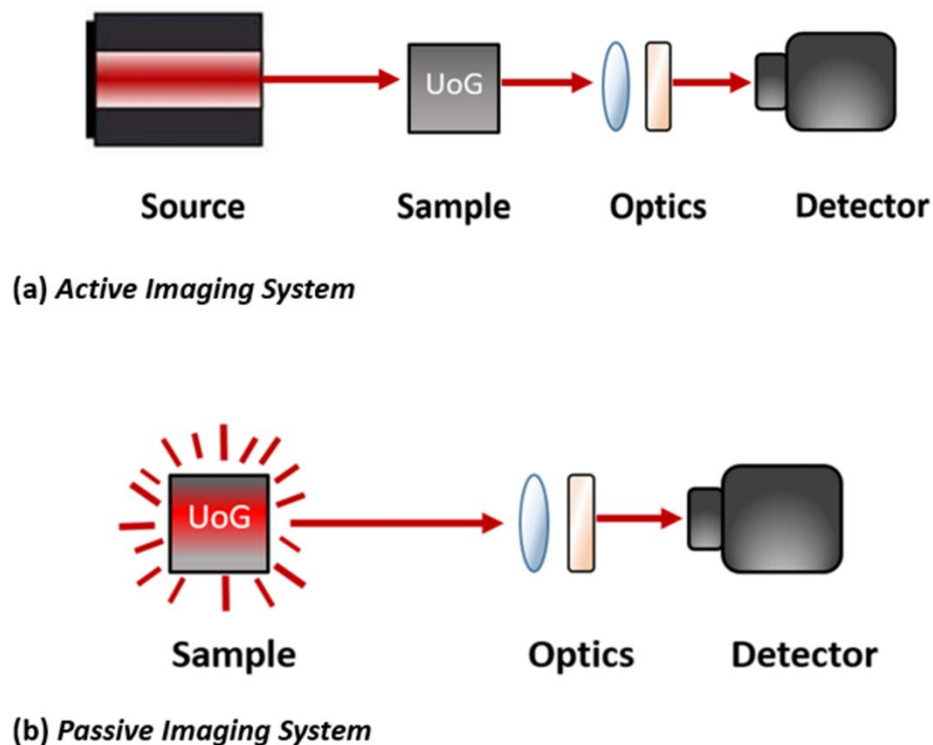


Figure 2.5- General block diagram illustrating the difference between (a) an active imaging system- where a systems own source of illumination is used, and (b) a passive system where an external source is used and not needed within the system.

Passive THz imaging systems are usually based around cryogenically cooled sensors at temperatures of 4K which can be very sensitive [26]. Such sensors have been successfully used in astronomical imaging where many stars emit spectral lines in the THz region that can be detected to give astronomers information about their physical properties [27]. Current passive THz imaging systems suffer from several problems that limit their applications- their large bulky size, high power requirements and expense due to the need to be constantly cryogenically cooled [28]. Uncooled passive THz systems are not very sensitive and struggle to differentiate between the sample being imaged and the background noise (very small dynamic range).

Active systems:

In active THz imaging systems a laser is the chosen type of source. There are two sub-categories of active THz imaging systems based on the type of laser being used- continuous wave (CW) and pulsed time domain (PTD) [29].

In PTD systems, very short (femtosecond) pulses are produced and directed in two separate paths - one to an antenna used to emit THz pulses that reflect off or transmit through a sample towards the detector. The other path from goes directly to the detector where it creates interference with the first path.

Changing the frequency of the pulses allows the THz wave to be scanned as a function of time and hence the frequency spectrum (and consequently transmission and reflection properties) can be obtained. This technique is known as THz time domain spectroscopy [30]. These types of systems are not used for real-time imaging and typically operate in the lower THz range (0.1-0.3 THz).

Continuous wave (CW) imaging systems are based on single frequency, coherent THz lasers and have the advantage of not requiring complicated optical systems or timing pulses. As the name suggests the laser output is continuous rather than pulsed. The laser radiation is transmitted through or reflected from a sample object and detected by a THz detector. These systems are typically used in the THz ranges >0.7 THz and may not require long imaging times depending on the type of detector being used.

2.3 Continuous-Wave THz Sources

When choosing a source for a THz imaging system, there are a number of key metrics that must be considered, especially as there is often a trade-off of one metric to optimize another. Firstly, the power needed must be sufficient to be detected, which can vary depending on the type of detector, sample, application and ranges being used. Many types of lasers also need to be cryogenically cooled which can potentially be expensive or impractical depending on size, weight, power or application needs. The stability of the laser (temporal coherence- or the ability to keep the same beam profile over a time period) and the beam quality (shape and uniformity) are also extremely important as these can drastically affect quality of images that may be obtained.

Quantum Cascade Lasers

The CW THz laser type with the highest future potential for compact, coherent imaging systems is the Quantum Cascade Laser (QCL). These are lasers built

around semiconductor devices where electrons recombine with holes and emit radiation depending on the material band-gap. To get around the small energy gap of THz wavelengths, QCL's use periodic layers of differing materials, which causes a periodic tunneling effect with the electrons and consequently emits THz photons.

Although THz QCLs have shown great potential for compact systems, the majority produce relatively low power. Recently improved QCLs can produce average power outputs of up to 4mW at room temperature [32]. This limits current applications of THz QCLs. Along with this issue, the majority are still cryogenically cooled which makes them bulkier and expensive to maintain. Recent advances have led to developments towards room temperature THz QCLs [33, 34], but these are not yet widely available.

Schottky Barrier Diodes

Schottky diode based frequency multipliers are another commonly used THz source [35]. This type of technology is built around the concept of heterodyne - mixing an input signal with a local oscillator signal to get a different frequency. GaAs Schottky Barrier Diodes (SBD) are used due to the high electron mobility in this material which causes the emission of THz radiation [36]. These types of sources produce a power output of around 240 μ W at frequencies <0.6 THz [37].

Optically Pumped Lasers

Optically pumped lasers are large lasers that usually consist of a gas pumped infrared (IR) laser and a Far-Infrared (FIR) vacuum chamber with gas molecules

that interact with the IR radiation resulting in the emission of THz radiation. A tunable, CO₂ pumped MIR laser is normally used (for its high power output in the 7-11 μm range) along with some mirrors for optical feedback and a coupling-hole into the FIR chamber. Inside the FIR chamber, the infrared photons with energies that match the molecular rotational state transition energies of the chosen molecule causes a population inversion resulting in the emission of THz photons [38]. The molecule chosen results in a different wavelength being emitted - for example methanol when pumped with the correct CO₂ laser line can produce an emission wavelength of 118.8 μm. Optically pumped lasers are a much more powerful source of THz radiation compared to the other sources mentioned- emitting up to 150 mW of power at THz wavelengths. They do have some drawbacks in that they can be unstable (the beam profile and power changes rapidly) and require a gas source which can limit practicality for portable applications.

2.4 Terahertz Detectors

There are many different types of detectors that have been utilized to detect THz radiation since the first photoconductor demonstrations by David Austin in 1984 [39]. As with THz sources, the detectors have a range of performance metrics that have to be considered when choosing the correct detector type for the system. These include the sensitivity of the detector at the wavelength of interest, the pixel pitch (distance between center of one pixel and center of adjacent), the number of pixels, response-time, frame-rate/operating speed and

whether they need to be cooled (usually adding extra size, weight and the requirement for cryogenic liquids such as liquid nitrogen). The importance of each metric varies depending on the application, for example when extremely high sensitivity is needed due to low powers from the source, but response-time is less important. Or for the THz holography system in this thesis, were a high powered laser is used (so a less sensitive detector could still be sufficient), but small pixel pitch, fast response times and fast frame-rates are required.

Schottky Barrier Diodes

Schottky diodes, which were previously discussed for their ability to emit THz radiation, can also be used as detectors. They are used with heterodyne receiver mixers and are most often used in applications in conjunction with a Schottky diode source - particularly for Fourier transform time domain spectroscopy [40]. They are potentially very useful because of their quick response times. However, their performance is very limited at frequencies > 0.7 THz.

Golay Cells

Another widely discussed type of detector is based around Golay cells. These are opto-acoustic sensors and are of particular interest in astronomical imaging. They operate using a sealed gas cell that expands and compresses a membrane when thermal energy from the THz radiation is applied - this can then be measured optically to get the response from the THz radiation [41]. Golay cell performance typically suffers from slow response times and are very sensitive to mechanical vibrations [42].

Pyroelectric Detectors

Pyroelectric detectors are a popular type of detector based around a crystalline material that produces an electrical response when thermally excited by EM radiation. It produces an AC signal which changes proportionally with temperature [43].

There are commercially available focal plane array (FPAs) pyroelectric THz cameras in the market with up to 160x160 pixels [44].

However, the detectors suffer from slow response times. The crystalline materials are also difficult and expensive to fabricate when integrating with CMOS circuits [45].

THz FETs

THz Field effect transistors (FETs) essentially act as a resonator that generate plasma waves when there is a fixed current in the FET channel, which generates THz radiation. This can be used in the opposite way where plasma waves in the channel respond to THz radiation and produce a current allowing for detection of THz radiation. This can be performed using silicon (Si) CMOS (complementary metal oxide semiconductor) based FETs [46] which have fast response times and high sensitivity.

These have advantages of being compatible with well-established CMOS Si processes allowing reduced costs and easy integration with current technology.

These can also be operated at room temperature [47].

This technology is still emerging and real-time operation is not yet achievable as large focal plane arrays (FPAs) with more than just a few pixels have not yet been developed.

THz detection has also been demonstrated using Gallium Arsenide (GaAs) and Gallium Nitride (GaN) FETs. These have advantages of extremely high sensitivity at high temperatures and broadband THz detection [48, 49]. Like Si CMOS FETs there are currently no large array GaAs or GaN FET FPAs available but the imaging technology is extremely promising.

Micro-bolometers

Micro-bolometers are perhaps the most promising THz detector for widespread use, of those currently available, due to their ease of integration with CMOS (complementary metal oxide semiconductor). Micro-bolometers are thermal detectors that convert thermal radiation to a change in resistance. The thermal response varies depending on the material used and frequency of radiation.

Although originally used in the LWIR band, they have been shown to be effective with THz radiation [50]. The two most commonly used materials for uncooled LWIR micro-bolometers are amorphous silicon (α -Si) and vanadium oxide (VO_x). The processing technology for these types of sensors is well established and focal plane arrays with large numbers of pixels and small pixel pitch are commercially available at relatively low-cost [51, 52]. Although they are fast and can be easily made into high resolution arrays, they suffer from lower sensitivity in the THz spectrum than other detectors. Figure 2.6 shows a commercially available LWIR microbolometer camera with 640x480 pixels.



Figure 2.6- Commercially Available LWIR Microbolometer FPA camera. This model is a Xenics Gobi 640-CL and is designed for LWIR radiation of wavelengths 8-14 μm , but can also be used with THz radiation. This is the same camera model used for the THz holography system in this thesis (image from [53])

2.5 State of the Art Terahertz Imaging Systems

There are currently several prominent THz imaging systems, both research laboratory based and commercially available. Many of these operate with EM radiation <0.7 THz. As mentioned at the beginning of the chapter, the work in this thesis will consider systems operating with EM radiation frequencies >0.7 THz as the THz frequencies of interest, and systems using lower frequencies as mm-wave imaging systems. It must be reiterated that there is some debate over what is actually THz and what is mm-wave, so systems using both will be mentioned. There are currently higher power sources available for mm-wave

radiation and this band is typically better applications like security screening people for concealed objects. However, some of the applications discussed earlier in this chapter (such as dehydration dynamics for biomedical and agricultural testing) are best achieved with radiation with frequencies > 0.7 THz.

There are a number of mm-wave systems used in security screening applications - in particular the commercially available Thruvision (UK), Safeview (USA) and the European research programme 'TeraScreen'. Thruvision systems are currently being used in several UK airports for quick and safe security screening [54]. An example of one of their products- the Thruvis TS4-C is shown below in Figure 2.7.



Figure 2.7- Thruvis TS4-C mm-Wave System demonstrating it's stand-off detection capabilities for finding concealed weapons in a train station environment [image from 47]

The concealed object stand-off real-time imaging for security (CONSORTIS) project is a system based around a large array of specially designed Kinetic Inductance Detector (KID) bolometers combined with a large optical element

[55]. It images with radiation of 0.34 THz with a lateral resolution of 10 mm. It has a relatively impressive frame-rate of 8 fps.

Looking at systems that image with radiation >0.7 THz it can be seen there are a number of limitations to their performance.

One of the most interesting systems is the Ohio State University developed heterostructure backward diode (HBD) FPA. This THz camera offers broadband (0.6-1.2 THz) THz imaging with high sensitivity. Currently only a 31x31 pixel FPA exists and frame-rate is limited to 5 fps.

Another interesting system is the Jet Propulsion Lab's frequency modulated continuous wave (FMCW) radar imaging system. This operates with EM frequency of 0.675 THz and has successfully demonstrated the ability to identify concealed weapons behind clothing. This technique has a relatively large lateral resolution (the smallest feature size in the x-y plane that may be resolved), of 10 mm so is not suitable for imaging very small objects. It has an array of 100x100 pixels and can image at a frame rate of 1 fps.

Researchers at Johann Wolfgang Goethe university were able to successfully implement a THz imaging system at 0.645 THz using a transceiver and optical arrangement. The transceiver array is capable of taking an image every 9s and can resolve objects as small as 15 mm.

Perhaps the closest to the 'gold standard' THz imaging system for > 0.7 THz is the commercially available i2s THz camera, which is based on an uncooled microbolometer array. This impressive FPA can be used from 0.1-10 THz with its

320x240 pixels and can achieve a lateral resolution of around 0.2 mm [56].

These cameras are inherently expensive (>\$100k with lens) and have frame-rates of 25 fps which is bordering video rate. Figure 2.8 shows the i2s camera.



Figure 2.8- I2s THz microbolometer FPA which features 320x256 pixels and is specifically designed for operation with THz radiation (image from [57])

A comparison of these mm-wave and THz systems is shown in table 2.1 with mm-wave systems in red and THz systems in green. As mentioned before, it is not fair to compare the mm-wave systems with THz as they both utilize very different methods, with THz systems behaving more like visible or infrared optical systems and mm-wave more like microwave radar systems. The digital holography system proposed in this thesis is also shown in comparison to these other systems in table 2.1.

System	Radiation frequency	Lateral Resolution	Frame-Rate	Cost
Jet Propulsion Lab	0.675THz	10mm	1Hz	N/A (research funded project)
Wolfgang	0.3-645THz	15mm	1 every 9s	N/A ()
Consortis	0.34THz	10mm	0.125s (8Hz)	N/A
Ohio State	0.6-1.2THz	1mm	5Hz	N/A (prototype)
I2S	0.1-10THz	~0.2mm	25fps	\$110k +source
THz Holography System Proposed	2.5THz	~0.2mm	50fps	~£12k +source (\$40-100k)

Table 2.1- Comparison of THz Imaging Systems including frame-rate, lateral resolution and operating wavelengths. The mm-wave systems are in red boxes whilst the THz systems that can detect EM frequencies >0.7 THz are in green as this is the region of interest for the system in this thesis.

3. Background Theory of Light Waves and Holography

In order to understand the concepts of holography, it is first necessary to understand the concepts of diffraction and coherence.

3.1 Diffraction

Two of the most important phenomena when studying the behaviour of light waves are diffraction and interference. In general diffraction is used to describe when light deviates from the original path it was travelling by interactions with objects or openings, or change of media it is travelling in, which slows the light wave down and causes bending effects [58]. This can be seen when light bends around corners.

Interference is described as two separate waves superimposing and creating dark and light fringes as they interfere constructively and destructively together [59].

When there are just two or three sources of waves interfering- interference is usually used. Contrarily if there are a larger number of sources, diffraction is usually used [60].

In this thesis, when discussing holography, interference will be used to describe the interactions between the two source waves, whereas diffraction will be used

to discuss the interactions and patterns produced from objects combining with waves.

Typically, diffraction patterns are described as one of two types- Fraunhofer or Fresnel diffraction. The type of diffraction pattern is affected by the distance between the object causing the diffraction and the detector or screen showing the pattern. If the distance is long or a lens is used to focus the light waves, a far-field or Fraunhofer diffraction pattern is created. Contrarily if no lens and a short distance is used, near-field or Fresnel diffraction takes place [61].

Numerically, if the distance from the source to the aperture/object with slits **and** the distance from object to detector is greater than the length f shown in Eq. 3.1 (where A =aperture area or size of slits and λ =wavelength of light), Fraunhofer diffraction takes place. Otherwise a Fresnel diffraction pattern will be created.

$$F \sim A/\lambda \quad \text{(Eq. 3.1)}$$

The most commonly used lens-less holography techniques typically create Fresnel patterns [62].

3.2 Coherence

The most fundamental requirement for holography is the need for coherence- the phase difference between waves must be constant in order to create interference [63]. Diffraction with an incoherent source may be observed where the patterns are average or gradient patterns. However, forming interference patterns with

an incoherent source (where the phase is not constant), is not possible- this is why interference is used to measure coherence [64].

To better understand the importance of coherence it's best to start with two waves:

the object wave U in the x and y plane at time t , defined in Eq. 3.2(a).

$$U(x,y,t) = |U(x,y,t)| \cdot Re[exp(i\theta U(x,y,t))] \quad \text{(Eq. 3.2a)}$$

the reference wave R in the x and y plane at time t , defined in Eq. 3.2(b).

$$R(x,y,t) = |R(x,y,t)| \cdot Re[exp(i\theta R(x,y,t))] \quad \text{(Eq. 3.2b)}$$

As these waves are both essentially spherical, assuming that these waves interfere at the same position for x , y and t , then the intensity distribution $I(x,y,t)$ recorded will be given from Eq. 3.2(c)

$$I(x,y,t) = |U(x,y,t)+R(x,y,t)|^2 \quad \text{(Eq. 3.2b)}$$

This can then be expanded to give the equation for an interferogram $I(x,y,t)$ shown in Eq. 3.3.

$$I(x,y,t) = |U(x,y,t)|^2 + |R(x,y,t)|^2 \dots \\ + 2 |U(x,y,t)| |R(x,y,t)| \cdot Re\{exp[i(\theta U(x,y,t)-(\theta R(x,y,t))]\} \quad \text{(Eq. 3.3)}$$

The concept of holography relies on creating an interferogram like this where the object wave will transmit or reflect from the target of interest whilst the reference wave is used to obtain the phase difference caused by the target.

The third term of the interferogram in Eq. 3.3 helps explain the effect of coherence and importance of remaining in phase to maximise the

intensity/contrast in the interferogram. The coherence is usually described as two effects- temporal and spatial.

Temporal Coherence

This describes the correlation of interfering waves in space at various times- for a time period τ (the coherence time), a radiation source is described as temporally coherent if the phase difference between waves remains constant (no random phase shifts). Using a larger time period than the coherence length results in a (usually undesirable) variable phase difference.

Spatial Coherence

Unlike temporal coherence, the spatial coherence describes the difference in spatial distance (in the x and y planes) observed at laterally spaced points. It is dependent on the separation d between points of the wave (d cannot be smaller than the wavelength), the distance R from the source to these points and the shape/size of the source. The separation d is the same as the separation between slits in Young's double slits experiment [65].

3.3 Holography

Holography describes the method created by Denis Gabor [66] that is used to obtain a wave-front containing amplitude and phase information from the diffraction pattern of a sample object. Since the wave-front contains the amplitude and phase information from the object, it is possible to obtain a full

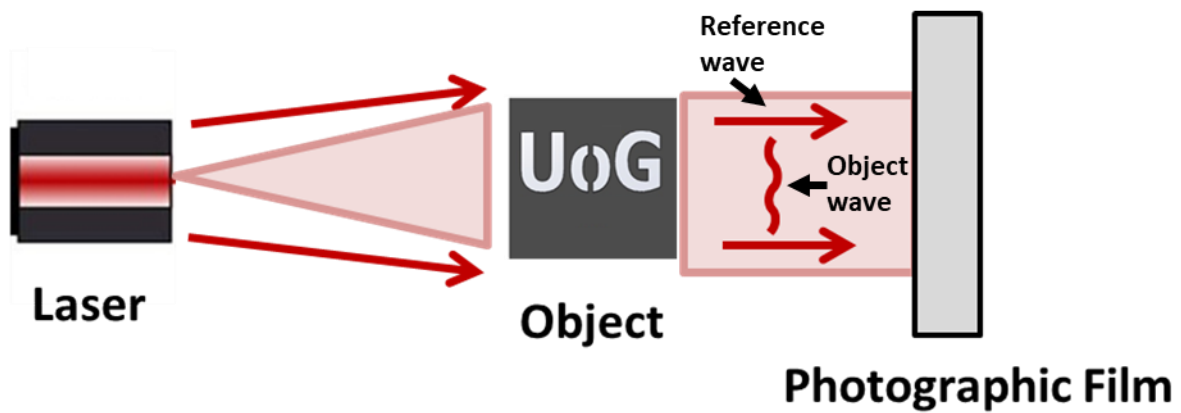
image of the object without the use of lenses. This can be very convenient when wanting to make compact, minimised systems or have a wide field of view (FOV).

This is done through obtaining the superimposed interference pattern created from a coherent source (an interferogram) where some of the radiation reflects or transmits from the sample object (object beam) and another part from the same source combines with this at the recording plane (reference wave). In analogue holography this would mean the two beams meeting at the photographic film or other recording media. This recorded interference pattern (or interferogram) contains the hologram. By illuminating the interference pattern using the same coherent source, a hologram is 'reconstructed' meaning it displays the wave-front from the object, giving a full image of the sample object. This means detailed images containing phase (allowing for 3D depth information) and amplitude may be obtained from the diffraction pattern rather than from using lenses to focus light down to a spot as in conventional lens imaging. Holography is therefore a two-step process- recording a hologram (or interferogram) and reconstructing this pattern to obtain the object image [67].

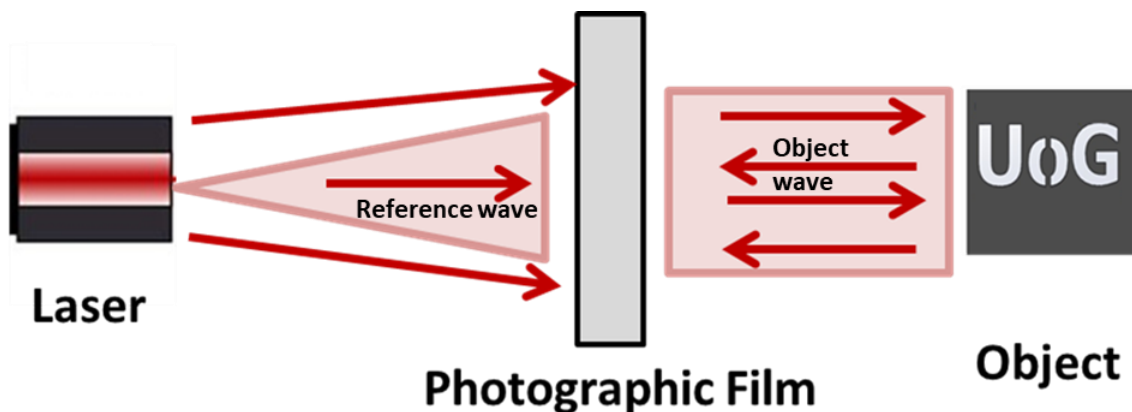
Transmission and Reflection Holography

As mentioned above, when an interference pattern from a coherent source is created by one beam transmitting or reflecting from an object (object beam) and another from the source (reference beam), the wave-front at the interference plane contains the phase information from the object wave-front. The hologram interference pattern can therefore be obtained in either a transmission or

reflection set-up. The simplest ('in-line' or 'on-axis') configurations for these are shown in Figure 3.1.



(a)



(b)

Figure 3.1- Typical in-line (Gabor) arrangements to record a hologram using (a) transmission holography and (b) reflection holography setups where a photographic film is the recording medium

In transmission holography (Figure 3.1(a)), the object beam transmits through the object causing phase changes, whilst the reference beam contains no phase change allowing for an interferogram with the object phase information to be

obtained. In the in-line configuration shown in Figure 3.1(a), some of the radiation passes through the object with no change which constitutes the reference beam whilst some of it is diffracted causing phase changes and the resulting diffracted wave-front is the object beam.

In the reflection setup in Figure 3.1(b) the radiation (in ideal condition) reflects back from the surface of the object, where the section of the object illuminated provides the wave-front corresponding to the object wave containing the phase information. This recombines with the reference wave at the photographic film to create the hologram. Note the roughness of the sample object can affect the reflectivity- when the roughness is similar to that of the radiation wavelength, it can produce speckle where it acts as lots of different reflective surfaces pointing in different directions creating noise in the hologram [68].

In order to reconstruct the holograms from the interference pattern created on the photographic film, a reconstruction laser beam is applied incident to the film. The coherent beam must have the same transverse profile and wavelength as that used when recording the hologram on the film, which means in most cases **using the same laser as that to record the hologram.**

Off-Axis Holography

Whilst the in-line holography set-ups shown in Figure 3.1 are simple ways to obtain a hologram, they suffer from a major drawback- when trying to reconstruct the object, there are three diffraction order modes that are superimposed together- the first order (real object image), second order (a mirror image of this) and the zero order from the mode (TEM_{00} profile of the laser). The

consequences from this problem are described further in chapters 3 and 4 but essentially it means there are three superimposed images that cannot be easily separated.

In order to avoid this, it is possible to use an alternative set-up that uses an off-axis angle ($\theta_{\text{off-axis}}$) between the reference and object beam known as off-axis holography. By increasing the angle between the two beams it becomes possible to separate the three diffraction order terms (from the 3 modes), this can be done until they are no longer superimposed.

Like the in-line holography set-ups, off-axis holography can be used in either transmission or reflection mode. Examples of these are shown in Figure 3.2.

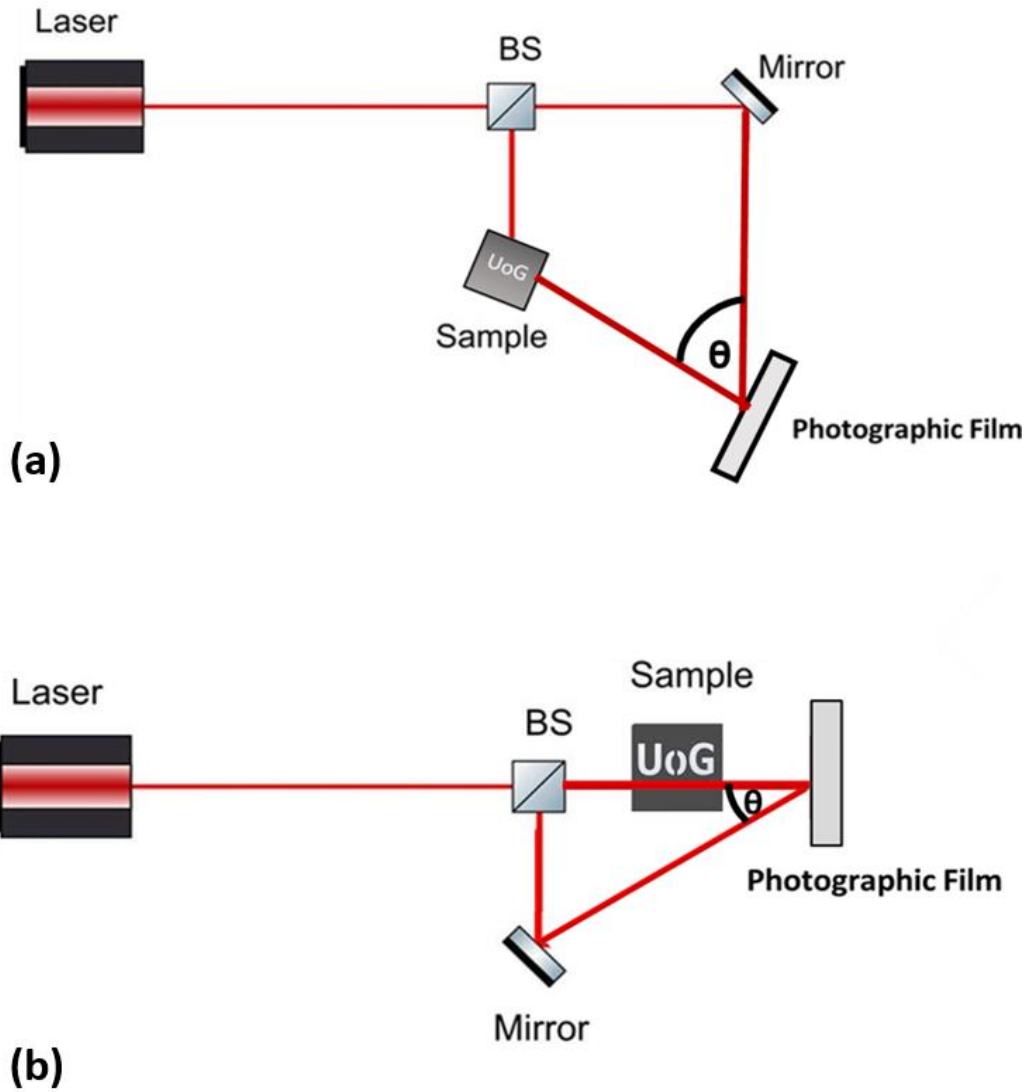


Figure 3.2- Typical arrangements to record a hologram using (a) off-axis reflection and (b) off-axis transmission holography setups where a photographic film is the recording medium

The minimum angle θ_{\min} required to separate the three diffraction order modes can be obtained using Eq. 3.4:

$$\theta_{\min} \geq \sin^{-1}(3B\lambda) \quad \text{(Eq. 3.4)}$$

Where B is the bandwidth of the spatial frequency (maximum spatial frequency of range), and λ is wavelength.

Which can be decreased further when the reference beam is stronger than that of the object beam to that in Eq 3.5 [69]:

$$\theta_{\min} \geq \sin^{-1}(B\lambda) \quad (\text{Eq. 3.5})$$

Since all three diffraction order terms are separated, the two unwanted terms can be eliminated by applying spatial filters in order to obtain just the first order real image.

Another advantage of the off-axis angle is that by increasing the angle between the two beams $\theta_{\text{off-axis}}$, higher spatial resolution may be achieved. The Bragg condition (for interference patterns of light) shown in Eq. 3.6:

$$2d_g \cdot \sin(\theta_{\text{off-axis}}/2) = \lambda \quad (\text{Eq. 3.6})$$

Where λ is the wavelength of laser light, d_g is the spacing between interference fringes. This means by increasing δ , the size of spacing between lines d_g becomes smaller so the system becomes more sensitive and can produce images with greater spatial resolution. Essentially using a larger off-axis angle gives a better spatial resolution.

Digital Holography

Whilst recording a hologram on film as done in analogue holography could have many applications, in order for this to be viable alternative to modern conventional imaging, it is necessary to be able to obtain digital images to allow for modern digital signal processing techniques, data storage and elimination for need of development of photo-sensitive films.

Digital holography can be performed, where instead of obtaining an interference pattern wave-front at the photographic film, the wave-front is obtained via a digital camera. The hologram can then be stored and reconstructed digitally by essentially simulating the reconstruction beam on the digital hologram. This has advantages of not needing a reconstruction beam, instantaneous reconstruction (depending on the processing speed of reconstruction algorithm) and no need for photosensitive film.

When used in this way, digital holography becomes a viable alternative to conventional digital imaging. When considering the unique coherence properties of THz radiation digital holography emerges as a strong option for THz imaging.

To date THz holography has been demonstrated several times - firstly by Heimbeck et al [70-72] (albeit with imaging limitations and never as a video-rate, scanning imaging system).

Both in-line and off-axis holography have been explored with THz radiation for different applications.

The most notable in-line THz holography work was carried out by Rong et al [73], where a set-up using a far-infrared pumped by CO₂ laser and pyroelectric camera were used to image cancer tissue (hepatocellular carcinoma). The set-up used is shown in Figure 3.3.

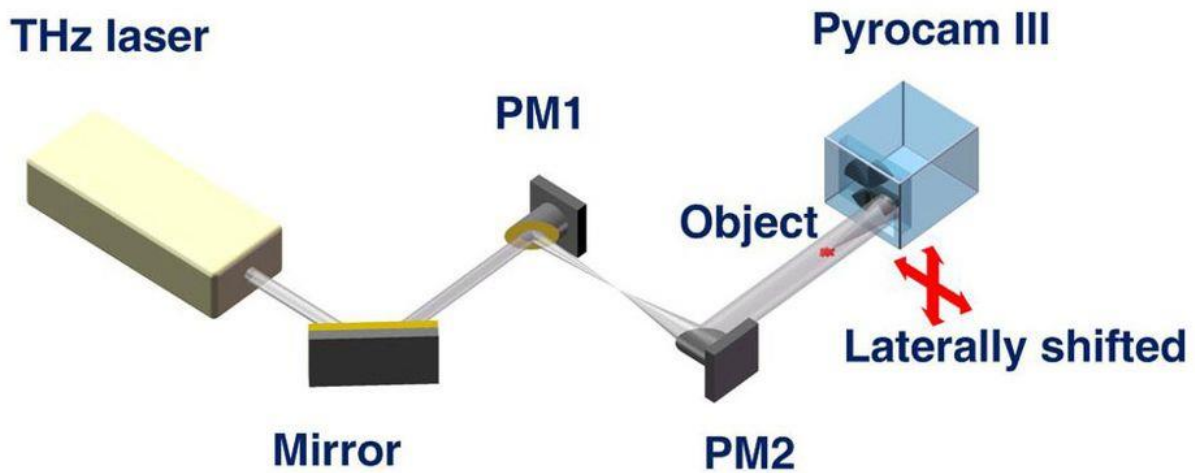


Figure 3.3- In-line THz holography setup for imaging hepatocellular carcinoma using an optically pumped gas laser and pyroelectric camera by Rong et al (image from [73])

This approach demonstrated acquisition time of just a few seconds for a single hologram of a 10mmx10mm sample, which is a significant improvement over THz fibre-scanning imaging techniques approaches which takes ~50minutes for a single frame of similar sample size.

Another drawback of this approach are that for successful reconstruction of the hologram, the area of the object must be about 1% of the area of the beam. If larger objects are to be used, the beam must be expanded meaning a decrease in power, hence a more powerful laser would have to be used or a more sensitive detector, causing more limitations- especially if wanting to image lossy samples (or samples concealed in lossy materials).

Off-axis THz holography was firstly demonstrated by Heimbeck et al [70] at a radiation frequency of 0.7 THz using Schottky diode based frequency multipliers as source and a single pixel Schottky diode detector. Diffraction limited lateral resolutions and an outstanding depth resolution of $\lambda/40$ was successfully achieved. The set-up used is show in Figure 3.4.

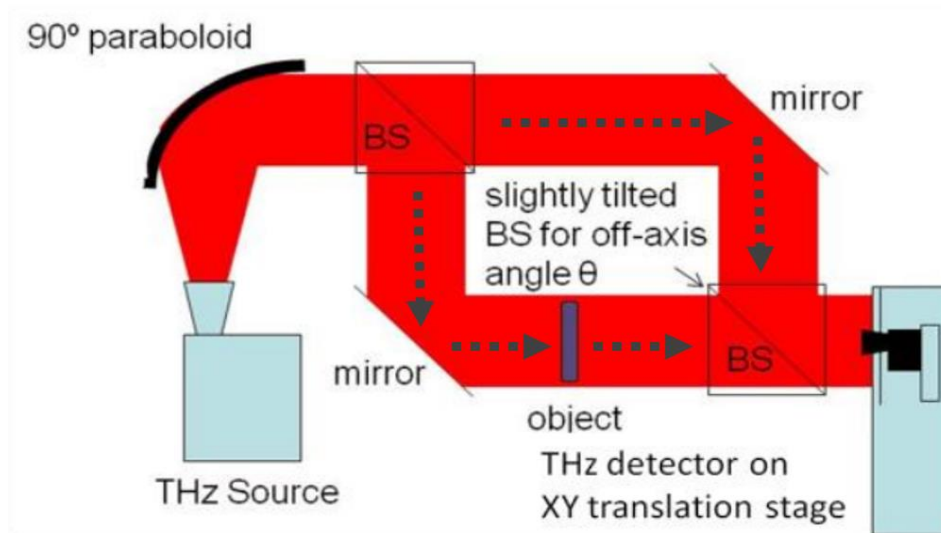


Figure 3.4- Off-axis THz holography set-up with single pixel Schottky diode detector scanned to detect hologram as used by Heimbeck et al (image from [62])

Whilst this approach proved ground-breaking and highly impressive, the practicality was limited due to the single pixel Schottky diode having to be scanned through the hologram plane. This typically took several hours to obtain a single frame depending on the size of sample, number of pixels required in the hologram and integration time for the detector.

The off-axis holography approach was further progressed by Locatelli et al [74] who demonstrated off-axis holography using an FPA. By using the off-axis holography approach with a QCL source and micro-bolometer FPA, entire holograms could be obtained with a single measurement from the detector, as opposed to scanning through the entire hologram plane with a single pixel. By using this approach, holograms were able to be obtained and reconstructed at up to 5 fps, which although not truly ‘real-time’, is a huge improvement on the hours taken for a single hologram to be read with the single pixel Schottky diode. The biggest limitations with this approach were that the low power from the QCL and the lower sensitivity of the LWIR micro-bolometer array as opposed to the

Schottky diode means that the laser must be highly focused to have enough power detected. This limited the system to only being able to image very small objects (maximum of 1-2mm diameter).

4. THz Digital Holography System Design

Digital holography, as described in the previous chapter, could have benefits over conventional THz imaging systems, such as the ability for 3D depth information and potentially minimising optical components.

This chapter will discuss the design choices made for the proposed THz holography imaging system.

4.1 Terahertz Coherence

As mentioned in the previous chapter, coherence is essential in order to produce interference and hence obtain a hologram. However, when working with THz radiation, both temporal and spatial coherence can become very problematic due to the nature of THz waves and their interactions with the optical components.

Stray light can interact undesirably if it re-enters the main beam path causing unwanted interference effects which increase noise and create unwanted phase changes which affect image reconstructions.

Standing waves are waves that have peaks that oscillate with respect to time but not space (amplitude constant along spatial path with respect to time). In optical systems, unwanted standing waves occurring can affect the coherence [75].

Standing wave modes are proportional to wavelength so become much more of a problem with THz than with IR and visible light due to the larger wavelength.

As the wavelength of THz radiation approaches the size of typical optical components, the standing wave effects become much greater than at visible wavelengths. Using larger optical components can be very impractical, expensive and not always feasible.

To understand this effect better, the Fresnel number (n_F) shown in Eq. 4.1 can be used:

$$n_F = \frac{a^2}{\lambda \cdot z} \quad \text{(Eq. 4.1)}$$

Where a is the diameter of the aperture of the pupil, λ is wavelength, z is how far the wave will travel. Note n_F is unit-less [76].

The Fresnel number can suggest which diffraction approximation will best describe the effect (i.e. Fraunhofer or Fresnel). If n_F is <1 , far-field (Fraunhofer) diffraction is the most accurate approximation whereas if $n_F \geq 1$, near-field (Fresnel) diffraction is more prominent [77].

Due to the small size of the optics and large size of wavelength (in comparison to visible and IR), n_F will typically be small which causes unwanted losses and reduced image quality. This illustrates the difficulty when choosing optical components and designing systems when compared to visible and infrared optics.

For this reason, it is important to minimise diffraction losses by using a combination of increasing the size of the optics where possible, maximising all apertures, minimising propagation distances, and minimising the number of optical components used. This is considered when choosing components and set-up design for the THz holography system.

For the system in this thesis, a wavelength of $\lambda=118.8 \mu\text{m}$, aperture diameter (which is given by the beam diameter for the lens-less system) of $a= 20\text{mm}$, and a path length from the laser source to detector of $z\sim 1200\text{mm}$ resulting in a Fresnel number of $n_F\sim 2.81$, meaning Fresnel diffraction is expected.

4.2 Terahertz Holography Laser Source

Choosing the best source to perform holography is essential as coherence is vital to obtaining a good hologram. A laser is usually the chosen source for holography. Choosing a laser becomes more difficult when working in the THz region as there is less available choice as discussed in chapter 1. Essentially there is a choice between QCLs and optically pumped lasers that can be either continuous-wave (CW) or pulsed.

Although pulsed THz imaging has been successfully used in some applications before [78, 79], it suffers from limitations with speed and complexity - needing more components, timing electronics and being more susceptible to phase drift [80]. For a video-rate holographic imaging system, a CW laser would allow for a simpler set-up.

The choice between QCL and an optically pumped laser is a more difficult one - both types of laser suffer from inherent disadvantages. QCLs are very compact in comparison to large pumped lasers and offer extremely good stability. The wavelength emitted can also often be tuned easily. However, QCLs suffer from having low powers ($<4 \text{ mW}$) [32], which, along with small output beam

diameters, limits the system to imaging very small objects (maximum of around 1mm²) due to having to focus the beam, and requires a more sensitive detector.

Optically pumped lasers suffer from instability and are large/bulky compared to QCLs. They also operate with a fixed wavelength which limits ease of tuneability. However, they do produce a much higher power output (>150 mW) which allows for larger areas to be imaged, and an increased power density which allows for penetration of more absorbing materials (such as Teflon) which could be used for imaging hidden objects of interest. It also allows for less sensitive detectors to be used allowing for greater options of camera. The exact power needed depends very much on the detector and application being used. By using higher power sources (>10 mW), there is more flexibility in sources as microbolometer arrays (including those designed for LWIR radiation) may be used, whereas the lower power sources such as QCLs (<4mW) limits the system to either pyroelectric detectors or microbolometer detectors with a highly focussed beam. A summary of the advantages of each type of laser is shown in Table 4.1.

Type of Laser	Advantages	Disadvantages
QCL	Stability, compactness, easily tuneable wavelength	Low power (<4 mW)
Optically Pumped	High power (> 150mW)	Unstable, large, wavelength fixed (to that emitted by gas line)

Table 4.1- comparison of QCL and optically pumped laser advantaged and disadvantages. Optically pumped provide higher power at the cost of stability whilst QCLs offer better stability at the cost of power.

Although QCLs have numerous advantages over the optically pumped laser, the lack of power and hence small beam size limit the applications for a holography system. For this reason, it was decided that an optically pumped laser will be used in order to image larger areas, penetrate through obscuring materials and allow a less sensitive detector to be implemented into the system allowing for potentially better resolution and lower cost.

The laser that was chosen was an Edinburgh Instruments FIR-295. This consists of CH₃OH (methanol) particles pumped by a high powered LWIR CO₂ laser that results in a wavelength of 118.8μm being produced with a power of ~150mW [81].

It was important to check the characteristics of the laser before committing to building the system as the laser source is the most important part of a holography system.

The spatially distributed patterns of laser light are described by transverse modes – eigenmodes of the laser cavity patterns. The solutions to these eigenmodes are notated as TEM_{nm} which stands for transverse electric and magnetic mode, where n and m are the number of intensity nodes. The TEM₀₀ mode is the lowest-order mode and is extremely desirable for lasers to operate in this mode. TEM₀₀ mode is where the most efficient, most stable performance, beam divergence, waist size and power are all achieved [82].

The ideal laser profile is one that operates with TEM₀₀ and has a fully Gaussian, round profile. The beam should be collimated (not diverging, or in practice very

little divergence) with a small waist size. The ideal beam is illustrated below in Figure 4.1.

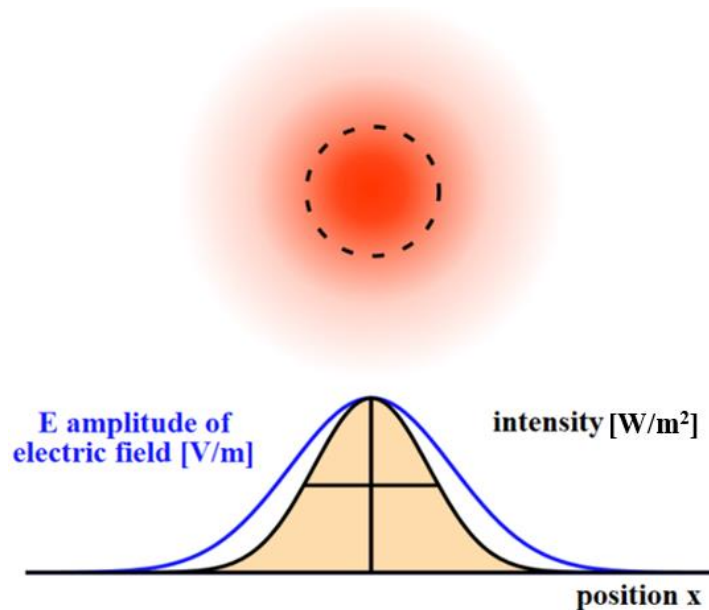


Figure 4.1 – Ideal laser beam profile which shows a normalised Gaussian distribution of intensity with the full width half maximum (FWHM) highlighted (image from [83])

This was used as the standard to compare the beam profile of the optically pumped THz laser being used. To analyse the laser, the best obtainable image of the beam was taken after focusing it using a 10mm focal length lens onto an LWIR Microbolometer FPA (FLIR Photon 320).

Another important factor for laser beam quality is the temporal stability- in other words, how well it can retain its profile over time. A laser that is stable over time and retains the same profile without drift, changing of shape or flickering is much more preferable for repeatability, measurements that require longer measurements in terms of time (for example on biological samples over a long period or measurements that require lots of frames of data), for stitching

together lots of images to form a larger image or scanning a large array without unwanted artefacts from the laser.

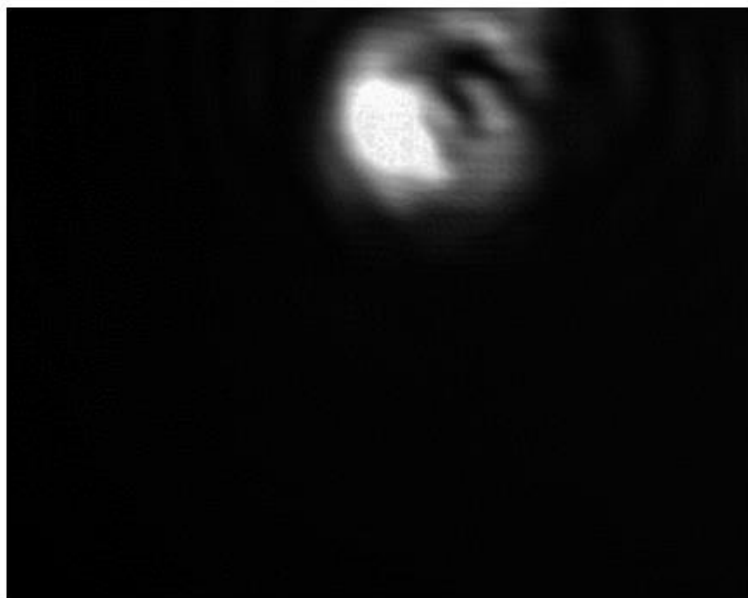
The temporal stability of the laser chosen for this system was poor and subsequently lead to many problems-the beam profile was constantly changing due to the temporal instability of the laser. This was mainly caused from mechanical instabilities and contamination within the laser cavity.

Changing the cavity length changes the stability and profile of the beam. Even when the laser is at its most stable and with the best roundness as shown in Figure 4.2(a), the beam profile still constantly changes slightly. At best the laser beam could go ~2 seconds without major flickering or the shape of the beam changing slightly. The holograms obtained in this thesis generally suffer from flickering when used in scanning/video mode and when stitching larger images together, it can be seen that there are artefacts caused in each frame from where the beam profile changes slightly.

For comparison, Figure 4.2(b) shows the suboptimal beam profile with a different (incorrect) cavity length.



(a)



(b)

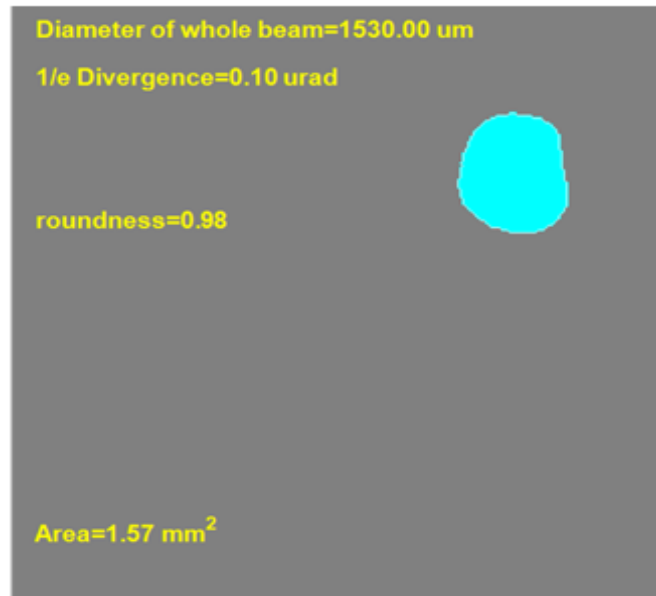
Figure 4.2- Laser beam profile images recorded on LWIR microbolometer FPA showing (a) Best obtainable profile with TEM_{00} mode showing fairly round profile and (b) a sub-optimal beam profile that has poor roundness and non-Gaussian distribution

Using Matlab image recognition functions, the roundness of the beam was calculated as 0.98 (shown in Figure 4.3) which shows that the beam is not fully Gaussian but the profile is acceptable. The vertical and horizontal cross-section of the beam are also shown to help illustrate the shape.

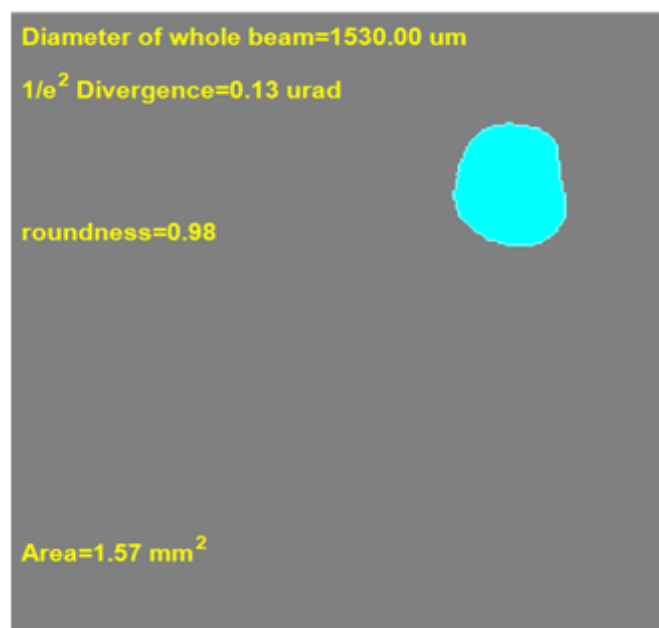
The divergence θ_d of the beam could also be calculated from this which helps understand how collimated the beam is. The divergence can be calculated using Eq. 4.2 below [84]:

$$\theta_d = \frac{d_b}{f} \quad \text{(Eq. 4.2)}$$

Where d_b is the diameter of the beam and f is the focal length of the lens (10mm). Rather than measure the divergence of the whole beam, the $1/e$ or $1/e^2$ divergence are usually used as this gives a more accurate representation of the Gaussian beam quality [85]. The $1/e$ and $1/e^2$ divergences are also shown in Figure 4.3. The code used for these is shown in Appendix 1.



(a)



(b)

Figure 4.3- Beam Profiles from Figure 4.2 analysed with Matlab to find the roundness (0.98), and show (a) 1/e divergence=0.1 μrad and (b) 1/e² divergence=0.13 μrad

The point of the beam where the radius is at the smallest is called the beam waist. This could be obtained by finding the minimum radius in Matlab and was found to be 1260 μm . Using this and Eq. 4.3, the minimum possible divergence can be found [85]:

$$\theta_{\min} = \frac{\lambda}{\pi w} \quad (\text{Eq. 4.3})$$

Where w is the beam waist and λ is the wavelength. At $\lambda=118.8 \mu\text{m}$ this gives a minimum divergence of 0.03 μrad . Comparing this to the $1/e$ and $1/e^2$ (0.1 and 0.13 μrad respectively) beam diameter, it can be seen that the values are close (0.1 μrad apart) and so the beam is close to being diffraction limited. From this it can be seen that the laser profile is more than acceptable for the purpose of digital holography.

4.3 Terahertz Holography Detector Resolution and Choice

Apart from the source, the detector is the next most important component of the system. Many of the imaging abilities and system constraints are dependent on the detector parameters so choosing the correct detector is important.

Constraints such as sensitivity, number of pixels, pixel pitch, aperture size, cost, frame-rate and ease of integration must all be considered. However, the main choice will be based around achieving the best resolution with the other constraints having less weight.

It is important to describe the relationship between camera parameters and resolution.

The resolution of the holography system is essentially a convolution of the resolution function of the pixel pitch of the camera and the numerical aperture (NA) of the system. The Fresnel approximation of the resolution function of the camera is shown in Eq. 4.4 [86].

$$R_x = N e^{-j(N-1)x p_x / \lambda z_0} \text{sinc} \left(\pi \frac{N p_x}{\lambda z_0} x \right) \quad (\text{Eq. 4.4})$$

Where lateral R_x is the resolution in x-axis, N is the number of pixels in x-direction, p_x is the pixel pitch in the x direction, z_0 is reconstruction distance (distance between sample and detector) and λ is wavelength.

The first zero of Eq. 3.3 can be found with Eq. 3.5:

$$d_x = \lambda \frac{z_0}{N_x \cdot p_x} \quad (\text{Eq. 4.5})$$

Where d_x is the lateral resolution (the smallest size that can be distinguished).

This gives a very important definition of the best detector: **in order for the best resolution, the smallest distance between detector and object must be chosen, along with the highest number of pixels possible and the smallest possible pixel pitch.** In other words, choosing a camera with a large number of pixels, with small pixels and minimum obscuration to allow close proximity of sample target.

When discussing performance metrics of thermal detectors, the responsivity/sensitivity of the detector along with the noise influence must be

considered to assess performance- especially when comparing different types of detectors that operate using different methods. Hence parameters such as signal to noise ratio (SNR) are more useful than just the responsivity of the detector. A useful parameter is the noise equivalent power (NEP) which is described as the power detected to give an SNR of 1. NEP can be found using Eq. 4.6 where V_{noise} is the noise signal voltage and V_R is the responsivity voltage (the ratio of voltage detected by detector element to the power of light at detector element).

$$\mathbf{NEP} = \frac{V_s}{V_R} \quad \mathbf{(Eq. 4.6)}$$

NEP is measured in the unit W/\sqrt{Hz} . This figure of merit can be made more useful if the bandwidth and detector area are also considered. The D^* measurement is often used as this and is defined as shown in Eq. 4.7 using the unit $m\sqrt{Hz}/W$ [87]:

$$\mathbf{D^*} = \frac{\sqrt{A_p B}}{NEP} \quad \mathbf{(Eq. 4.7)}$$

The lowest NEP detectors in THz range are pyroelectric detectors and microbolometer detectors specifically made for THz wavelengths. However, when using the D^* merit, the detection capabilities of LWIR microbolometer FPAs designed for 7-13 μm wavelengths show similar performance. A comparison of the D^* and resulting SNR with a 10mW laser source incident, for a state of the art THz microbolometer (NEC IRV-T0831) FPA, a pyroelectric camera (Spiricon Pyrocam III HR), and 2 different LWIR microbolometer FPAs at $\lambda=118.8 \mu\text{m}$, it was seen that the LWIR microbolometer FPAs (a VOx based Devitech IR032 and an a-Si based Xenics Gobi 640) demonstrated equally good or better performance

than those specifically made for THz radiation [88]. This could also be seen when comparing the best possible (limiting) resolution of reconstructed holograms at this wavelength. The comparison can be seen in Table 4.2.

Detector Type:	LWIR Microbolometer FPA: Devitech	LWIR Microbolometer FPA: Xenics	THZ Microbolometer FPA: NEC	Pyro-electric Camera: Spiricon
D* ($cm\sqrt{Hz}/W$)	3.5x10 ⁷	4.48x10 ⁷	2.35x10 ⁷	5.86x10 ⁷
SNR with laser power of 10mW at $\lambda=118.8 \mu m$	60	80	60	3
Limiting resolution at $\lambda=118.8 \mu m$ (mm)	0.06	0.06	0.065	0.07

Table 4.2- Comparison of Detector Performance of two different LWIR microbolometer FPAs, a THz microbolometer FP and Pyroelectric camera with a 10mW laser emitting radiation of 2.52 THz. The LWIR microbolometer arrays offer at least as good SNR and resolution as the other detectors that were specifically designed for detecting THz frequencies. (data from [88])

From these results it can be concluded that the SNR and limiting resolution of all 3 microbolometer detectors at 118.8 μm were very similar whilst the pyroelectric camera has a worse SNR. This leads to design decision that **since the resolution is very dependent on pixel pitch and number of pixels. Since the SNR performance of LWIR and THz microbolometers are similar with power ≥ 10 mw, it would be a better choice to use an LWIR microbolometer FPA since larger arrays of smaller pixels are available.** These detectors are also much less expensive than pyroelectric or THz FPAs and more readily available. Many of these are also capable of operating at higher frame-rates than the THz cameras (state of the art i2s operates at 25 Hz max). Therefore, a LWIR microbolometer FPA was chosen as they could offer better resolution due to smaller pixel pitches, larger pixel arrays, at least as good SNR, faster frame-rates and lower cost.

The chosen detector was a Xenics Gobi 640-CL LWIR microbolometer FPA as this had the smallest pixel pitch (17 μm), highest number of pixels (640x480), best SNR at 118.8 μm (80), and fastest native frame-rate (50 Hz) at the time of purchase. Note that original preliminary tests were carried out on a lower spec LWIR camera (FLIR Photon 320 with 38 μm pixel pitch and 320x256 pixels) before being switched to the Xenics Gobi 640-CL.

4.4 Terahertz Optical Components

The significance of diffraction effects with optics in the THz range was discussed in Section 4.1. As well as suffering from the problem with standing waves and unwanted diffraction when using standard visible or IR size lenses at THz wavelengths, material uniformity and inhomogeneities also affect the performance. THz lenses often cause aberrations when used to expand/collimate and typically cause severe standing waves.

It therefore made sense to try to limit the number of optics and avoid using lenses where possible. For this reason, it was decided to use commercially available mirrors for collimation which have minimal surface roughness, good reflectivity at THz wavelengths (>90%) and should remove any aberrations or standing wave effects.

A high resistivity float zone silicon (HRFZ-Si) beam-splitter specifically designed for THz by Tydex [89] was also purchased. This has a 54/46% transmission/reflection characteristic at 2.52 THz (with negligible absorption) and is designed to minimise standing wave and aberration effects. This is shown in Figure 4.4.

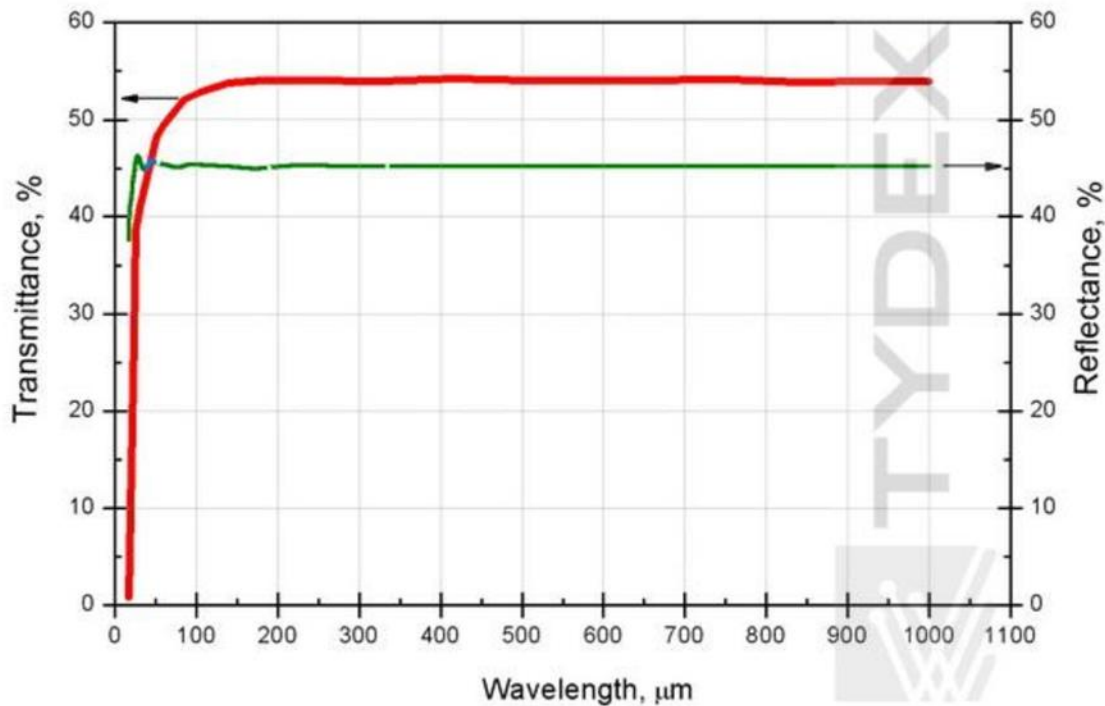


Figure 4.4- Tydex HRFZ-Si beam-splitter reflection (green)/transmission (red) vs wavelength plot. There is 54/46% transmission/reflection at $\lambda=118.8 \mu\text{m}$ (image from [89])

It was decided that to minimise unwanted effects from the optics, just two mirrors - one for collimation and one for the beam would be used along with the beam-splitter as the only optics in the system. Standard silver collimating and planar mirrors from Thorlabs were used.

4.5 Terahertz Holography System Set-Up

As discussed in the previous chapter, there are numerous different types of set-up for a digital holography system. One of the advantages of working with THz (compared to visible or IR radiation) for holography is that the larger wavelength

naturally lends itself to being very effective in off-axis holography since a larger off-axis angle ($\theta_{\text{off-axis}}$), can be used which is a distinct advantage.

As previously mentioned, the maximum achievable resolution of a holographic system is dependent on several parameters - the pixel pitch of the detector, the number of pixels and the distance between the sample object and detector. Since a larger $\theta_{\text{off-axis}}$ allows for a closer distance between the sample object and detector whilst still insuring that the reference and object beams of the holography system only meet at the hologram plane - it can be seen that a larger $\theta_{\text{off-axis}}$ will lead to a smaller distance and better resolution. This also means a larger $\theta_{\text{off-axis}}$ will result in a higher NA.

The maximum off-axis angle the holography system can use depends on the detector. For any detector, the optical transfer function (OTF) may be used to describe its performance over a range of spatial frequencies. This can be found for this holography set-up using Eq. 4.8 [90]:

$$OTF \propto \left| F \left[\text{rect} \frac{x}{w} \right] \right|^2 \propto \text{sinc}^2(p \cdot f_x) \quad \text{(Eq. 4.8)}$$

In the x-direction where w is the aperture size, f_x is the spatial frequency (number of lines or fringes per unit distance) at position x , and p is the pixel pitch. (For the Xenics Gobi 640 this is 640 pixels in x-axis with 17 μm pixel pitch, p).

Therefore, if the maximum spatial frequency f_{cutoff} of the camera can be found, then it becomes possible to find the maximum off-axis angle using Eq. 4.9:

$$\theta_{\max} = \sin^{-1} \left(f_{\text{cutoff}} \cdot \lambda \right) \quad \text{(Eq. 4.9)}$$

This angle allows for minimum distance between sample and detector to be found, hence the best resolution to be achieved.

Another consideration is whether the off-axis setup should be in reflection or transmission mode. Although both set-ups have advantages depending on the application, it was decided that for this system a reflection setup should be used for the following reasons:

Firstly, using reflection mode allows for a shorter distance d , between the detector and sample without the two beams interfering before the hologram plane at the detector.

Secondly, if an extra mirror was used in transmission mode, the extra component would be expected to affect the system performance. By using less optical components the system will have less loss, aberrations and reflections so keeping the number of optical components to a minimum will result in better performance.

Lastly, it may be possible to use this system as a potential scanning inspection/NDE tool - particularly for concealed metallic objects - which naturally lends itself better to reflection mode imaging since metallic objects are highly reflective in the THz region whilst many packaging materials are very transmissive in THz.

By using the system in reflection mode and finding the cut-off frequency f_{cutoff} , for the Xenics Gobi 640-Cl camera with the laser used (found from largest angle that

fringes could be obtained) as having a fringe spacing of $f_{\text{cutoff}}=6.92$ cycles/mm, the maximum off-axis angle was found as $\theta_{\text{max}} = 55.3^\circ$. This resulted in a minimum working distance of $d=15\text{mm}$, which was used for the system.

The proposed THz holography setup is therefore shown below in Figure 4.5:

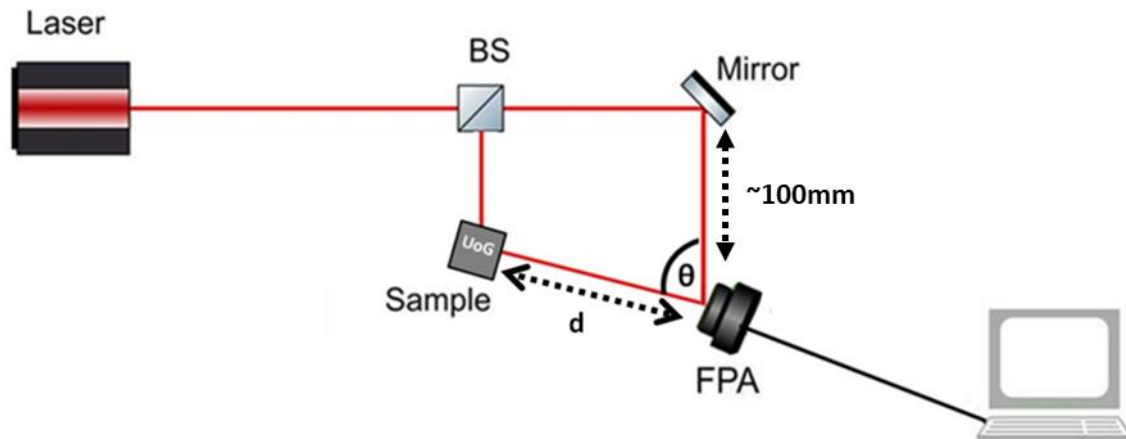


Figure 4.5 - THz Holography Off-Axis Reflection Set-Up Chosen for the system where an optically pumped laser with $\lambda=118.8 \mu\text{m}$, an HRFZ-Si beam-splitter, planar silver mirror, and Xenics Gobi 640-CL FPA. Off-axis angle of $\theta=55.3^\circ$ and distance of $d=15\text{mm}$ between detector and sample were also chosen.

5. Terahertz Digital Holography System

Performance

As discussed in Chapter 4, an off-axis reflection mode set-up was selected as the optimal THz holography configuration. The system will feature a large methanol pumped FIR laser (Edinburgh Instruments FIR-295) at $\lambda = 118.8 \mu\text{m}$ (frequency of 2.52THz), a LWIR microbolometer FPA (Xenics Gobi 640) and some reflective optics (collimating mirror, beam-splitter and plane mirror). This should result in optimal performance of the system by ensuring highest possible laser power and imaging area, optimal resolution (highest pixel pitch and number of pixels on the detector along with minimum distance between sample and detector) and minimal losses (minimising lossy components). Table 5.1 summarises this.

System Parameter	Value
Laser Output Wavelength	118.8 μm
Laser Power	~150 mW
Detector Pixel Pitch	640x480
NA	0.23
Imaging Area	7x7 mm
Stand-off Distance	15 mm
Lateral Resolution	~250 μm

Table 5.1- Summary of chosen THz holography system imaging parameters and performance

In this set-up a Thorlabs motorised stages (Thorlabs MTS25-Z8) were used to control x, y and z directions of the sample. For accurate alignment and scanning of the sample, the stages can be controlled using the Thorlabs motor (KDC01) software ('Thorlabs APT' software) allowing step sizes as small as 1 μm .

The interferograms are recorded at the detector plane by the FPA. Digital reconstructions of these interferograms can then be carried on the computer using specially designed software.

A schematic of the system set-up is shown below in Figure 4.5 whilst an example 3D image of how this would look on an optical bench is shown in Figure 5.1.

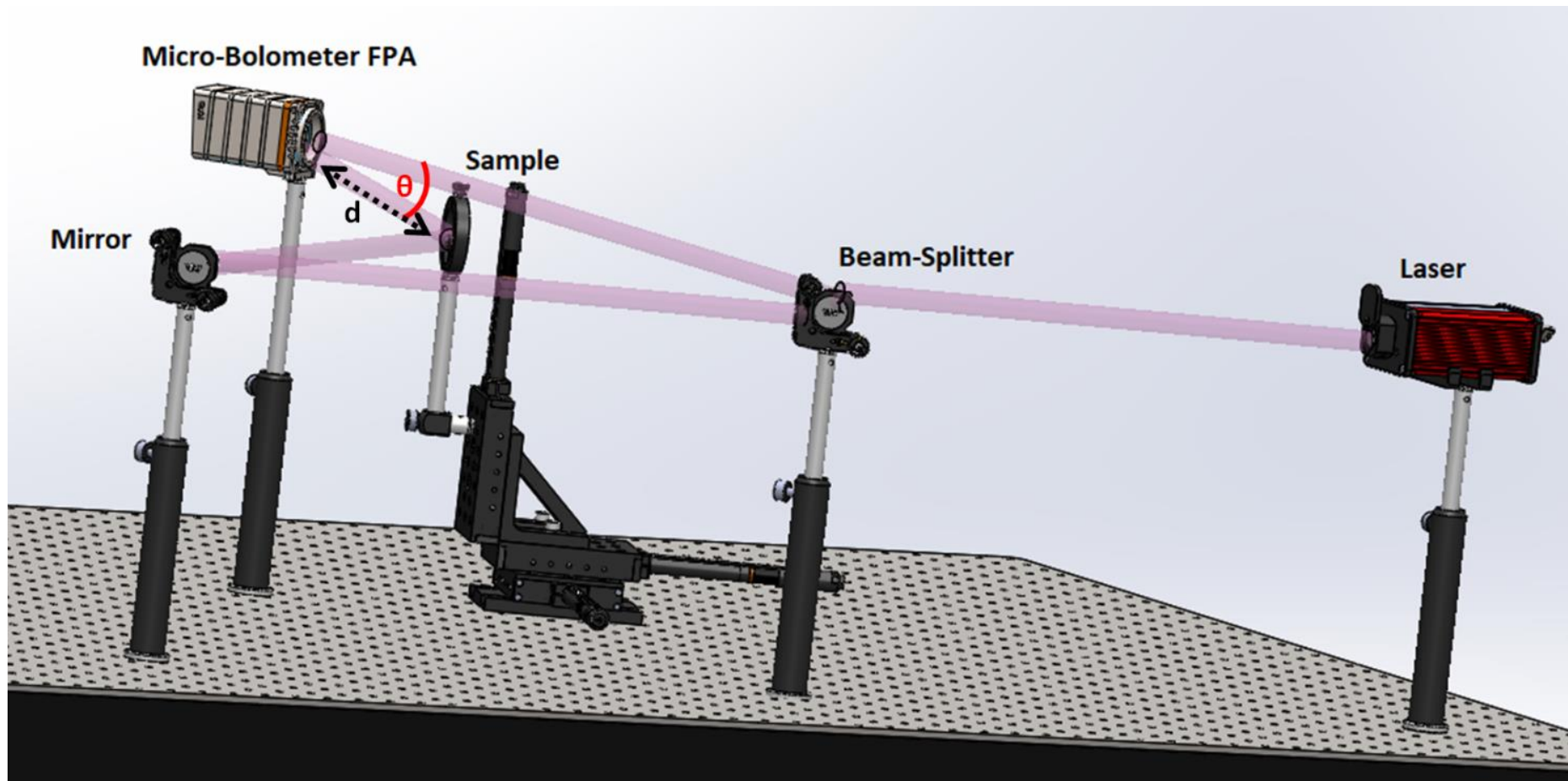


Figure 5.1- Off-Axis Reflection Mode Set-up for Digital THz holography as could be set-up on an optical bench with sample mounted on an x,y,z stage at a distance of $d=15\text{mm}$ from detector. An off-axis angle of $\theta=55.3^\circ$ between reference and object

beam was used

5.1 Recording an Interferogram

As discussed in Chapter 3, in order to obtain a successful hologram, the most important step is to obtain a high quality interferogram containing information of the sample object whilst minimising noise. In the case of this reflection set-up, the sample object used was an aluminium object drawn in CAD with a smallest feature size of 0.8 mm. The sample object features the letters 'UoG' each being around 2.8 mm wide with the total width of the three letters being around 9 mm. The object is shown below in Figure 5.2.

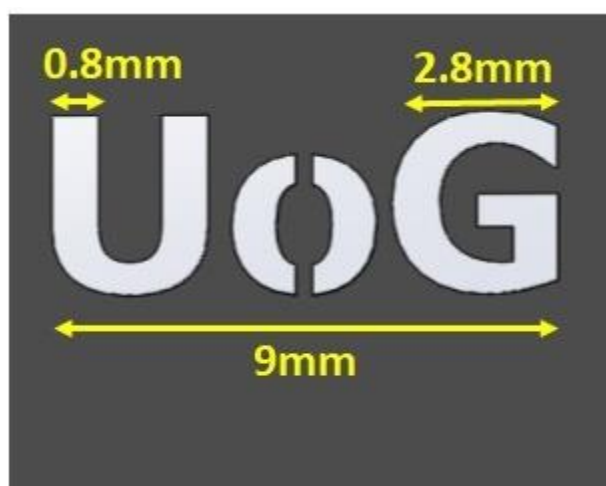


Figure 5.2- CAD drawing of the aluminium sample object used in the THz holography experiments

The sample was placed on electronically controlled translation stages for precise alignment and to allow scanning of objects to be performed.

Initial interferograms were recorded using a different camera- a FLIR photon 320. Although it was possible to record an interferogram using this FPA, it was very suboptimal for the following reasons:

- The camera had a large amount of housing/covering in front of the sensor- this metal housing caused unwanted reflections and needed to be removed.
- The larger pixel pitch of 38 μm results in a lower spatial frequency being obtainable and hence smaller off-axis angle, hence larger distance between sample and detector.
- The camera suffered from a large number of damaged pixels
- The smaller number of pixels (320x256) compared to the Xenics Gobi 640 (640x480) also impacts maximum resolution.

For these reasons the Xenics Gobi camera was used, which features both smaller pixels (17 μm) and a greater number of them. In order to optimise the performance of the camera and obtain the best possible interferogram the following steps were taken:

- All camera housing/covering was removed from the front of the detector and the FPA was arranged so that it was flush with the edge of the camera holder. This minimised any reflections or losses at the FPA plane.
- Gain and offset adjustments were made using the Xenics Xeneth software algorithm to obtain best possible contrast and hence best interferogram.

Note that the camera applies a non-uniformity correction (NUC)

calibration to the array by factory default to minimise error in cross-pixel gain.

- Since the camera is of a microbolometer variety which naturally suffers from thermal background noise- the laser was blocked and a two-point calibration was performed immediately before recording interferograms to account for the noise from the ambient temperature of the room. (The thermal noise from the room and having a person in it generating blackbody radiation can be picked up from the camera).

In order to find the cut-off frequency f_{cutoff} of the camera, interferograms were recorded with gradually increasing off-axis angle $\theta_{\text{off-axis}}$ until the smallest possible fringe spacing was found. This resulted in f_{cutoff} of 6.92 cycles/mm.

Using this along with Eq. 4.9:

$$\theta_{\text{max}} = \sin^{-1} \left(f_{\text{cutoff}} \cdot \lambda \right) \quad \text{(Eq. 4.9)}$$

Results in maximum off-axis angle of $\theta_{\text{max}} = 55.3^\circ$ which is used to obtain best resolution.

Using this angle resulted in using a minimum working distance of 15 mm between the sample object (~9x9 mm) and detector. This is the minimum distance at this angle where the sample object could be placed that didn't cause the two beams to interfere before they reach the FPA. However, it should be noted that in terms of reconstruction, **there is no minimum distance requirement for the of angular spectrum reconstruction approach, in contrast to the traditional Fourier method.**

At this position the detector was found to have a 7x7 mm imaging area. The numerical aperture (NA) of the system was then obtained as NA=0.23, using Eq. 5.1:

$$NA = n \sin(\theta) \quad (\text{Eq. 5.1})$$

Where $\theta = 13.5^\circ$ (from imaging array and distance to sample).

Note that the distance between sample object and detector was chosen to optimise resolution, but that a larger distance can be used depending on the application.

It should also be noted that the sample was angled slightly toward the detector in order to reduce reflections from re-entering the detector which causes unwanted Fabry-Perot fringes and hence poorer quality interferograms.

Using this setup, an interferogram such as the one shown below in Figure 5.3 could be obtained. Note the image is stitched from two interferograms in order to fit the entire object into the field of view (since the system has a 7 mm imaging area but the sample is >9 mm wide). The lines in the interferogram are the interference fringes- as mentioned above, **more and narrower fringes results in a better hologram.**

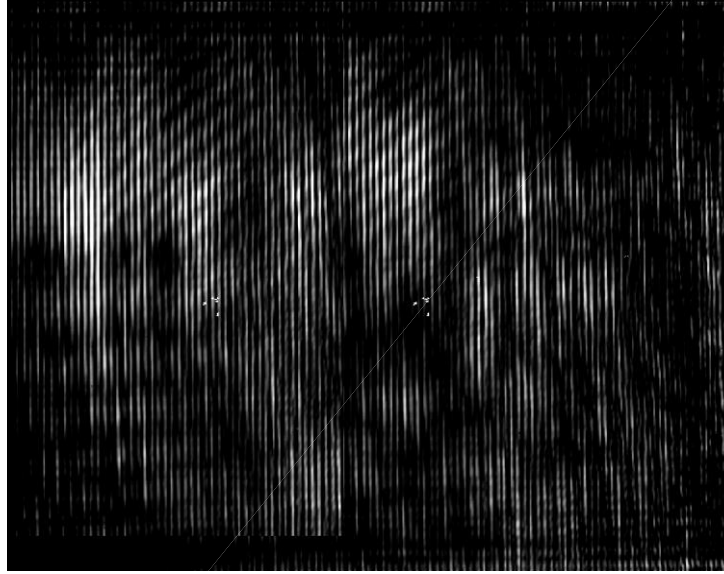


Figure 5.3- Interferogram of ‘UoG’ sample object in reflection mode stitched from 2 interferograms to increase FoV. The fringes are caused by the interference between the object and reference beams.

5.2 Reconstructing Holograms

As described in chapter 2, digital hologram reconstruction in its simplest form involves taking the recorded interferogram and essentially simulating the reconstruction beam. As one would expect, there are several different algorithms that could be used- the simplest of which would be Fourier reconstruction.

This involves describing the interferogram from the Fresnel diffraction pattern (far-field) at the detector plane from the sample wave $\Psi_0(x,y)$ in Eq. 5.2(a), and reference wave $\Psi_r(x,y)$ in Eq. 5.2(b) [91]:

$$\Psi_0(x,y)=\exp\left[\frac{-j}{2\lambda z_0}(x^2 + y^2)\right] \times F\left\{\sigma_0(x,y)\exp\left[\frac{-j}{2\lambda z_0}(x^2 + y^2)\right]\right\}$$

(Eq. 5.2(a))

$$\Psi_r(x,y)=\exp\left[\frac{-j}{2\lambda z_0}(x^2 + y^2)\right] \times F\left\{\delta(x - x_0, y)\exp\left[\frac{-j}{2\lambda z_0}(x^2 + y^2)\right]\right\}$$

(Eq. 5.2(b))

Where $\sigma_0(x, y)$ is the position of the sample object, $\delta(x - x_0, y)$ is the distance between sample and detector, whilst F denotes Fourier Transform.

The resulting hologram of these two waves interfering would be given by Eq. 5.3:

$$H(x,y)=|\Psi_0(x,y)+\Psi_r(x,y)|^2 \quad \textbf{(Eq. 5.3)}$$

Expanding this and looking at the cross terms gives Eq. 5.4:

$$\begin{aligned} \Psi_0(x,y)\Psi_r^*(x,y)+\Psi_0^*(x,y)\Psi_r(x,y) &= \exp\left[\frac{-jx_0x}{2\lambda z_0} + \frac{jx_0^2}{2\lambda z_0}\right] \times \\ &F\left\{\sigma_0(x,y)\exp\left[\frac{-j}{2\lambda z_0}(x^2 + y^2)\right]\right\} + \exp\left[\frac{jx_0x}{2\lambda z_0} - \frac{jx_0^2}{2\lambda z_0}\right] \times \\ &F\left\{\sigma_0(x,y)\exp\left[\frac{-j}{2\lambda z_0}(x^2 + y^2)\right]\right\} \end{aligned} \quad \textbf{(Eq. 5.4)}$$

In order to reconstruct the hologram, a simple Fourier transform of Eq. 5.4 is applied which gives Eq. 5.5 (ignoring the component from the zero order mode of the laser):

$$\begin{aligned} F\{\Psi_0(x,y)\Psi_r^*(x,y)+\Psi_0^*(x,y)\Psi_r(x,y)\} &\propto \sigma_0\left(-\frac{z_0}{f}x + x_0, -\frac{z_0}{f}y\right) \times \\ \exp\frac{-j}{2\lambda z_0}\left[\left(\frac{z_0}{f}x - x_0\right)^2 + \left(\frac{z_0}{f}y\right)^2\right] &+ \sigma_0^*\left(\frac{z_0}{f}x + x_0, \frac{z_0}{f}y\right) \times \exp\frac{j}{2\lambda z_0}\left[\left(\frac{z_0}{f}x + \right. \right. \\ &\left. \left. \dots x_0\right)^2 + \left(\frac{z_0}{f}y\right)^2\right] \end{aligned} \quad \textbf{(Eq. 5.5)}$$

Where the first term returns an image of the sample object and the second returns a mirror image of the sample. An example of how the three terms appear is shown below using a simulated hologram in Figure 5.4. Note that the simulation uses a CAD image of the sample object in Figure 5.2 and the hologram was simulated by simulating the propagation using Eq. 5.4 (code in Appendix 2). The first order image is highlighted in green whilst the other two terms are the mirror image (red highlight) and zero order mode image (yellow circle in the centre).

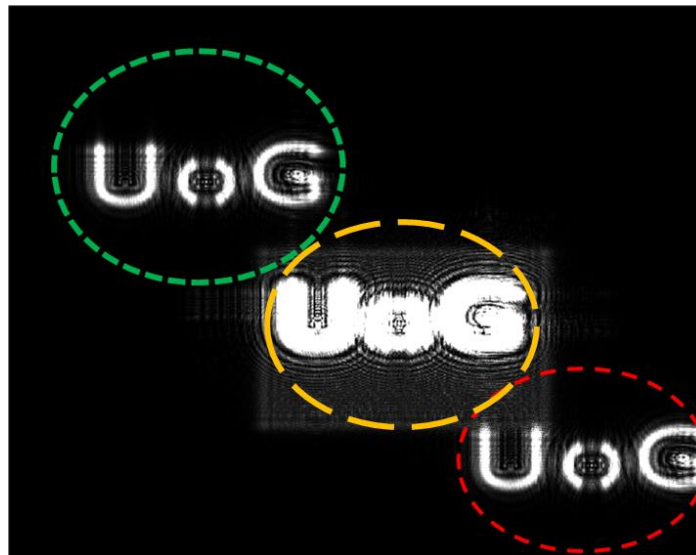


Figure 5.4 –Fourier reconstruction of simulated hologram of ‘UoG’ sample showing the first order term (green circle top left), zero order mode (yellow circle centre) and second order mirror image (red circle bottom left).

Sampling considerations must also be taken into account as with any digital signal processing. The Nyquist frequency describes the minimum sampling frequency needed to prevent aliasing (signals overlapping, becoming indistinguishable causing noise, spatial warping etc.) [92]. The Nyquist frequency N_f is defined in Eq. 5.6:

$$N_f = f_s / 2 \quad (\text{Eq. 5.6})$$

Where f_s refers to sampling frequency. Hence in order to prevent aliasing and obtain an accurate hologram reconstruction, **it is vital that the bandwidth of the hologram is limited to the Nyquist frequency** (so any spatial frequencies greater than the Nyquist frequency are set to 0). The sampling frequency may be increased by using more sample points- by adding extra zero's to the array (zero padding), which results in more frequency bins with closer spatial separation, resulting in an artificial increase in f_s . This ensures aliasing never occurs.

5.3 Angular Spectrum Reconstruction

Although simple Fourier reconstructions are beneficial, they suffer from the major drawback of requiring a minimum z_{\min} distance between the detector and sample as shown in Eq. 5.7:

$$z > (p_x(W_x)) / \lambda \quad (\text{Eq. 5.7})$$

Where p_x is pixel pitch in the x direction and W_x is the detector width in the x direction.

As discussed in Chapter 4, having the smallest possible distance between detector and object results in the best obtainable resolution hence having a minimum distance constrains this along with allowing less options for sample position choices.

An alternative reconstruction method that does not require a minimum distance between sample and object hence allowing potentially better resolution and greater system flexibility is the angular spectrum reconstruction method [93]. It should be noted that the angular spectrum reconstruction algorithm uses two Fast Fourier Transforms (FFTs) which are quite computationally demanding. For this reason, it requires either more computational power or performs at slower speed than the standard Fourier method.

The angular spectrum describes the 2D Fourier Transform of a wave-field in the x - y plane propagating in the z plane. This can be denoted as wave-field $W(x,y,z)$ with corresponding angular spectrum $A(\alpha/\lambda, \beta/\lambda, z)$ where α and β are the x and y directional cosines corresponding to the spatial frequencies of $W(x,y,z)$.

The angular spectrum at the detector can be found by choosing the distance z between the sample object and hologram plane (this can be found using a simple iterative ‘if’ loop qualitatively or autofocus algorithm quantitatively). This is then applied to FFT of the angular spectrum $A(\alpha/\lambda, \beta/\lambda, z)$ which is multiplied by the propagation kernel in Eq. 5.8 which take into account the propagation between distance z to obtain angular spatial frequencies at point z :

$$A\left(\frac{\alpha}{\lambda}, \frac{\beta}{\lambda}, z\right) = A\left(\frac{\alpha}{\lambda}, \frac{\beta}{\lambda}, 0\right) \exp\left(j \frac{2\pi}{\lambda} \sqrt{1 - \alpha^2 - \beta^2} z\right) \quad \text{(Eq. 5.8)}$$

Applying the FFT to Eq. 5.8 gives the wave-field of the original object $H(x,y,z)$. Digital simulation of the reference wave can then be applied followed by filtering

to remove the second and zero order terms so that only the first order term containing the sample object remains. The reference wave, R , with off-axis angle θ , is simulated using Eq. 5.9:

$$R(\theta) = \exp\left(j \frac{2\pi}{\lambda} y \cdot \sin(\theta)\right) \quad \text{(Eq. 5.9)}$$

The FFT of $H(x,y,z) \cdot R(\theta)$ then gives the Fourier space plot as shown in Figure 5.5 for a simulated hologram containing the 1st order image (highlighted with green circle to top left), mirror image (highlighted in red circle to bottom right), and zero-order mode (highlighted in yellow circle in center) wave-fields.

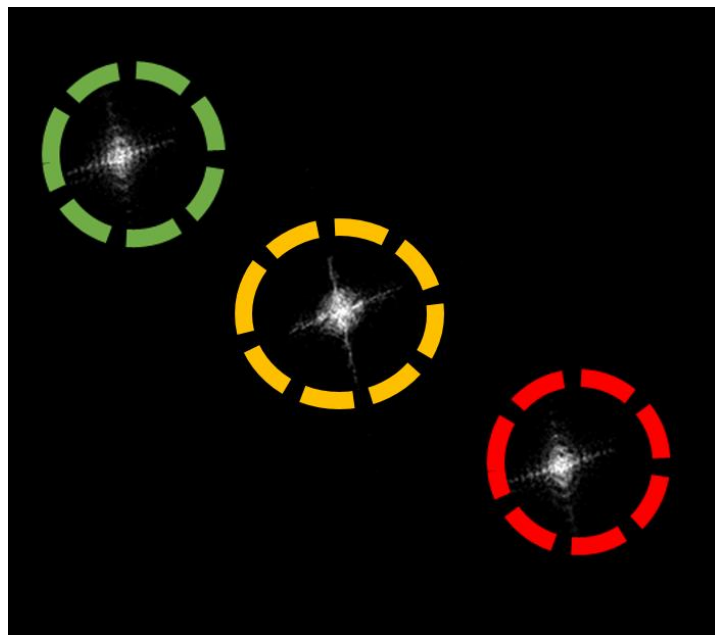


Figure 5.5- FFT of Hologram and Reference Wave Product (1st order mode (green circle, top left), zero order (yellow circle, center)) and 2nd order mode term (red circle, bottom right right) for simulated hologram.

The zero order mode and the mirror image wave-field can then be filtered out by applying circular filters of zeros to the FFT of $H(x,y,z) \cdot R(\theta)$. The simplest way to automate this process is to write the code to find the maximum intensity product- which will always be the zero-order mode, center this and apply the circular array of zeros to filter this. Re-arranging the order to center the next highest intensity section would allow the first order mode to be centered. By now applying a filter of zeros to everything not within the circle containing the first order mode, all of the unwanted terms will be removed and only the first order term remains. The size of the band-pass filter applied around the first order term is important- if too small a filter is used then some spatial frequency components (hence spatial resolution and details) will be lost. If too large a filter is used, then unwanted terms can remain in the reconstruction. The size of the filter will depend on the amount of samples in the Fourier space. For a 640x480 pixel array with 5x zero padding used here, a circular filter of radius 111 pixels was experimentally found to be enough to not affect resolution whilst also not retain any unwanted components. Although this was found experimentally, this would always be enough for this system provided that the off-axis angle in the system separating the terms and the zero padding multiplication factor of 5 do not change, as the relative positions and size of the hologram FFT terms shouldn't change.

Back-propagating the real object wave-field using Eq. 5.8 gives the wave-field of the original object in Fourier space as shown in Figure 5.6

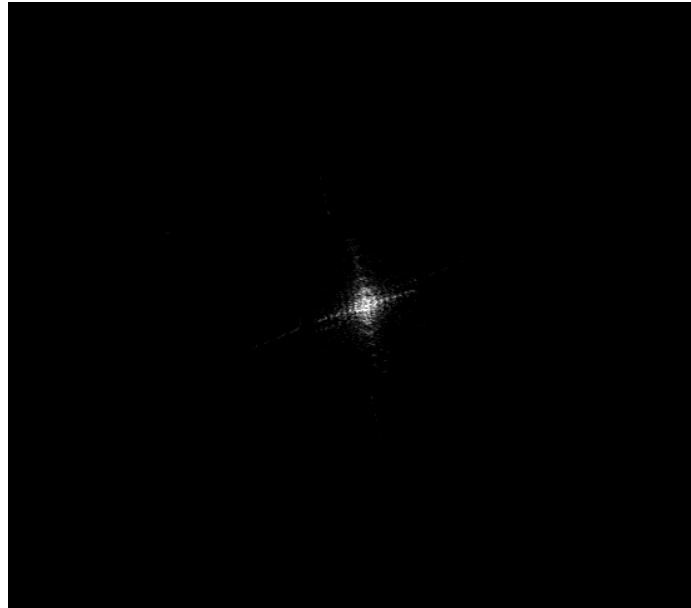


Figure 5.6- Filtered Wave-field of Object and Back-Propagation Kernel product for simulated hologram.

Applying the inverse FFT to this then gives the filtered reconstruction of the original object $O(x,y,z)$ as shown in Figure 5.7.

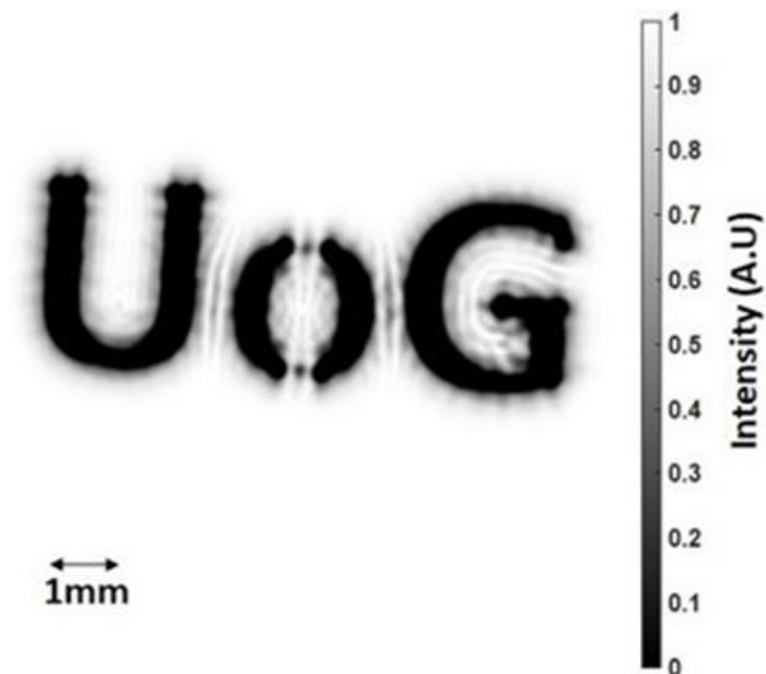


Figure 5.7- Angular Spectrum Reconstruction of Simulated Interferogram of 'UoG' object with features < 1 mm clearly resolved.

The full steps for the reconstruction process are described in algorithmic form by Eq. 5.10:

$$O(x, y, z) = \text{inverseFFT} \left[\text{backpropagation} \left(\text{FilteredFFT} \left(H(x, y, 0) \right) \right) \right] \quad (\text{Eq. 5.10})$$

This can also be described in integral form as shown in Eq. (5.11 - 5.14) where matrix C represents the circular filter of zeros, f_x and f_y are the spatial frequencies in the x/y directions, whilst BP represents the back propagation kernel which acts as a wave propagation transform kernel that accounts for distance z from the detector to the sample object.

$$Y(f_x, f_y) = [C]_{z=0} \cdot \iint e^{-j2\pi(f_x x + f_y y)} \cdot H(x, y, 0) \cdot dx \cdot dy \quad (\text{Eq. 5.11})$$

$$f_{z0} = \sqrt{1 - (\lambda \cdot f_x)^2 - (\lambda \cdot f_y)^2} \quad (\text{Eq. 5.12})$$

$$BP = e^{j \frac{2\pi}{\lambda} \{f_{z0}\} \cdot z} \quad (\text{Eq. 5.13})$$

$$O(x, y, z) = \frac{1}{2\pi} \iint e^{j2\pi(f_x x + f_y y)} \cdot BP \cdot Y(f_x, f_y) \cdot df_x \cdot df_y \quad (\text{Eq. 5.14})$$

A consideration that must be made when using this method is the number of spatial sample points, in order to prevent aliasing.

It's important to note that although there is no minimum distance required for successful reconstruction when using the angular spectrum method, aliasing can occur from under-sampling if the

distance is too large. This is due to the spatial frequency of the hologram being proportional to the distance between the object wave source (the laser beam reflecting or transmitting from object) and the detector. The relationship describing maximum distance to avoid under-sampling using the angular spectrum method is shown below in Eq. 5.15:

$$z \leq \frac{\sqrt{4p_x^2 - \lambda^2}}{2\lambda} (N - N')p_x \quad \text{(Eq. 5.15)}$$

Where N is the total number of pixels and N' is the number of pixels on the detector with incident light on them (giving non-zero values).

The simplest way of preventing aliasing as the distance from the detector to object increases would be to increase the number of pixels. Since the number of pixels in the camera is fixed, this can be achieved through zero-padding [94]. **By zero-padding the samples by a larger number, a larger distance between sample and detector can be used.** This is particularly useful in situations where the distance between sample and detector is unknown or varies.

For the case of the set-up used in this chapter ($\lambda=118.8\mu\text{m}$, 640x480 pixels with 17 μm pixel pitch and assuming a Gaussian beam fully incident within the detector) that a maximum distance of 5.2 mm could be used. However as mentioned in section 5.1 the minimum distance that could be used without the two beams interfering before they reach the FPA was 15mm. By using zero padding to get an array of 5 times the number of x-pixels, this maximum distance could be increased to 26.1 mm.

Using more zero padding results in more computer processing being required but it was found that by using zero padding of 5 times the number of x pixels for

each frame, that aliasing never occurred when moving the sample in the set-up whilst still offering quick processing times.

This method was applied to the experimentally obtained interferogram in figure 4.3 using Matlab code (Appendix 2) which resulted in the actual hologram reconstruction obtained shown in Figure 5.8.

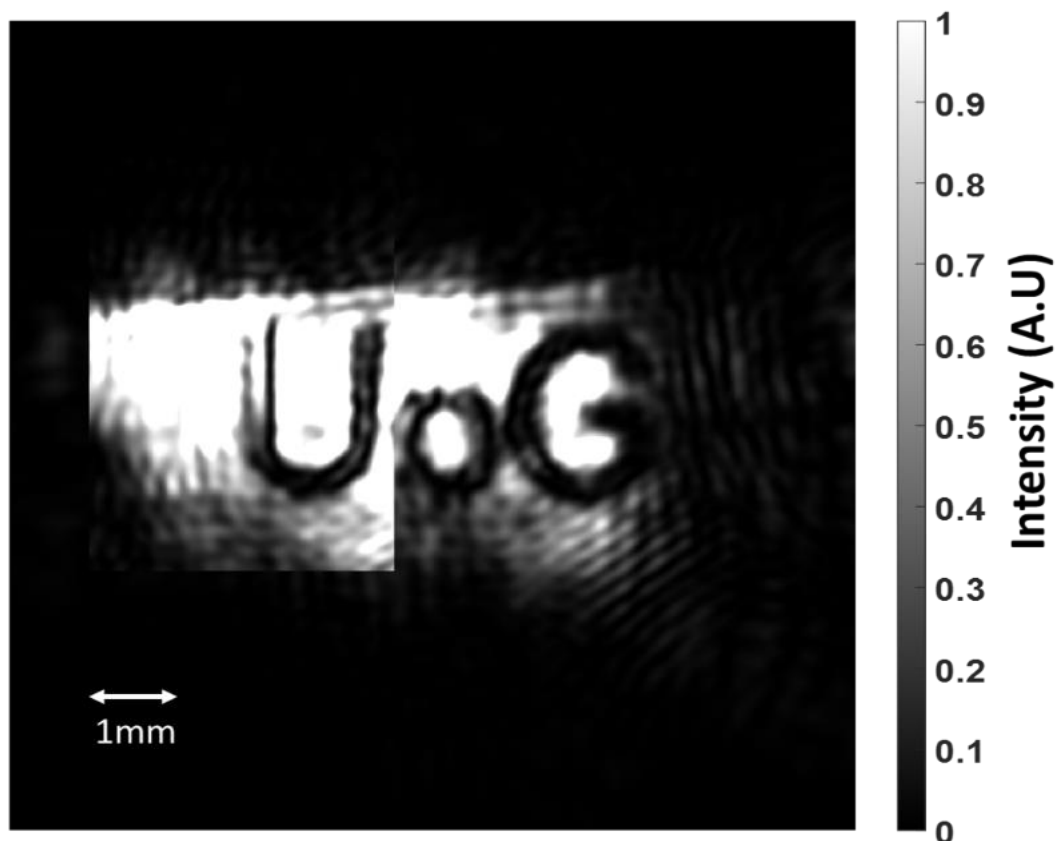


Figure 5.8- Angular Spectrum Hologram Reconstruction of Experimentally Obtained Hologram of 'UoG' sample with features <1 mm clearly resolved.

A comparison between the simulated and experimentally obtained holograms and amplitude reconstructions is shown in Figure 5.9.

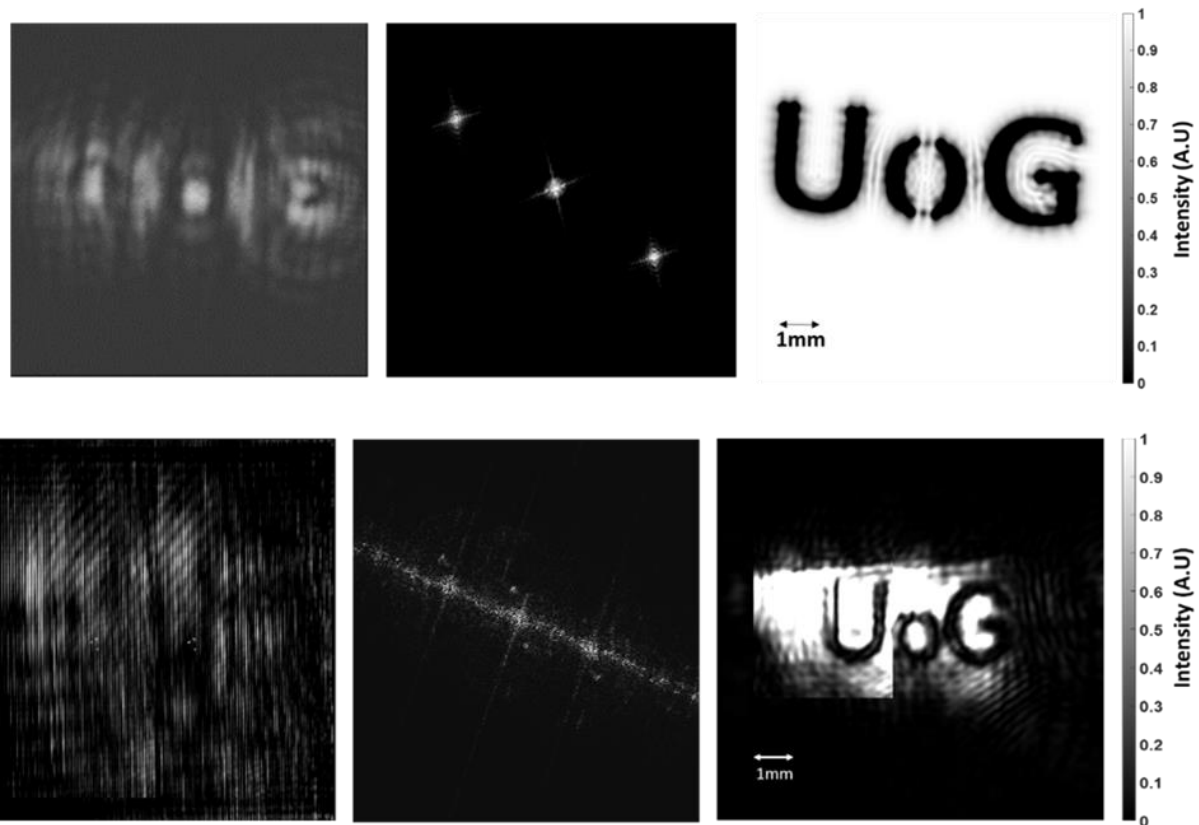


Figure 5.9- Comparison of Simulated (top) – Interferogram (left), Frequency Spectrum (mid) and Reconstruction (right). Experimental (bottom) – Interferogram (left), Frequency Spectrum (mid) and Reconstruction (right). Experimental data varies slightly from simulated due to combination of the laser beam not being fully Gaussian, noise from dead pixels and cross-talk and unwanted reflections at the detector.

Note that the differences between the simulated and experimental data are most likely caused by a combination of the beam profile not being perfectly Gaussian, some reflections at the camera plane, dead/noisy pixels and cross-talk between them in the FPA.

The constantly changing beam profile caused by the highly unstable laser results in intensity changes between each stitched frame of the reconstructed hologram. This causes stitching artefacts when stitching multiple frames because of the laser. This is an inconvenience when stitching together large holograms, however

it would not be a problem in real time video scanning as discussed in Chapter 5. A stable laser source would eliminate this problem all together.

It is important to find the correct distance z as this controls the focus of the hologram as shown below in Figure 5.10.

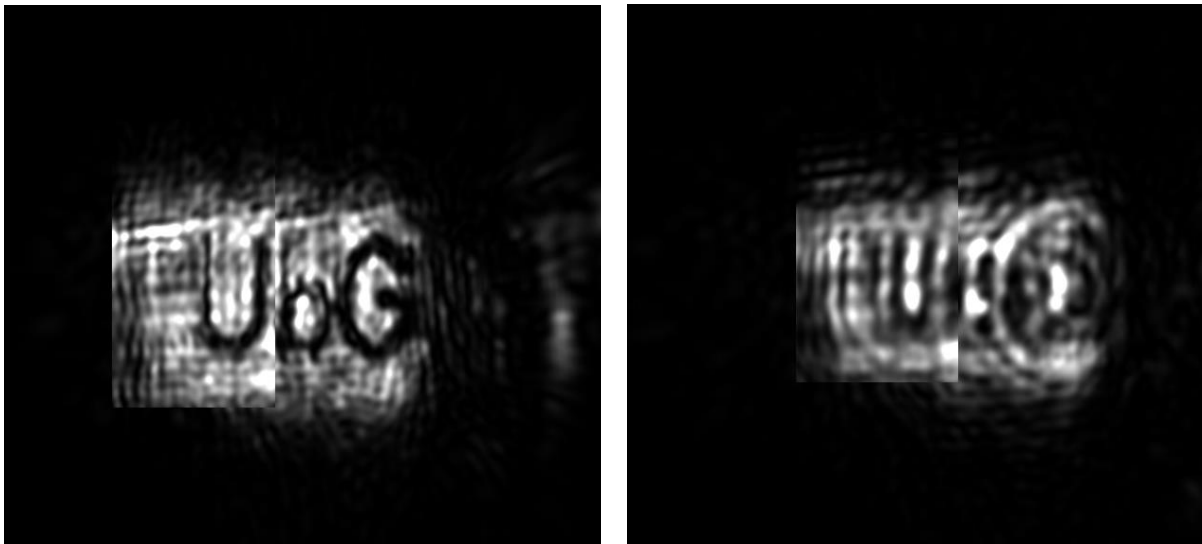


Figure 5.10- Hologram with correct distance $z = 15$ mm(left) and incorrect distance $z = 10$ mm(right) illustrating the effect this has on focus.

Choosing the correct parameters for the off-axis angle x and y components and distance z is done via iterative 'for' loops - this can be time consuming but once found will be fixed for all holograms obtained using this setup assuming the detector-object distance remains the same. The correct z value was chosen qualitatively by eye from what 'looked best' after running several loops of increasingly smaller steps (by first changing z in mm's, down to steps of 1/100 mm's) and deciding where it appeared most focussed (essentially an iterative Newton-like approach). Quantitative methods can also be taken using sparsity of gradient approach- where the gradient modulus is calculated to determine how sharp the edges in the image are [95].

5.4 Performance

The optical performance and limits of the off-axis system using the angular spectrum reconstruction were analyzed. The lateral resolution defines the smallest feature size the system can resolve. This could be found using a USAF target - in this case a 38 mm clear optical path reflective 1951 USAF target (Edmund Optics) was used. This is made of nickel and has no substrate - glass based substrates cause significant absorption and scattering in THz.

An optical image of the target is shown below in Figure 5.11. The yellow highlighted region shows the smallest line pairs that could be resolved with this holography system.

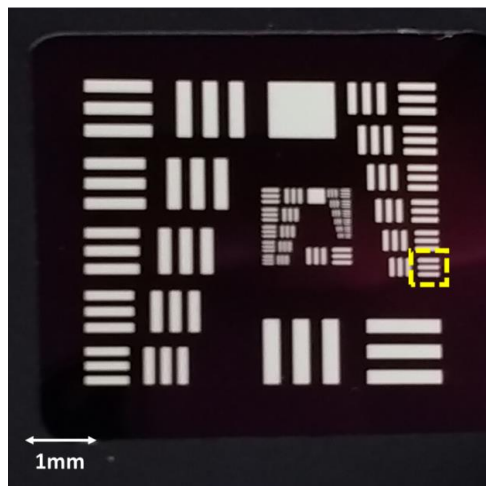
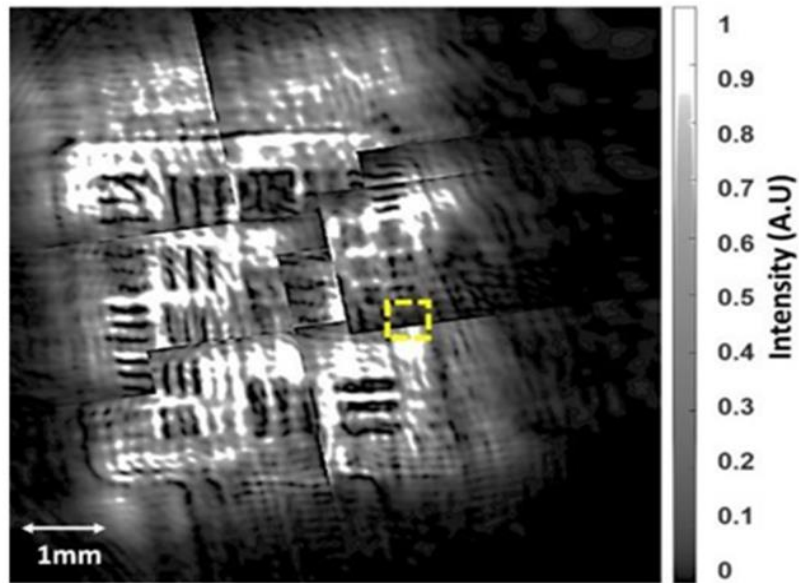


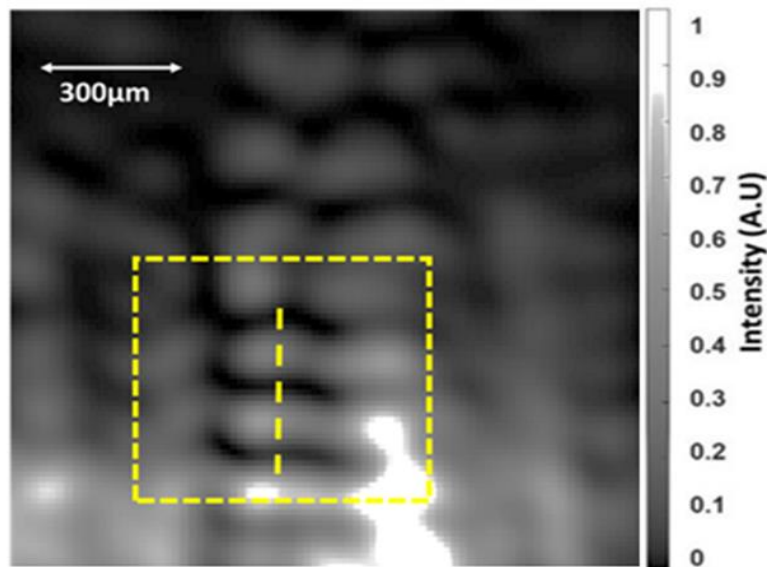
Figure 5.11 - USAF Clear Path Target used to determine lateral resolution limit

The resulting hologram reconstruction was stitched together from 8 holograms (since the sample was too large to image with one hologram) and is shown below in Figure 5.12 (a). The stitching was done by controlling the stages in steps of 17 μm (the pixel pitch) and recording the positions which could then be translated into pixels to choose where to join the holograms.

The highlighted region showing the smallest group of lines that can be resolved is shown in Figure 5.12. Note that the stitching artefacts here are quite noticeable, and like with Figures 5.9 and 5.10, they are caused by the changing laser profile in each frame due to the instability of the laser.



(a)



(b)

Figure 5.12- Reconstructed hologram of USAF target (a) shows full target stitched together from 8 holograms (and featuring some unwanted stitching artefacts due to unstable laser) and (b) a zoom of highlighted region showing where a cross-section was taken for measurement.

This group of lines has a spatial resolution of 3.5 lines/mm which gives a lateral resolution of 280 μm . Hence the system can clearly resolve features as small 280 μm (slightly larger than 2λ). A cross section intensity plot of where the yellow

line passing through Figure 5.12 (b) was taken in order to prove this resolution. This is shown in Figure 5.13.

Cross-Section of USAF Target

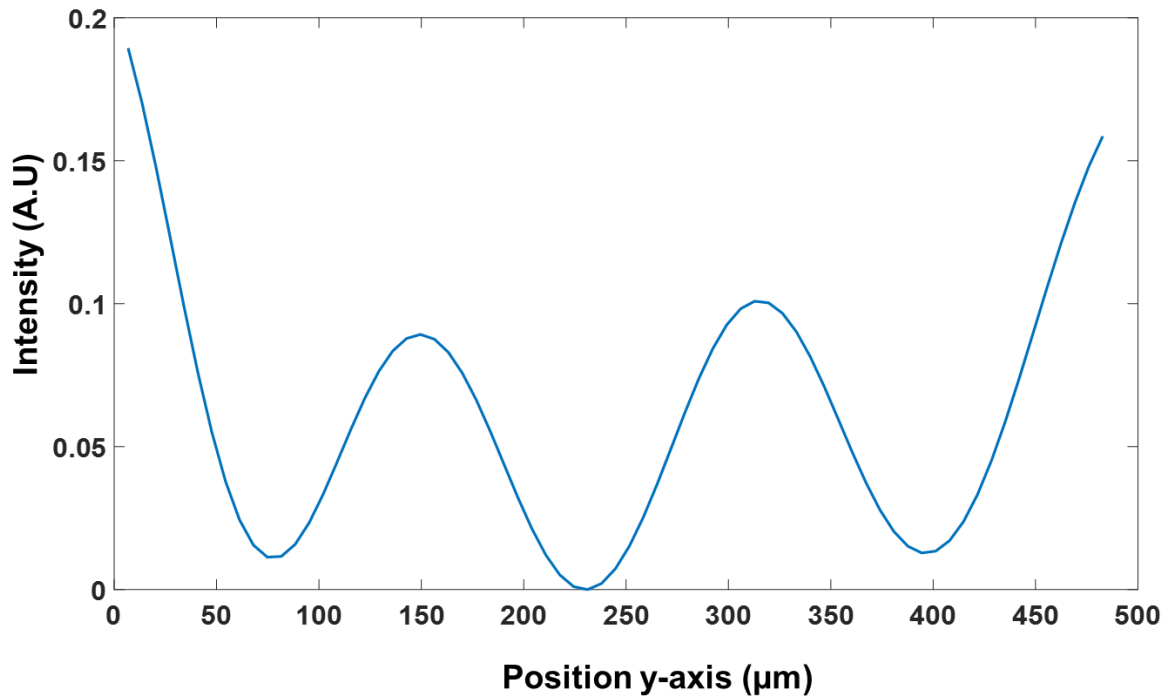


Figure 5.13- Cross-section plot of USAF target from the region marked with dotted line in Figure 5.13 (b)

The modular transfer function (MTF) describes the magnitude response of an optical system in response to different spatial frequencies. It is an excellent figure of merit for a system's resolution as it considers contrast over a range of spatial frequencies.

The modulation transfer MT describes the contrast or ratio of modulation in the image to that in the actual object (i.e. the maximum intensity - minimum intensity in the image). This can be shown in Eq. 5.16:

$$MT = M_{\text{image}} / M_{\text{object}} \quad \text{(Eq. 5.16)}$$

where M is modulation or contrast.

The MTF is therefore the modulation transfer as a function of spatial frequency, f , [96] as shown in Eq. 5.17:

$$MTF(f) = M_{\text{image}}(f) / M_{\text{object}}(f) \quad \text{(Eq. 5.17)}$$

In other words, the MTF describes the modulation/contrast in response to spatial frequency.

The simplest way to find the MTF would be to take cross sections of various spatial frequencies and find the contrast at these. However, a more accurate method for finding the MTF of three bar USAF targets exists (by Boreman et al. [97]). This method accounts for inaccuracies in spatial frequency between the image and object peaks by finding the spatial frequencies corresponding to zeros using the magnitude spectrum, calculating the corresponding object modulation value and using these in Eq. 5.17 to give a more accurate modulation value.

This method was applied to the USAF target hologram reconstruction in order to find the system MTF which is shown in Figure 5.14. The 10% modulation level which defines the system lateral resolution was found at 4 lines/mm or 250 μm . From this it can be stated that the system has a lateral resolution of 250 μm ($\sim 2\lambda$).

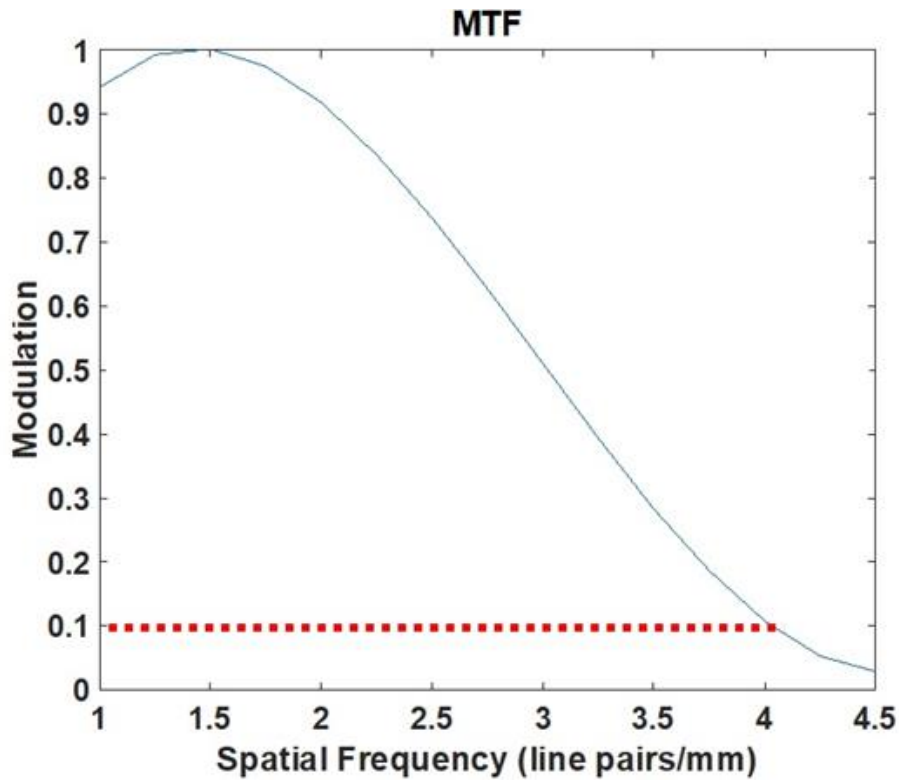


Figure 5.14- MTF of Holography System illustrating the system performance over range of spatial frequencies. Red dotted line gives the cut-off frequency 4 lines/mm equating to a lateral resolution limit of 250 μm

To summarise, in this chapter the holography system setup and process of obtaining a hologram was discussed along with the reconstruction process. The performance of the system was then analysed including obtaining the MTF and spatial resolution of 250 μm . Table 5.1 summarises the system parameters and performance.

6. Real Time Reconstruction and Holography

System Applications:

6.1 Real-Time Video-Rate Terahertz Holography

Successfully recording and reconstructing a THz hologram is beneficial, but in order to be useful for many applications real time recording and reconstruction is essential. As discussed in Chapter 1, there is a lack of video-rate (>30fps) THz imaging systems so being able to use holographic imaging at this speed would be very beneficial, particularly for NDE scanning and biomedical imaging applications. This chapter will discuss how video rate scanning with a THz holography system (video available in thesis data set) was achieved.

The detector used in the holography setup shown in Figure 5.1 (Xenics Gobi 640 camera) can record images at a frame-rate of 50 Hz. All interferogram data recorded on the computer was initially saved to the hard drive and digitally reconstructed offline using Matlab. However, in most applications this is not practical and it would be preferable to read data directly from the camera and reconstruct the holograms in real-time at the camera frame-rate (the bottleneck speed of the system).

In order to test the feasibility of reconstructing hologram video frames in real time, a video of an interferogram of the 'UoG' sample object being scanned along the x-axis was recorded (saved to hard-drive) and reconstructed in Matlab using the angular spectrum reconstruction algorithm discussed in Chapter 5.

The sample object was scanned across the x-y plane at a rate of 2 mm/s using the motorized stage in the setup (as mentioned in Chapter 5). This speed was chosen as it could demonstrate the potential to image a larger area target whilst not being too fast as to not see the sample. Using a lower speed or larger sample proves difficult as the constantly and randomly changing laser profile due to the un-stability of the laser makes it harder to image for longer than few seconds.

The speed taken to reconstruct the hologram video was found by using the built in performance timer in Matlab ('tic/toc') and dividing by the number of frames in the video.

This reconstruction speed was initially very slow at approximately 0.25Hz (for 1000frames which took~4000s) using a standard 64bit windows computer (no GPU, intel i5-6500 processor @3.2GHz with 8Gb RAM). Therefore, a more efficient code was needed.

6.1.1 Hologram Multiplexing Algorithm

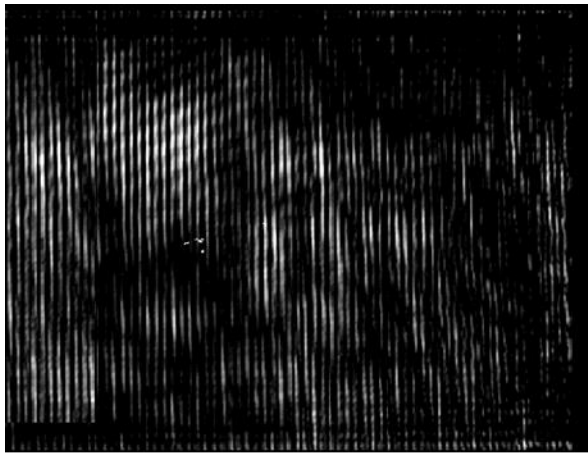
After exploring options for algorithms with faster/more efficient computational performance, an algorithm developed by Girshovitz *et al*, which essentially multiplexes the holograms therefore speeding the reconstruction mechanism, was investigated [98].

In Matlab, the Fast Fourier Transform (FFT) function is quite computationally demanding and hence slows the operation of the holography reconstruction. As mentioned in Chapter 5, the Angular Spectrum reconstruction requires two FFTs (standard and inverse FFT) which makes the process slower. Although

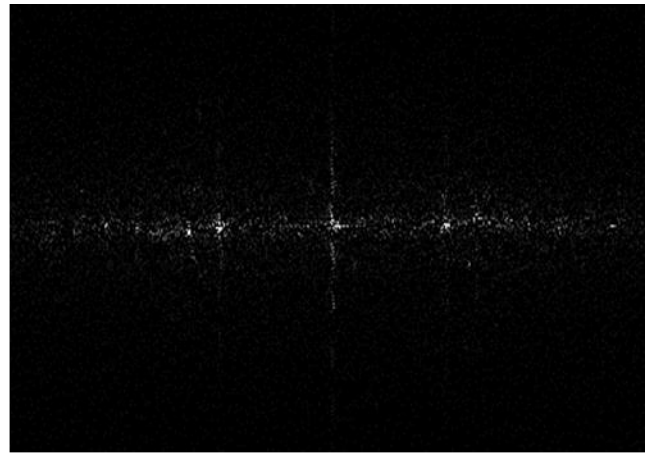
simple Fresnel reconstruction only requires one FFT, so would be faster, the system becomes less flexible and has poorer resolution due to the minimum distance constraint between detector and sample as discussed in Section 5. For this reason, it was best to use the angular spectrum reconstruction method, but also minimise the number of FFTs performed.

Using the algorithm developed by Girshovitz, it was found that the holograms acquired could be multiplexed with the previous frame by rotating one frame by 90° , adding them together and then performing the FFT of these together.

Because one frame is rotated 90° , the terms in Fourier space do not overlap, instead the empty space is used. Figure 6.1 shows hologram 1 with its FFT and hologram 2 rotated with its FFT. Figure 6.2 illustrates how the FFT looks when both these frames are summed first.



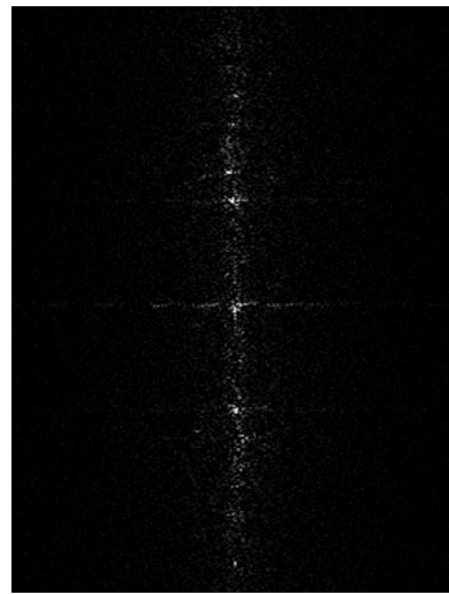
(a)



(b)



(c)



(d)

Figure 6.1- Taking two frames (hologram 1 and 2) and multiplexing them together. (a) shows Hologram 1 and (b) the corresponding FFT. Hologram 2 is rotated 90° and shown in (c) along with the corresponding FFT (d).

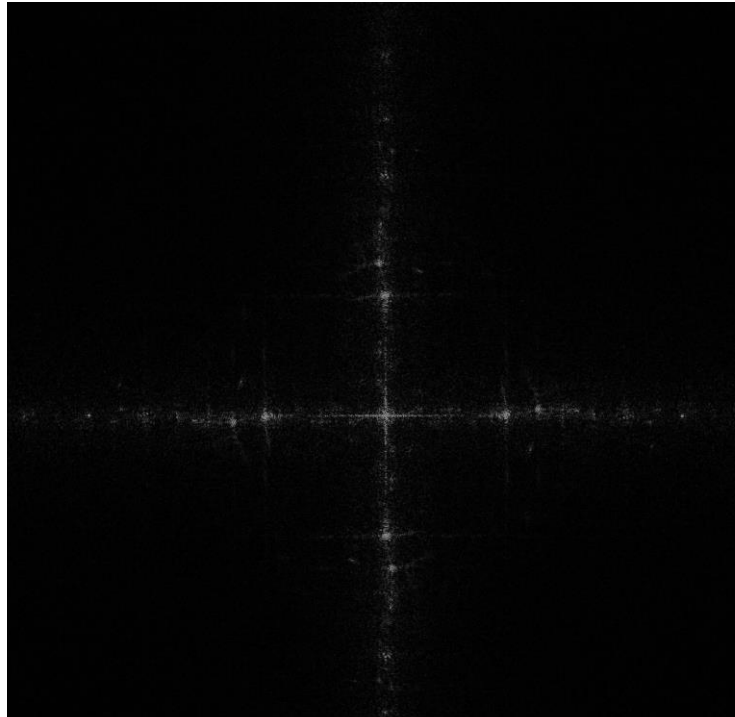


Figure 6.2- FFT of multiplexed Hologram 1+ Hologram 2 (after it is rotated 90°)

This would essentially half the processing time needed for the first part of the hologram (up until the inverse FFT). However, two inverse FFTs would need to be included so this would only decrease the processing time by 25% (as 3 of 4 FFTs must still be performed).

Following on from this, to further increase the speed, the filtering of the unwanted terms and re-shifting of the FFT to centre could be eliminated. It was easier to find the location of the first order terms from frame n and frame $(n+1)$, then crop these. This allowed for performing the inverse FFT directly on these terms, removing the steps shifting of the frequency spectrum and having to filter these.

By further cropping the size of the section for the inverse FFT, it was found that a higher performance speed could be obtained with no negative impact on image reconstruction quality.

It should be noted that the original zero padding size affects the speed of the first FFT. The zero padding is important since it increases the number of spatial points, hence spatial frequency and spatial resolution. It was found that zero padding by a factor of 5 (so 3200x2400 samples for the 640x480 pixel camera) yielded the best performance speed to resolution trade-off. As mentioned in chapter 5, for the parameters in this system a zero padding factor of 5 allows for 26.1mm stand-off distance between the detector and sample without any aliasing effects. The distance used for the sample to detector was 15mm, so the zero padding factor of 5 allowed for some extra distance between sample and detector to be used if necessary. Zero-padding of anything higher than a factor of 5 wasn't necessary and resulted in slower reconstruction speeds so wasn't used here.

The method for this multiplexing and cropping algorithm is shown in Figure 6.3. This method resulted in a computational speed of approximately 2.86 Hz (1000frames in 350s) almost an order of magnitude faster than the original frame-rate with no cost of resolution and no extra computing power needed.

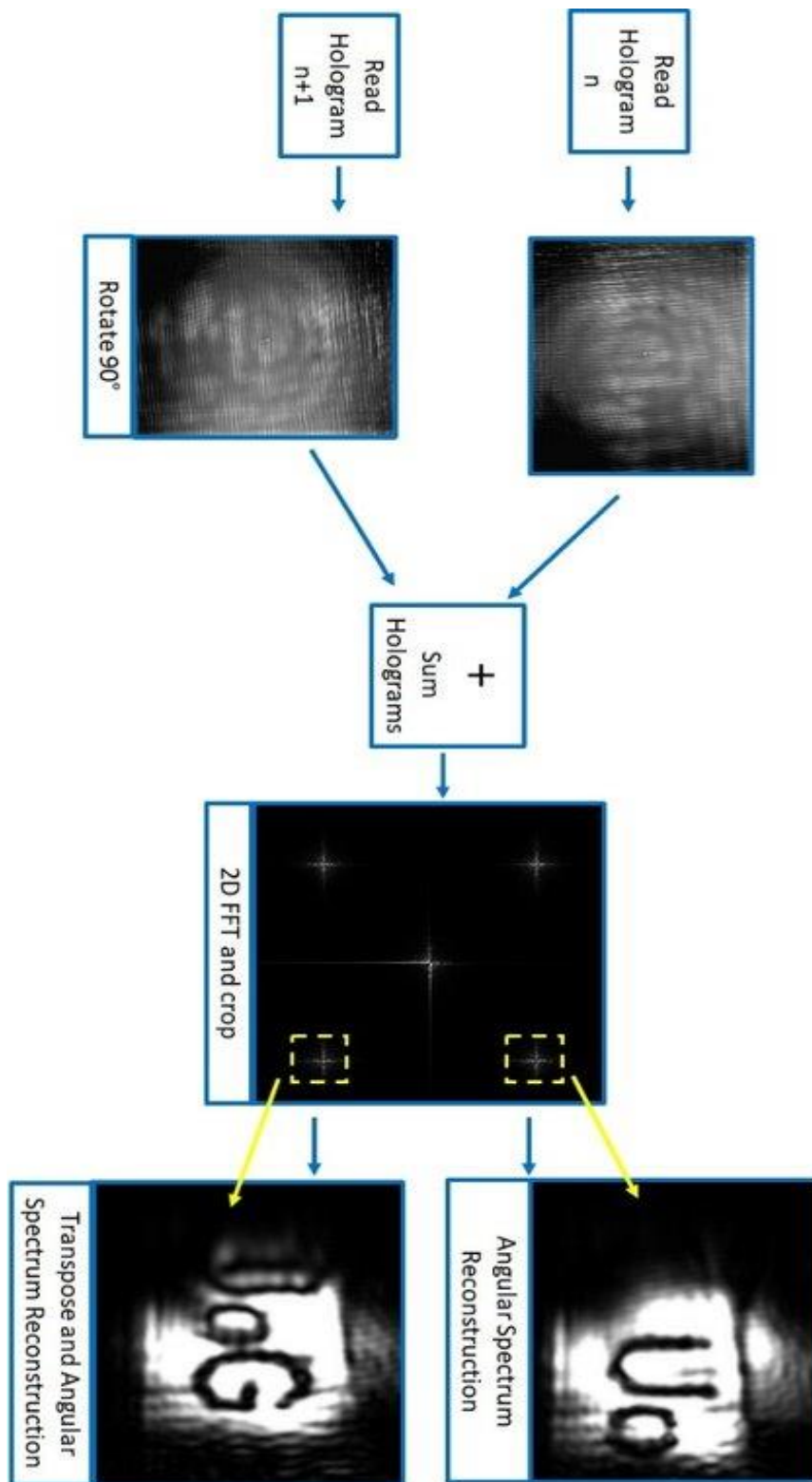


Figure 6.3- Step by step guide of the hologram multiplexing algorithm as first conceived by Girshovitz [98] and used to speed up reconstruction speed in system by an order of magnitude.

In order to further improve reconstruction speed, the use of graphics processor units (GPUs) was explored. The Matlab code used for the multiplexing algorithm performed with a computer with GPU is in Appendix 4.

6.1.2 Enhancing Performance with GPU

In order to further increase the speed of the hologram reconstruction so that it's closer to video-rate (>30Hz), more computing processing power was needed. The use of GPUs in Matlab for carrying out fast, real-time calculations has become common practice and Matlab even has a convenient GPU array toolbox that allows for easy manipulation of code in order to benefit from the GPU processing.

By using the 'gpuArray' function in the parallel computing toolbox, GPU-enabled MATLAB®, all of the processing and Fourier Transforms can be performed on a GPU drastically increasing performance speed.

The choice of GPU is an important consideration as there is a wide variety of GPUs available for various markets and price ranges. A pair of commercially available GPUs was chosen, the NVidia Titan XPs which were linked via SLI Bridge. These were selected as they offered some of the highest performance speeds for calculations at a relatively inexpensive cost (~£1000 each). These were then used inside a commercially available PC- Asus (~£1000). This resulted in a total cost of £3000 for a commercially available, non-specialist computer.

Using the multiplexing algorithm (Appendix 4) in this computer resulted in a massive increase in reconstruction speeds- with frame rates of over 57Hz (1000 frames in 17.5s).

When reading from the Xenics camera directly from the frame-grabber (Teledyne Dalsa) reconstructions were performed in real time at a steady frame-rate of 50Hz (the operating frame-rate of the camera).

This meant that real time imaging and reconstructions could be performed at video rates (50Hz) from the camera stream. In order to compare the performance speed of reconstruction without a GPU or multiplexing algorithm, with multiplexing algorithm and with the multiplexing algorithm and GPUs, a graph is shown in Figure 6.4.

It's important to remember that **a zero padding factor of 5 was used which means that the maximum stand-off distance between the sample and detector that can be used when reconstructing holograms at a speed of 50fps is 26.1mm.** Larger distances may be used but at the cost of reconstruction speed.

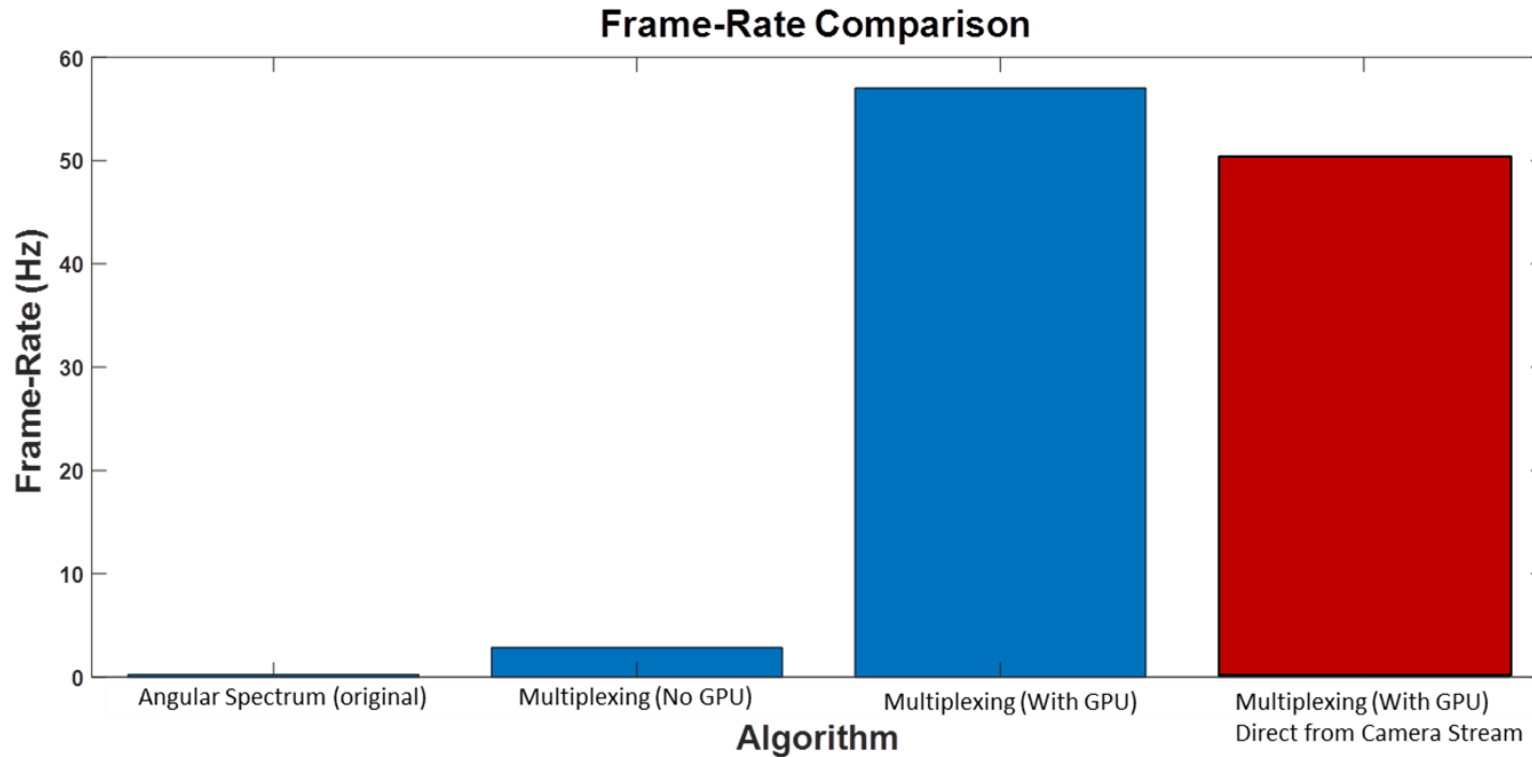


Figure 6.4- Comparison of reconstruction algorithm speeds with no multiplexing (original hologram reconstruction method), multiplexing without a GPU, multiplexing with a GPU and multiplexing with a GPU reading straight from the frame-grabber (as would be done for real time imaging). The multiplexing algorithm makes it significantly more efficient than without and using this with a GPU gives a massive performance increase allowing the system to comfortably operate at 50 fps when reading from the frame-grabber in real-time.

6.2 Terahertz Holography Application: Scanning Concealed Objects

THz radiations long wavelength properties make it ideal for penetrating through many materials that are optically opaque in the visible band. As discussed in Section 1, many materials such as polymers, paper and wood can be highly transparent in the THz region making it possible to see through them. One of the most sought after THz applications is to be able to see through visibly opaque materials both for non-destructive evaluation quality testing and to find concealed objects for security reasons.

In order to analyse potential concealed object detection, it is useful to know the reflection, absorption and transmission characteristics of materials at the relevant wavelengths.

Extensive studies on THz radiation on dielectric properties of materials have been carried out before- particular on polymers [97- 99].

Spectrometry performed on polymers over ranges of 2-10THz show that refractive indices can vary from 1.523-1.817 and absorption co-efficient from $\sim 0-220\text{cm}^{-1}$ [99]. Results are shown below in Table 6.1

<u>Material</u>	<u>Refractive Index</u> <u>Range</u>	<u>Absorption</u> <u>Coefficient Range</u> <u>(cm⁻¹)</u>
Polyethylene (LDPE)	1.523- 1.526	~0
Polyethylene (HDPE)	1.522- 1.525	~0
Polytetrafluoroethylene(PTFE)	1.312- 1.755	0-500
Polyamide-6 (PA6)	1.587- 1.817	60-250

Table 6.1- Refractive indices and absorption co-efficient of materials over 2-10

THz range

Polyethylene (also called polythene or PE) can be broken down into two categories – low density (LDPE) and high density (HDPE). Both LDPE and HDPE are widely used as packaging materials and show almost zero absorption in the 2-10 THz region.

In contrast to this, polytetrafluoroethylene (PTFE or Teflon®) and polyamide-6 (PA6) show extremely high absorptions at certain frequencies- this could be due to their polar bonds and helical structure giving them very different physical properties from materials like polyethylene. Interestingly, within 2-3 THz PTFE does show almost negligible absorption which is an interesting anomaly that has been noticed before for this material [100].

This would suggest that at 2.5THz, Teflon sheets may be transparent and possible to image through. Based on other THz experiments, this has been done

before [101]. Along with this, low density polymers such as PE should have very high transmission and be almost transparent. However, PA6 would be expected low density polymers such as PE should have very high transmission and be almost transparent.

Since many packaging types are typically made of low density polymers such as PE, the THz holography system could potentially be used for imaging reflective targets through these. To verify this, common packaging types such as polythene bags, paper envelopes and cardboard boxes were assessed using an FTIR spectrometer (Bruker IFS 66v/S) in the lab.

The system was used in transmission mode and the transmissions of materials tested at 2.52 THz are shown below in Table 6.2.

Material	Transmission (%)
Polythene package 1	96.2
Polythene package 2	95.7
Cardboard package 1 (thick)	59.8
Cardboard package 2	67.2
Paper Envelope 1	92.1
Paper Envelope 2	93.3

Table 6.2- List of packaging materials tested with FTIR Spectrometer and corresponding transmission at 2.52 THz

From this testing, it could be assumed that at 2.52 THz imaging in reflection mode through polythene or paper packaging may be possible, whilst with thicker cardboard materials would be expected to cause significant absorption, reflection or scattering.

The off-axis reflection mode THz holography system proposed in this thesis would be ideal for finding concealed metallic objects in these types of packaging- especially when you consider the fast, real-time, video-rate scanning that could be done to quickly and safely check packages. Metallic objects such as weapons or parcel bombs could be whilst the system could also be used for non-destructive evaluation of packaged objects for quality check.

In order to test the feasibility of such applications, the metallic 'UoG' object was placed inside two common packaging types. A standard polythene delivery package with a transmission of 95.7 % at 2.52 THz was used along with a paper envelope with transmission of 92.1% at 2.52 THz. The schematic of the system is same as shown in Figure 5.1 with the same object-detector distance and angles. The resulting hologram reconstruction of the 'UoG' sample inside both packaging types are shown in Figure 6.5.

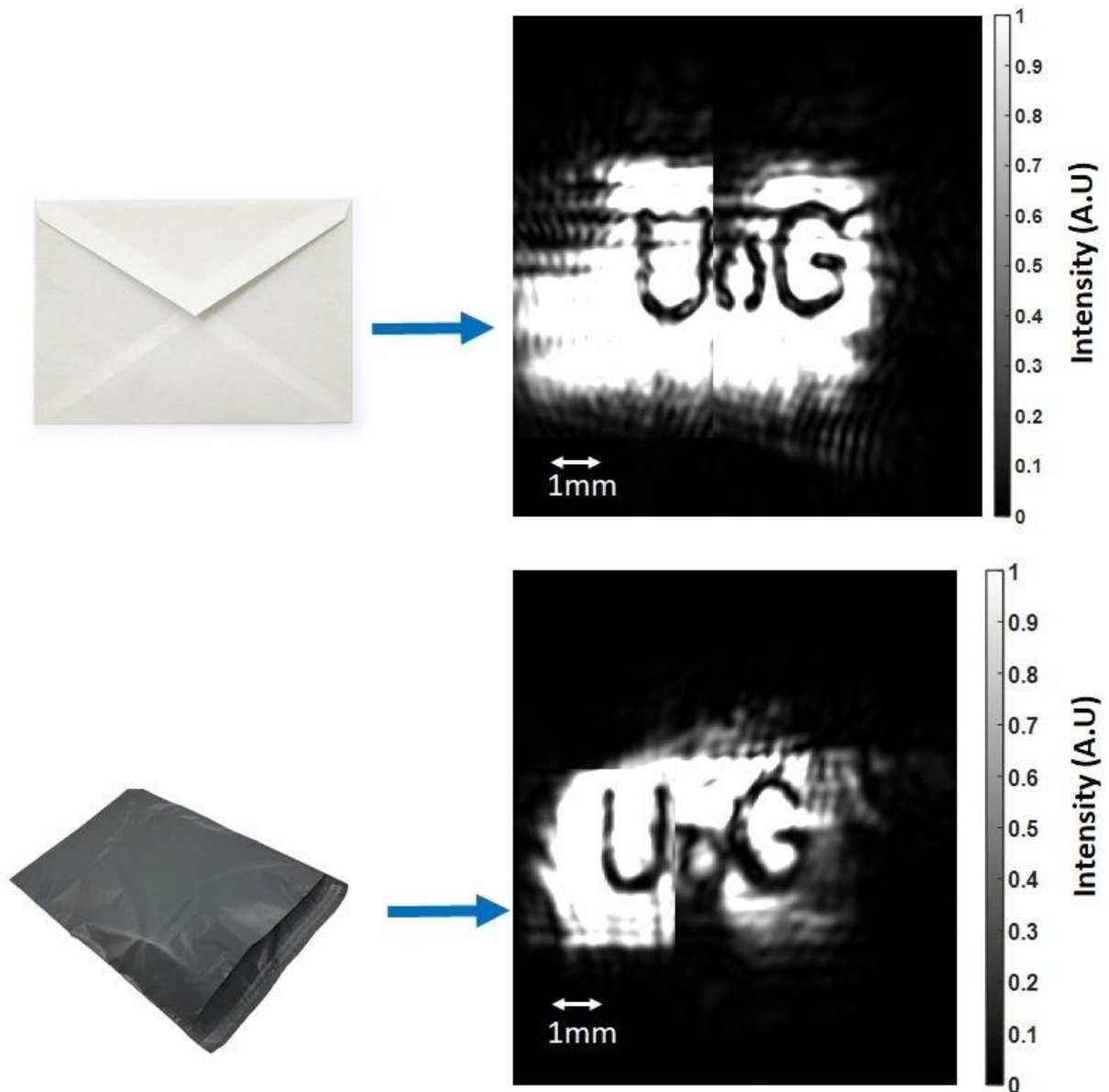


Figure 6.5- Reconstruction of hologram of 'UoG' object concealed in polythene (top) and paper (bottom) packaging. Both of these materials are easy to detect the metallic sample object through

From Figure 6.5 it can be seen that the detector can easily identify the concealed objects with only a small amount of reflection loss- the object is still very clearly identifiable. This highlights the potential of using this holography system as a package inspection tool for these particular materials.

6.3 THz Holography Application: 3D Depth Imaging

As discussed in chapter 2, one of the most interesting and useful features of holographic imaging is the ability to get depth information of a sample obtained from the phase information. Most of the hologram reconstructions shown so far have shown just the 2D amplitude, which provides a 2D image.

In digital holography, obtaining 3D information becomes more difficult as the phase information is ‘wrapped’. This phenomenon is briefly mentioned in Chapter 4. In coherent imaging, phase extraction algorithms usually result in a series of discontinuities within the harmonic function. For a continuous phase $\Phi(t)$, when being processed, sampling between the phase range $[0, 2\pi)$ must be used in order to perform a Fourier Transform. This results in jumps of 2π causing spikes and changes from the true phase. The phase with these 2π ambiguities in the signal is referred to as ‘wrapped’. The process of ‘unwrapping’ can be applied by a variety of methods in order to obtain the true phase [102]. To date there is no full method/solution to unwrapping phase in all situations, but there are some solutions that could be used in holography.

In holography, the problem caused by 2π ambiguities is present whenever the thickness/steps are greater than the wavelength of the source. The most common method to eliminate this is by using two sources with different wavelengths to create an artificial wavelength λ_a as shown in Eq. 6.1 [103]:

$$\lambda_a = \frac{\lambda_1 \lambda_2}{\lambda_2 - \lambda_1} \quad \text{(Eq. 6.1)}$$

However, this dual wavelength approach would not be suitable for this system as the laser source is not tunable and can only emit at a single wavelength.

The other option would be to use a computational phase unwrapping algorithm. There is a variety of phase unwrapping algorithms that do not require a-priori knowledge of the sample object [104-106] however they can be computationally demanding and would detract from the fast, real-time operation of this system. A faster, real time algorithm for phase unwrapping could be developed but such a complex algorithm would require a thesis in its own- the possibility is however discussed in Chapter 6 in the Further Work section.

The option used, in order to prove this system could measure phase depth without 2π ambiguities, is simply to use an object with features less than $\lambda/2$ deep.

To test optical thickness, a glass 1951 USAF target was used as a photomask in order to make a copy of the sample on a HRFZ-Si wafer (since this is partially reflective in THz). This is the same material as the beam-splitter in the system, so the reflection of this material at 2.5THz can be expected to be $\sim 45\%$. The transmission was then verified for the wafer using an FTIR spectrometer (Bruker IFS 66v/S).

The USAF pattern could then be dry etched into the wafer to have a depth of less than λ . Here the sample was dry etched to have a thickness of $40\mu\text{m}$ for the pattern features. The actual thickness was found to be $40.6\mu\text{m}$ when measured using a Bruker Contour surface profilometer. An image taken of a section of the

USAF target and plots of the depth profiles along the x and y axis are shown in Figure 6.6.

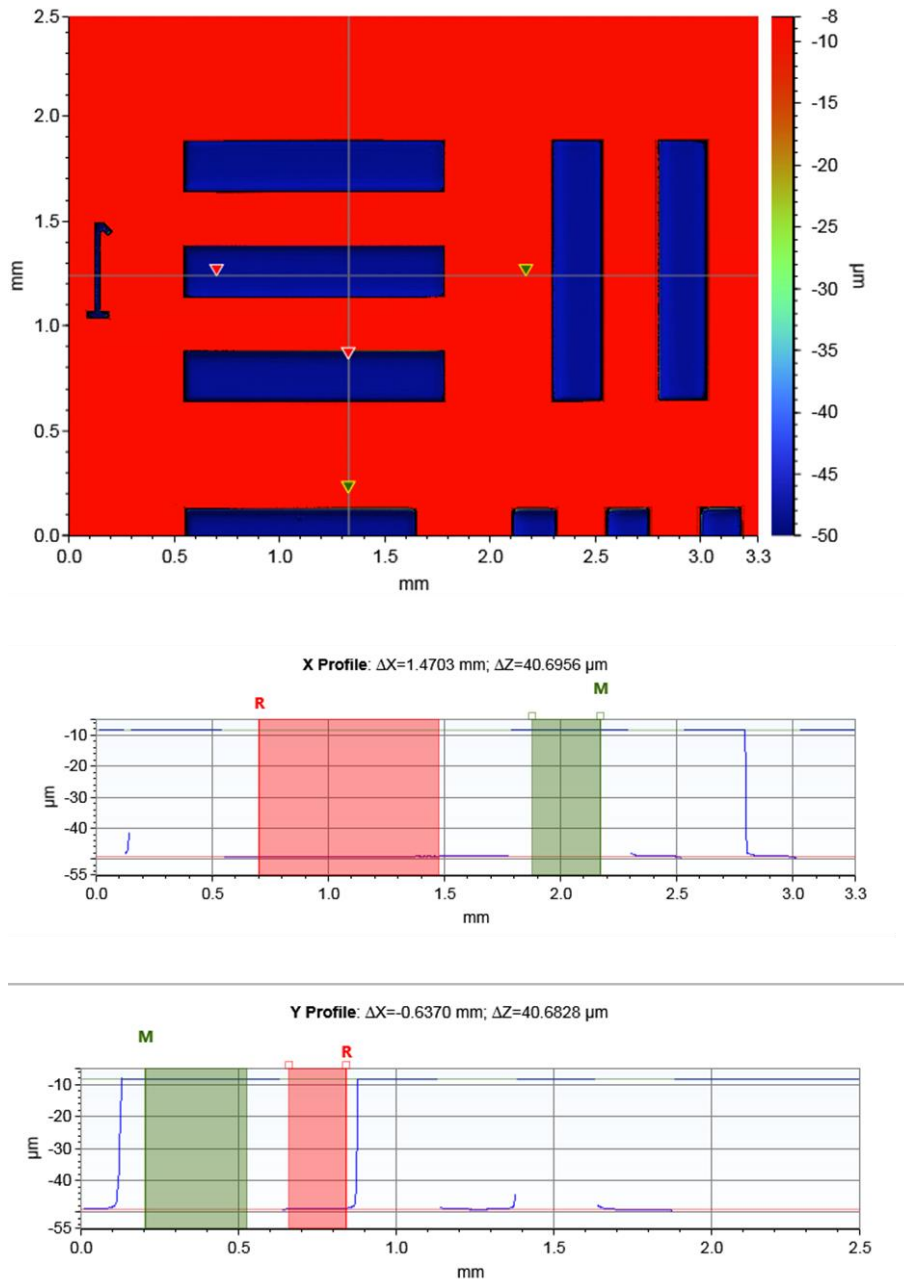
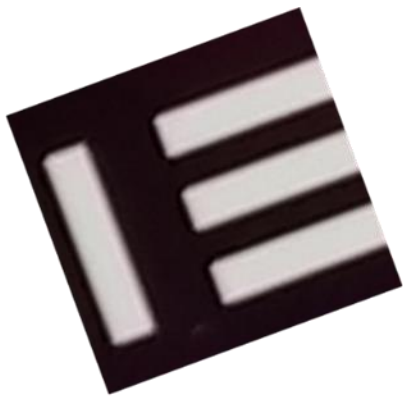
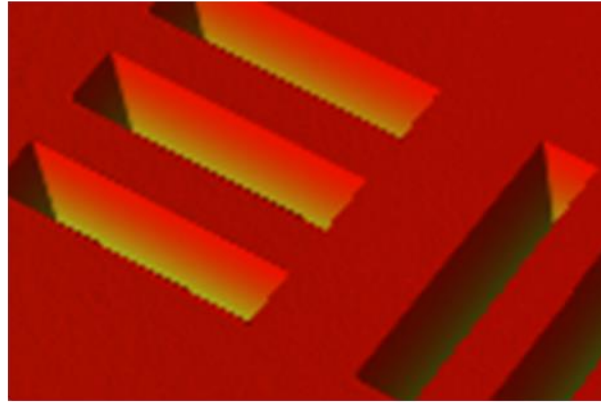


Figure 6.6- HRFZ-Si Wafer with 40µm Deep Etched USAF Target Pattern where top image shows optical image of section, the middle id depth profile along x-axis (showing etch depth of 40.6956 µm) and the bottom showing depth profile along y-axis ((showing etch depth of 40.6828 µm)

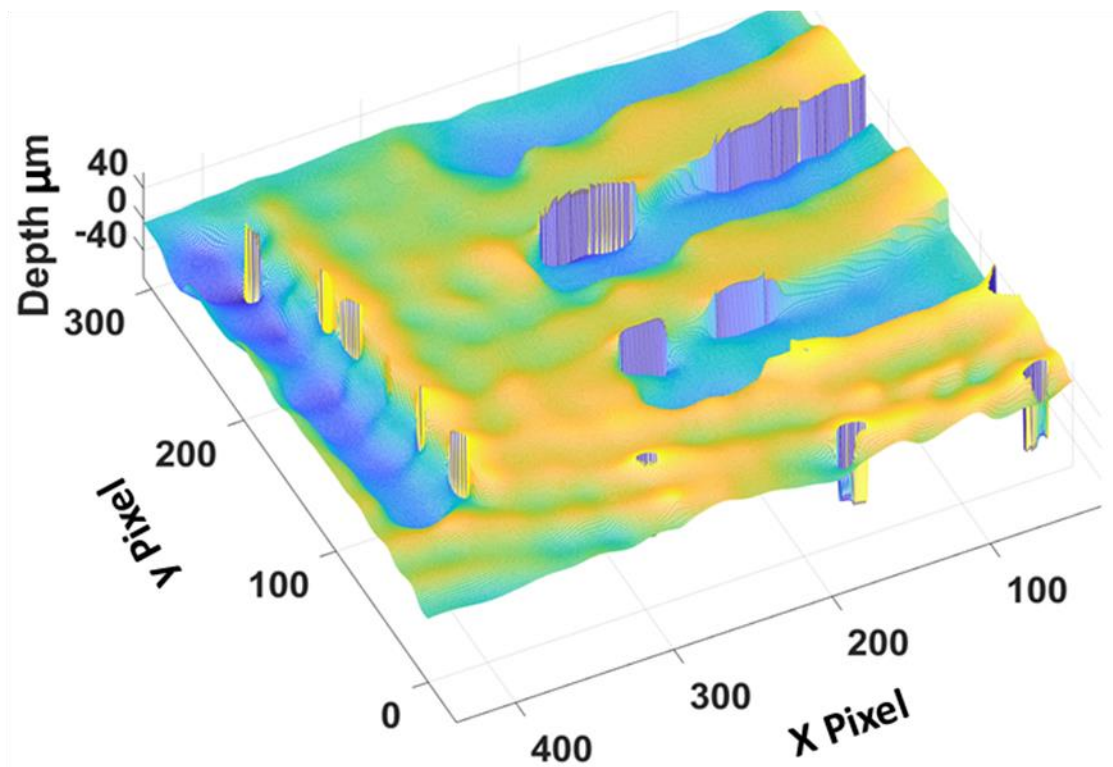
A hologram of the etched target was then obtained using the off-axis holography system with the same arrangement and angular spectrum reconstruction code as in chapter 5. However, this time the wrapped phase reconstruction was obtained as opposed to the amplitude (the code remains the same but the phase information is displayed). To minimize phase ambiguities due to the constant changing laser profile from the unstable laser, a single section of the USAF target was obtained from one image rather than stitching together. An optical image of the section from the original USAF target, along with the image obtained on the surface profilometer of the etched HRFZ-Si target and the resulting phase reconstruction of the hologram of this target are shown in Figure 6.7. It can be seen there are no 2π ambiguities and the phase appears to be ‘unwrapped’ despite no unwrapping algorithm being used due to the thickness being less than $\lambda/2$.



(a)



(b)



(c)

Figure 6.7- optical image of USAF Target Section in (a), a surface profilometer image of the same section on HRFZ-Si etched target in (b) and phase reconstruction of the same section of an experimental hologram of the same 40 μm-deep etched HRFZ-Si target in (c)

The depth in Figure 6.7 was converted from phase to distance (in μm) by using Eq. 6.2 [107]:

$$d = \frac{\Phi\lambda}{2\pi(n-1)} \quad (\text{Eq. 6.2})$$

Where n is the refractive index of the HRFZ-Si wafer (~ 3.416) and Φ is the phase (in radians). The depth of the etch was found to be between $40.1\mu\text{m}$ for the average depth at the center of features which closely matches the $40.6\mu\text{m}$ of the profilometer tool.

By using the mean phase step between adjacent pixels as the resolution (phase) and converting it to depth (μm), the depth resolution was found to be

$d_{\text{res}} = 0.9\mu\text{m}$. For the wavelength of the source ($118.8\mu\text{m}$) this means that a depth resolution of $\lambda/132$. This compares closely to leading visible light holographic microscopy techniques ($\lambda/136$) [108].

Achieving this depth resolution suggests that this THz holography approach could potentially be used as a surface profilometer tool. This could potentially be useful for applications where it would be necessary to image the sample in reflection mode, but where visible or infrared radiation would be absorbed or scattered. If a stable laser was available, video rate 3d depth holograms would be possible without large phase shifts caused by the laser beam profile constantly changing.

7. Conclusion:

7.1 Summary of Thesis

To summarize, in this thesis current THz imaging technology and the background theory to understand digital holography are discussed (chapters 2 and 3). A THz digital holography system is designed in the off-axis reflection mode set-up (chapter 4) which was then implemented and used to obtain digital interferograms, with suitable reconstruction algorithm which allows for a lateral resolution of $250\mu\text{m}$ (chapter 5). The reconstruction algorithm was improved using hologram multiplexing and further improved through the use of GPUs in order to achieve real time video-rate image reconstruction at 50Hz with movie scanning capabilities demonstrated (videos in thesis data-set) (chapter 6).

Other potential applications for a THz holography system such as an NDE tool for concealed metallic objects are successfully demonstrated along with use as a surface profilometer at THz frequencies achieving depth resolution of $\lambda/132$.

7.2 Limitations and Possible Improvements

Although many of the results demonstrated from this system show future potential as a legitimate imaging tool, there are many limitations using this THz holography approach.

By far the biggest constraint on the system performance is that of the laser - the stability issues, power limitations, lack of tune-ability and impractical size of the

optically pumped THz lasers have significant negative effects on the system performance and practicality. The cost alone of the laser used is ~£100k which defeats some of the arguments about this approach being 'low cost' by avoiding the use of lenses.

The development of improved, higher power THz QCLs would allow for greater stability, greater quality of hologram and a larger NA. The stability of the laser was a major problem both when stitching images together due to the laser profile causing unwanted artefacts, and when scanning videos due to constant flashing (shown in videos in thesis data set).

Having a wavelength tune-able THz laser would also allow dual wavelength reconstruction, which would enable unwrapped 3D phase depth holograms of optically thick objects with thicknesses greater than $\lambda/2$ to be obtained without any 2π ambiguities or prior knowledge of sample needed.

As discussed in chapters 4 and 5, the lateral resolution achieved by the system is highly dependent on the pixel pitch and number of pixels. Having a larger FPA with a higher number of pixels and smaller pixel-pitch could result in better resolution and have a larger NA. Increasing the number of pixels would also allow for a larger stand-off distance as there could be less pixels under incident light whilst still allowing the full hologram to be recorded (although this could also be achieved by further zero-padding at the cost of computation time/frame-rate when reconstructing the holograms). A more sensitive detector would also allow for less laser power to be needed and offer the possibility of wider field of

view due to the higher NA and ability to expand the beam more without concern of limiting the power too much to be detected.

The reconstruction speed of the system is also limited to that of the camera (it cannot be faster than the data-stream). This could be considered the bottleneck speed of the system. A camera with a faster native frame-rate would allow for the opportunity to increase reconstruction frame-rates higher.

It is a fair question to ask, since one of the main benefits of this system is that it uses an LWIR microbolometer FPA, that if better THz laser sources and detectors were available to improve the holography system, would it be necessary to use holography at all?

The potential to simultaneously obtain depth information with amplitude, the convenience of not needing any expensive and often lossy THz optical components (such as lenses) and the compactness of system that could be used (if a smaller laser is available) mean there could still be advantages for using a real-time holography system for THz imaging, if better detector and sources become available.

Perhaps a more important question is the needs for imaging with THz radiation in the region of ~ 2.5 THz ($118.8 \mu\text{m}$) over mm-wave radiation. As discussed in Chapter 3, using frequencies in this order for imaging has some advantages over mm-wave approaches and there has been suggestion of possible applications, but as of date there is no major and highly desirable imaging application that can only be done at frequencies of ~ 2.5 THz and not also with other frequencies.

Many of the applications suggested could also be done with mm-wave technology, perhaps with lower resolution but at potentially lower cost or easier integration.

A fair summary and conclusion could be that, **there aren't currently many applications where imaging with THz radiation ~ 2.5 THz is required over mm-wave radiation. However, provided that a sufficiently powerful and stable source becomes available, real-time digital THz holography could provide a good option for imaging at these frequencies if required- especially for 3D depth or surface profiling applications.**

7.3 Further Work

Given more time, the piece of work I would most liked to have investigated would be exploring solutions for a fast algorithm to unwrap phase in real-time - obtaining full 3D depth THz images in real time with no 2π ambiguities would have allowed for thicker objects to be measured/imaged and could have been extremely useful. Development of phase unwrapping algorithms for digital holography is still a very active area of research and such a task could have been a thesis in its own right.

Other than this, most of the work that would improve this system would be on having higher power, more stable, coherent sources and more sensitive detectors with larger FPAs (more pixels) to allow for more options such as wider FoV, better image stitching/less artefacts when stitching images or scanning in video-mode, and allowing further stand-off distances.

Appendix 1.1: Matlab 1/e Divergence Beam

Profile Code

1/e divergence and roundness:

```
%start/input
```

```
clear all;
```

```
close all;
```

```
%inputs
```

```
I=double(imread('89.bmp')); %Xenics image file goes here
```

```
f=10e3; %mirror focal length in um
```

```
pixelpitch=30; %pixel pitch in um for Xenics
```

```
es=1-(1/(exp(1))); %(1-1/e^2)
```

```
lambda=118.8; %wavelength in um
```

```
%%if test needs has RGB data use line below
```

```
if size(I,3)==3
```

```
I = rgb2gray(I);
```

```
end
```

```
% normalise:
```

```
I=I/(max(max(I)));
```

```
%%%%%%%%%%%%%%%%%%%%%%%%%%%%%%%%%%%%%%%%%%%%%%%%%%%%%%%%%%%%%%%%%%%%%%%%script%%%%%%%%%%%%%%%%%%%%%%%%%%%%%%%%%%%%%%%%%%%%%%%%%%%%%%%%%%%%%%%%%%%%%%%%
```

```
%%%%%%%%%%%%%%%%%%%%%%%%%%%%%%%%%%%%%%%%%%%%%%%%%%%%%%%%%%%%%%%%%%%%%%%%
```

```

%1- [process image]

%threshold image
bw = imbinarize(I);
imshow(bw)

%%noise removal
% remove all object containing fewer than 30 pixels
bw = bwareaopen(bw,10);

% fill any holes, so that regionprops can be used to estimate
% the area enclosed by each of the boundaries
bw = imfill(bw,'holes');
imshow(bw)

[B,L] = bwboundaries(bw,'noholes');
%find largest element:
[max_size, max_index] = max(cellfun('size', B, 1));
B=B(max_index);

%2 [find boundaries]
% Display the label matrix and draw each boundary
imshow(label2rgb(L, @jet, [.5 .5 .5]))
hold on

```

```

for k = 1:length(B)

    boundary = B{k};

    plot(boundary(:,2), boundary(:,1), 'w', 'LineWidth', 1)

end

%determine roundness, size of beam

stats = regionprops(L,'all');

% loop over the boundaries

for k = 1:length(B)

    % obtain (X,Y) boundary coordinates corresponding to label 'k'

    boundary = B{k};

    %3 [calculations and output]

    %get diameter

    di1=max(boundary)-min(boundary);

    diameter_pixelcount=1+max(max(di1));

    waist=min(min(di1));

    diameter_um=diameter_pixelcount*pixelpitch; %convert pixels to um with 30um pixel pitch of
camera

    waist_um=waist*pixelpitch;

    % obtain the area calculation corresponding to label 'k'

    area = stats(k).Area;

    area_um2 = area*(pixelpitch^2)/1e6; %area into mm^2 for 30um pitch xenics

allPerimeters = [stats.Perimeter];

diameter=max(max(allPerimeters))/pi;

Divergence_urad=(diameter_um/f)*es;

minDivergenceurad_waist=lambda/(pi*waist_um);

```

```

% Divergence_mrad=Divergence_urad/1000;

allAreas = [stats.Area];

Circularities = (4 * pi* allAreas)./(allPerimeters .^ 2) ;

% display the results

metric_string = sprintf('roundness=%2.2f',Circularities);

metric_string2 = sprintf('Diameter of whole beam=%2.2f um',diameter_um);

metric_string3 = sprintf('1/e Divergence=%2.2f urad',Divergence_urad);

% metric_string4 = sprintf('1/e Divergence=%2.2f mrad',Divergence_mrad);

metric_string5 = sprintf('Area=%2.2f mm^2',area_um2);

text(10,90,metric_string,'Color','y','FontSize',20,'FontWeight','bold');

text(10,10,metric_string2,'Color','y','FontSize',20,'FontWeight','bold');

text(10,30,metric_string3,'Color','y','FontSize',20,'FontWeight','bold');

% text(10,50,metric_string4,'Color','y','FontSize',14,'FontWeight','bold');

text(10,220,metric_string5,'Color','y','FontSize',20,'FontWeight','bold');

end

```

Appendix 1.2: Matlab 1/e² Divergence and

Roundness Code:

```
%start/input
clear all;
close all;

%inputs
I=double(imread('89.bmp')); %Xenics image file goes here
f=10e3; %mirror focal length in um
pixelpitch=30; %pixel pitch in um for Xenics
es=1-(1/(exp(1)^2)); %(1-1/e^2)
lambda=118.8; %wavelength in um

%%if test needs has RGB data use line below
if size(I,3)==3
I = rgb2gray(I);
end

% normalise:
I=I/(max(max(I)));

%%%%%%%%%%%%%%%%%%%%%%%%%%%%%%%%%%%%%%%%%%%%%%%%%%%%%%%%%%%%%%%%%%%%%%%%script%%%%%%%%%%%%%%%%%%%%%%%%%%%%%%%%%%%%%%%%%%%%%%%%%%%%%%%%%%%%%%%%%%%%%%%%
%%%%%%%%%%%%%%%%%%%%%%%%%%%%%%%%%%%%%%%%%%%%%%%%%%%%%%%%%%%%%%%%%%%%%%%%

%1- [process image]
```

```

%threshold image
bw = imbinarize(I);
imshow(bw)

%%noise removal
% remove all object containing fewer than 30 pixels
bw = bwareaopen(bw,10);

% fill any holes, so that regionprops can be used to estimate
% the area enclosed by each of the boundaries
bw = imfill(bw,'holes');
imshow(bw)

[B,L] = bwboundaries(bw,'noholes');
%find largest element:
[max_size, max_index] = max(cellfun('size', B, 1));
B=B(max_index);

%2 [find boundaries]
% Display the label matrix and draw each boundary
imshow(label2rgb(L, @jet, [.5 .5 .5]))
hold on
for k = 1:length(B)

```

```

boundary = B{k};

plot(boundary(:,2), boundary(:,1), 'w', 'LineWidth', 1)

end

%determine roundness, size of beam

stats = regionprops(L,'all');

% loop over the boundaries

for k = 1:length(B)

    % obtain (X,Y) boundary coordinates corresponding to label 'k'

    boundary = B{k};

    %3 [calculations and output]

    %get diameter

    di1=max(boundary)-min(boundary);

    diameter_pixelcount=1+max(max(di1));

    waist=min(min(di1));

    diameter_um=diameter_pixelcount*pixelpitch; %convert pixels to um with 30um pixel pitch of
camera

    waist_um=waist*pixelpitch;

    % obtain the area calculation corresponding to label 'k'

    area = stats(k).Area;

    area_um2 = area*(pixelpitch^2)/1e6; %area into mm^2 for 30um pitch xenics

allPerimeters = [stats.Perimeter];

diameter=max(max(allPerimeters))/pi;

Divergence_urad=(diameter_um/f)*es;

minDivergenceurad_waist=lambda/(pi*waist_um);

% Divergence_mrad=Divergence_urad/1000;

```

```

allAreas = [stats.Area];

Circularities = (4 * pi* allAreas)./(allPerimeters .^ 2);

% display the results

metric_string = sprintf('roundness=%2.2f',Circularities);

metric_string2 = sprintf('Diameter of whole beam=%2.2f um',diameter_um);

metric_string3 = sprintf('1/e^2 Divergence=%2.2f urad',Divergence_urad);

% metric_string4 = sprintf('1/e Divergence=%2.2f mrad',Divergence_mrad);

metric_string5 = sprintf('Area=%2.2f mm^2',area_um2);

text(10,90,metric_string,'Color','y','FontSize',20,'FontWeight','bold');

text(10,10,metric_string2,'Color','y','FontSize',20,'FontWeight','bold');

text(10,30,metric_string3,'Color','y','FontSize',20,'FontWeight','bold');

% text(10,50,metric_string4,'Color','y','FontSize',14,'FontWeight','bold');

text(10,220,metric_string5,'Color','y','FontSize',20,'FontWeight','bold');

end

```

Appendix 2: UoG Fourier Hologram Sim Matlab

Code

```
%% Reading input bitmap ?le
I0=imread('UG.bmp'); % 256 256 pixels, 8bit image
I0 =double(I0) ; % parameter setup
[c1,r1]=size(I0);
deltax=17e-4; % pixel pitch 0.0038 cm (38 um)
w=118.8e-6; % wavelength 120um
z=15; %distance mm
z=z/3;
% z=r1*deltax^2/w; %distance mm
%Step 1: simulation of propagation
r=5*r1; c=5*c1;
[ C, R]=meshgrid(c, r) ;
I=zeros(c,r);
I(513:768,513:836)=I0;
A0=fftshift(fft2(fftshift(I)));
deltafr=1/5/r1/deltax;
deltafc=1/5/c1/deltax;
p=exp(-2i*pi*z.*((1/w)^2-((R-r1).*deltafr).^2-((C-c1).*deltafc).^2).^0.5);
Az=A0.*p;
EO=fftshift(fft2(fftshift(Az)));
EO=EO(513:768,513:836); % reduce diffraction-plane size

% Step 2: interference at the hologram plane
% zero-padding in the spectrum domain
```

```

Az=fftshift(iff2(fftshift(EO)));
Az2=zeros(4*c1,4*r1);
Az2(85:340,85:408)=Az;
EOf=fftshift(fft2(fftshift(Az2)));
AV=(min(min(abs(EOf)))+max(max(abs(EOf))))/4;
angle=55.3; % reference beam angle;degree
r2=1:4*r1;
c2=1:4*c1;
[ C2, R2]=meshgrid(c2, r2);
Ref=AV*exp(1i*2*pi*sind(angle)*deltax/4.*(R2 -4*r1-1)/w+1i*2*pi*sind(angle)*deltax/4.*(C2-
4*c1-1)/w);
IH=(EOf+Ref).*conj(EOf+Ref);
%IH=IH(257:768,257:904); % reduce the hologram size

%step 3
r3=1:4*r1;
c3=1:4*c1;
[C3 R3]=meshgrid(c3,r3);
THOR=((R3-r1-1).^2+(C3-c1-1).^2).^0.5;
A=THOR.*deltax/4;
QP=exp(1i*pi/w/(1*z).*(A.^2));
FTS=fftshift(fft2(fftshift(IH.*QP)));
I2=FTS.*conj(FTS);
I2=(25*I2)/max(max(I2));
imshow(I2);

```

Appendix 3: Angular Spectrum Hologram

Reconstruction Matlab Code

```
%%%%This code stitches two holograms together to get UoG

%%%% [1] read image file and convert to format Matlab understands %%%%

clear

close all;

holo1=imread('UogHoloPart1.bmp'); %enter your file name here or use this example one

if ndims(holo1)==3

holo1=rgb2gray(holo1);

end

holo1=double(holo1);

%%%% [2] zero pad to avoid aliasing and use zero padded hologram for rest of code%%%%

holo1=holo1/(max(max(holo1)));

%reconstruction

hologram=holo1;

[r,c]=size(hologram);

I=zeros(5*r);

I(513:992,513:1152)=hologram;

hologram=I;

hologram1=I;
```



```

%% Find best dx by looping

dx=15; %distance in mm

dx=dx*30;

d=dx/10000;

%% x and y angles of reference wave for reconstruction, loop for best here too;

thetax = 10; %degrees

thetay = 61; %degrees

%% reference plane wave

ref = exp(1i*2*pi/lambda*x*sin(thetax*pi/180)).*exp(1i*2*pi/lambda*y*sin(thetay*pi/180));

%% [4]compute the Angular Spectrum

FirstFFT =delx*dely*fftshift(fft2(ref.*hologram)); %filter the spectrum to retain only the real or
virtual image of the object

[gux guy]=find(FirstFFT==(max(FirstFFT(:))));%find max peak location of FirstFFT

posx=(nsamplesy/2)-gux;

posy=(nsamplesx/2)-guy;

%% shift and apply circular filter to remove unwanted terms

FirstFFT=wshift('2D',FirstFFT,[round(-posx) round(-posy)]); %shift so 0 order is centred

FirstFFTh1=FirstFFT;

x1 = nsamplesx;

y1 = nsamplesy;

CircFilter = ones(y1,x1);

[xc,yc] = ndgrid(1:y1,1:x1);

%% may need to adjust filter radius size to eliminate zero order

filter_radiansy =180;

CircFilter(sqrt((xc-(nsamplesy/2)).^2+(yc-(nsamplesx/2)).^2) <=(filter_radiansy)) = 0;

FFT_Filter = FirstFFT.*CircFilter; %filter 0 order

```

```

[gux guy]=find(FFT_Filter==(max(FFT_Filter(:))));%find max peak location of FFT with no -
order

posx=(nsamplesy/2)-gux;
posy=(nsamplesx/2)-guy;
FFT_Filter=wshift('2D',FFT_Filter,[round(-posx) round(-posy)]); %shift so real image FFT is
centred

%%% may need to adjust filter radius size to eliminate unwanted noise

filter_radiusy =111;
CircFilter = zeros(y1,x1);
CircFilter(sqrt((xc-(nsamplesy/2)).^2+(yc-(nsamplesx/2)).^2) <=(filter_radiusy)) = 1; %filter
everything except real image

FFT_Filter = FFT_Filter.*CircFilter; %filter 0 order

%%%%% [5] Backpropagate and inverse FFT

%% define back-propagation kernel;
fz = sqrt(1-(lambda.*fx).^2-(lambda.*fy).^2);
propagation = exp(1i*2*pi/lambda/d*real(fz));

%back-propagate the Angular spectrum;
oangspec = FFT_Filter.*propagation;

%inverse FFT to find original object;
reconstruction = (1/delx*1/dely)*ifft2(ifftshift(oangspec));

%amplitude reconstruction
recons = reconstruction.*conj(reconstruction);
Urecons = recons/max(max(recons));
phase = atan2(imag(reconstruction),real(reconstruction));
imshow(3*Urecons)

figure

holo2=imread('UogHoloPart2.bmp'); %enter your file name here or use this example one

```

```

if ndims(holo2)==3
holo2=rgb2gray(holo2);
end
holo2=double(holo2);

%%%%% [2] zero pad to avoid aliasing and use zero padded hologram for rest of code%%%%%

holo2=holo2/(max(max(holo2)));
%reconstruction
hologram=holo2;
[r,c]=size(hologram);
I=zeros(5*r);
I(513:992,513:1152)=hologram;
hologram=I;
hologram1=I;
[r,c]=size(hologram);

%%%%% [3] enter parameters for camera, distance, wavelength and angles%%%%%

%% define wavelength in mm;
pixel_pitch=17e-3;
lambda =118.8e-3;
%% define sampling
nsamplesx = c;
nsamplesy = r;
%physical distance in mm;

```



```

%%%%% [4]compute the Angular Spectrum %%%%%

FirstFFT =delx*dely*fftshift(fft2(ref.*hologram)); %filter the spectrum to retain only the real or
virtual image of the object

[gux guy]=find(FirstFFT==(max(FirstFFT(:))));%find max peak location of FirstFFT

posx=(nsamplesy/2)-gux;
posy=(nsamplesx/2)-guy;

%%%%%shift and apply cicrular filter to remove unwated terms

FirstFFT=wshift('2D',FirstFFT,[round(-posx) round(-posy)]); %shift so 0 order is centred

FirstFFTh1=FirstFFT;

x1 = nsamplesx;
y1 = nsamplesy;

CircFilter = ones(y1,x1);

[xc,yc] = ndgrid(1:y1,1:x1);

%%%%%may need to adjust filter radius size to eliminate zero order

filter_radiusy =180;

CircFilter(sqrt((xc-(nsamplesy/2)).^2+(yc-(nsamplesx/2)).^2) <=(filter_radiusy)) = 0;

FFT_Filter = FirstFFT.*CircFilter; %filter 0 order

[gux guy]=find(FFT_Filter==(max(FFT_Filter(:))));%find max peak location of FFT with no -
order

posx=(nsamplesy/2)-gux;
posy=(nsamplesx/2)-guy;

FFT_Filter=wshift('2D',FFT_Filter,[round(-posx) round(-posy)]); %shift so real image FFT is
centred

%%%%% may need to adjust filter radius size to eliminate unwated noise

filter_radiusy =111;

CircFilter = zeros(y1,x1);

CircFilter(sqrt((xc-(nsamplesy/2)).^2+(yc-(nsamplesx/2)).^2) <=(filter_radiusy)) = 1; %filter
everything except real image

```

```

FFT_Filter = FFT_Filter.*CircFilter; %filter 0 order

%%%%% [5] Backpropagate and inverse FFT
%% define back-propagation kernel;
fz = sqrt(1-(lambda.*fx).^2-(lambda.*fy).^2);
propagation = exp(1i*2*pi/lambda/d*real(fz));
%back-propagate the Angular spectrum;
oangspec = FFT_Filter.*propagation;
%inverse FFT to find original object;
reconstruction = (1/delx*1/dely)*ifft2(ifftshift(oangspec));
%amplitude reconstruction
recons = reconstruction.*conj(reconstruction);
oGrecons = recons/max(max(recons));
phase = atan2(imag(reconstruction),real(reconstruction));
imshow(3*oGrecons)

%%%%%%%%%% [3] stitch U and oG slices together

figure;
reconsAll=oGrecons;
reconsAll(544:1088,909:1252)=Urecons(544:1088,691:1034);
imshow(2*rot90(reconsAll,2));

```

Appendix 4: Real Time Video-Rate Hologram

Reconstruction Matlab Code

```
-%clear;

tic

close all

%initiate parameters

I=single(2400);

I1=zeros(I,'gpuArray'); %5*ypixels

%I=zeros(2400);

[r,c]=size(I1);

%% define wavelength in mm;

lambda =single(118.8e-3);

%% define sampling

nsamplesx = single(c);

nsamplesy = single(r);

%physical distance in mm;

xdistance =1*c*17e-3;

ydistance = 1*r*17e-3;

%physical step size;

delx = xdistance/nsamplesx;

dely = ydistance/nsamplesy;

%define spatial frequency sampling with origin in center;

xsamples = (- (nsamplesx)/2:1:(nsamplesx)/2-1). * xdistance/nsamplesx;

ysamples = (- (nsamplesy)/2:1:(nsamplesy)/2-1). * xdistance/nsamplesx;

fxsamples = (- (nsamplesx)/2:1:(nsamplesx)/2-1). * 1/xdistance;

fysamples = (- (nsamplesy)/2:1:(nsamplesy)/2-1). * 1/ydistance;

[x,y] = meshgrid(xsamples,ysamples);
```

```

[fx,fy] = meshgrid(fxsamples,fysamples);

%% define object - hologram distance

%%%d is around 2-3.5!!!!loop

dx=single(450);

d=dx/10000;

%% x and y angles of reference wave for reconstruction;

thetax = single(51); %degrees

thetay = single(22); %degrees

%% reference plane wave

ref = exp(1i*2*pi/lambda*x*sin(thetax*pi/180)).*exp(1i*2*pi/lambda*y*sin(thetay*pi/180));

%%FFT Filter stuff

x1 = nsamplesx;

y1 = nsamplesy;

CircFilter = ones(y1,x1,'single');

[xc,yc] = ndgrid(1:y1,1:x1);

filter_radiusy =single(220);

CircFilter(sqrt((xc-(nsamplesy/2)).^2+(yc-(nsamplesx/2)).^2) <=(filter_radiusy)) = 0;

filter_radiusy2 =single(77);

CircFilter2 = zeros(y1,x1,'single');

CircFilter2(sqrt((xc-(nsamplesy/2)).^2+(yc-(nsamplesx/2)).^2) <=(filter_radiusy2)) = 1; %filter

everything except real image

con1=filter_radiusy;

con2=filter_radiusy2;

blank_cla=zeros(2*con1+1,'gpuArray');

blank_cla2=zeros(2*con1+1,'gpuArray');

%%FFT CRopping

cropsquarepos=nsamplesx/2;

```

```

%% define back-propagation kernel (inc cropping)

fz = sqrt(1-(lambda.*fx).^2-(lambda.*fy).^2);

cropfz=fz((cropsquarepos-filter_radiusy):(cropsquarepos+filter_radiusy),(cropsquarepos-
filter_radiusy):(cropsquarepos+filter_radiusy));

propagation = exp(1i*2*pi/lambda/d*real(cropfz));

%% Set up webcam

vidObj = VideoReader('RecordedHologramUoG.avi');

vidHeight = single(vidObj.Height);
vidWidth = single(vidObj.Width);

%% Set up video writer

mywriter = VideoWriter('recons.avi','Grayscale AVI');
open(mywriter);

%pause on

s = struct('cdata',zeros(vidHeight,vidWidth,3,'uint8'),...
'colormap',[]);

%% Grab and process frames

k = 2;

while hasFrame(vidObj)

    s(k).cdata = readFrame(vidObj);

```

```

% Acquire frame for processing

img =s(k).cdata ;

% Quantize image by thresholding

holo1=im2single(img);

%holo2=(im2single(img2));

holo1=rgb2gray(holo1);

%holo2=(rgb2gray(holo2));

I1(513:992,513:1152)=holo1;

hologram=I1;

    hologram=hologram/(max(max(hologram)));

%reconstruction

%% compute the Angular Spectrum

FirstFFT =delx*dely*fftshift(fft2(ref.*hologram)); %filter the spectrum to retain only the real or
virtual image of the object

[gux guy]=find(FirstFFT==(max(FirstFFT(:))));%find max peak location of FirstFFT

%posx=(nsamplesy/2)-gux;

%posy=(nsamplesx/2)-guy;

%FirstFFT=wshift('2D',FirstFFT,[round(-posx) round(-posy)]); %shift so 0 order is centred

FirstFFT(gux-con1:gux+con1,guy-con1:guy+con1)=0;

%imagesc(abs(FirstFFT))

%figure

%FFT_Filter=FirstFFT;

%FFT_Filter = FirstFFT.*CircFilter; %filter 0 order

[gux2 guy2]=(find(FirstFFT==(max(FirstFFT(:))));

```

```

%%[gux guy]=find(FFT_Filter==(max(FFT_Filter(:))));%find max peak location of FFT with no -
order
%posx=(nsamplesy/2)-gux;
%posy=(nsamplesx/2)-guy;
%FFT_Filter=wshift('2D',FFT_Filter,[round(-posx) round(-posy)]); %shift so real image FFT is
centred
%FFT_Filter2 = FFT_Filter.*CircFilter2; %filter 0 order
blank_cla(con1-con2:con1+con2,con1-con2:con1+con2)=FirstFFT(gux2-con2:gux2+con2,guy2-
con2:guy2+con2);
%FirstFFT(gux2-con2:gux2+con2,guy2-con2:guy2+con2)=0;
%cropFFT=FirstFFT(gux+(cropsquarepos-
filter_radiusy):gux+(cropsquarepos+filter_radiusy),guy+(cropsquarepos-
filter_radiusy):guy+(cropsquarepos+filter_radiusy));
%figure
%imshow(blank_cla)
gux3=gux+abs(guy2-guy);
guy3=guy+abs(gux2-gux);
%%cropFFT=blank_cla(gux-filter_radiusy:gux+filter_radiusy,guy-
filter_radiusy:guy+filter_radiusy);

oangspec = blank_cla.*propagation;

%inverse FFT to find original object;
reconstruction = (1/delx*1/dely)*ifft2(ifftshift(oangspec));
%amplitude reconstruction
recons = reconstruction.*conj(reconstruction);
%recons = recons/max(max(recons));

```

```
img=3*recons/max(max(recons));
```

```
img=gather(img);
```

```
img=im2uint8(real(img));
```

```
% Write frame to videoclear
```

```
writeVideo(mywriter,(img));
```

```
% writeVideo(mywriter,(img2));
```

```
k = k+1;
```

```
%display(k)
```

```
if k==10000
```

```
    break
```

```
end
```

```
end
```

```
%% Clean up
```

```
%close(mywriter);
```

```
toc
```

```
clear
```

References

1. Vicario, C., Jazbinsek, M., Ovchinnikov, A.V., Chefonov, O.V., Ashitkov, S.I., Agranat, M.B., and Hauri, C.P., (2015). High efficiency THz generation in DSTMS, DAST and OH1 pumped by Cr:forsterite laser. *Optics Express* 23(4)
2. Pawar, A., Sonawane, D., Erande, K. and Derle, D. (2013). Terahertz technology and its applications. *Drug Invention Today*, 5(2), pp.157-163.
3. Bohn, M. and Petkie, D. (2013). Terahertz applications in the aerospace industry. *Handbook of Terahertz Technology for Imaging, Sensing and Communications*, pp.510-546.
4. Tewari, P., Kealey, C., Bennett, D., Bajwa, N., Barnett, K., Singh, R., Culjat, M., Stojadinovic, A., Grundfest, W. and Taylor, Z. (2012). In vivo terahertz imaging of rat skin burns. *Journal of Biomedical Optics*, 17(4), p.040503.
5. D. Jackson, (1953)). The diagnosis of the depth of burning, *Br. J. Surg.*40(164), p588–596
6. Guo, L., Wang, X., Han, P., Sun, W., Feng, S., Ye, J. and Zhang, Y. (2017). Observation of dehydration dynamics in biological tissues with terahertz digital holography [Invited]. *Applied Optics*, 56(13)
7. Castro-Camus, E., Palomar, M. and Covarrubias, A. (2013). Leaf water dynamics of *Arabidopsis thaliana* monitored in-vivo using terahertz time-domain spectroscopy. *Scientific Reports*, 3(1).
8. Baldacci, L., Pagano, M., Masini, L., Toncelli, A., Carelli, G., Storchi, P. and Tredicucci, A. (2017). Non-invasive absolute measurement of leaf water content using terahertz quantum cascade lasers. *Plant Methods*, 13 (1).
9. Santesteban, L., Palacios, I., Miranda, C., Iriarte, J., Royo, J. and Gonzalo, R. (2015). Terahertz time domain spectroscopy allows contactless monitoring of grapevine water status. *Frontiers in Plant Science*, 6.
10. Jordans, C., Rutz, F. and Koch, M. (2006). Quality Assurance of Chocolate Products. ECNDT, 2006- Poster 67.
11. Kawase, K., Shibuya, T., Hayashi, S. and Suizu, K. (2010). THz imaging techniques for nondestructive inspections. *Comptes Rendus Physique*, 11(7-8), pp.510-518.

12. Zimdars, D. and White, J. (2004). Terahertz reflection imaging for package and personnel inspection. *Terahertz for Military and Security Applications II*.
13. Dickinson, J., Goyette, T., Gatesman, A., Joseph, C., Root, Z., Giles, R., Waldman, J. and Nixon, W. (2006). Terahertz imaging of subjects with concealed weapons. *Terahertz for Military and Security Applications IV*.
14. Davies, A., Burnett, A., Fan, W., Linfield, E. and Cunningham, J. (2008). Terahertz spectroscopy of explosives and drugs. *Materials Today*, 11(3), pp.18-26.
15. Appleby, R. and Wallace, H. (2007). Standoff Detection of Weapons and Contraband in the 100 GHz to 1 THz Region. *IEEE Transactions on Antennas and Propagation*, 55(11), pp.2944-2956.
16. . Strachan, C. J., Taday, P. F., Newnham, D. A., Gordon, K. C., Zeitler, J., Pepper, M., & Rades, T. (2005). Using Terahertz Pulsed Spectroscopy to Quantify Pharmaceutical Polymorphism and Crystallinity. *J. Pharma Sci*, 94(4), 837-846.
17. Baker, C., Lo, T., Tribe, W. R., Cole, B. E., Hogbin, M. R., & Kemp, M. C. (2007). Detection of Concealed Explosives at a Distance Using Terahertz Technology. *Proceedings of the IEEE*, 95(8), 1559-1565
18. Liu, J., Fan, W., Chen, X., & Xie, J. (2016). Identification of high explosive RDX using terahertz imaging and spectral fingerprints. *J. Physics: Conference Series*, 680, 012030.
19. Rees, W. (2012). Introduction. *Physical Principles of Remote Sensing*, pp.1-10,
20. <https://www.microscopyu.com/techniques/super-resolution/the-diffraction-barrier-in-optical-microscopy> [online], [Accessed 18 Dec. 2018].
21. Vangindertael, J., Camacho, R., Sempels, W Mizuno, H., Dedecker, P., Janssen, K.P.F (2018). An introduction to optical super-resolution microscopy for the adventurous biologist. *Methods Appl. Fluoresc.* 6 022003
22. Zhang, X., Xu, J. (2018). Near-field imaging of graphene triangles patterned by helium ion lithography. *Nanotechnology*, 29, Number 38
23. Vicidomini, G., Bianchini, P., Diaspro, A. (2018). STED super-resolved microscopy. *Nature Methods* 15 173

24. Sizov, F. (2018). Terahertz radiation detectors: the state-of-the-art. *Semiconductor Science and Technology*, Volume 33, Number 12
25. Weishaupt D., Köchli V.D., Marincek B. (2003) Factors Affecting the Signal-to-Noise Ratio. In: *How does MRI work?*. Springer, Berlin, Heidelberg
26. May, T., Zieger, G., Anders, S., Zakosarenko, V., Starkloff, M., Meyer, H.G., Thorwirth, G. and Kreysa, E. (2008). Passive stand-off Terahertz imaging with 1 Hertz frame rate, *Proc. SPIE, Terahertz Mil. Secur. Appl. VI*, vol. 6949, pp. 69490C–1–8
27. Withington, S. (2004). Terahertz astronomical telescopes and instrumentation. *Philosophical Transactions of the Royal Society A: Mathematical, Physical and Engineering Sciences*, 362(1815), pp.395-402.
28. May, T., Meyer, H.G., and Popp, J. (2010). *Candid Cameras*, SPIE Professional
29. Karpowicz, N., Zhong, H., Xu, J., Lin, K., Hwang, J. and Zhang, X. (2005). Comparison between pulsed terahertz time-domain imaging and continuous wave terahertz imaging. *Semiconductor Science and Technology*, 20(7), pp.S293-S299.
30. Naftaly, M. and Miles, R. (2005). Terahertz time-domain spectroscopy: A new tool for the study of glasses in the far infrared. *Journal of Non-Crystalline Solids*, 351(40-42), pp.3341-3346.
31. Lee, A. and Hu, Q. (2005). Real-time, continuous-wave terahertz imaging by use of a microbolometer focal-plane array. *Optics Letters*, 30(19), p.2563.
32. Williams, B. (2007). Terahertz quantum-cascade lasers. *Nature Photonics*, 1(9), pp.517-525.
33. Degl'Innocenti, R., Shah, Y., Wallis, R., Klimont, A., Ren, Y., Jessop, D., Beere, H. and Ritchie, D. (2015). A hybrid plasmonic waveguide terahertz quantum cascade laser. *Appl. Phys. Lett.*, 106(8), p.082101
34. Sirkeli, V., Yilmazoglu, O., Küppers, F. and Hartnagel, H. (2017). Room-temperature terahertz emission from ZnSe-based quantum cascade structures: A simulation study. *physica status solidi (RRL) - Rapid Research Letters*, 11(3), p.1600423.
35. Chan, C. (2015). *Towards room-temperature Terahertz Quantum Cascade Lasers : directions and design*. [online] Hdl.handle.net. Available at: <http://hdl.handle.net/1721.1/97258> [Accessed 18 Dec. 2018].

36. Maestrini, A., Thomas, B., Wang, H., Jung, C., Treuttel, J., Jin, Y., Chattopadhyay, G., Mehdi, I. and Beaudin, G. (2010). Schottky diode-based terahertz frequency multipliers and mixers. *Comptes Rendus Physique*, 11(7-8), pp.480-495.
37. D. Pardo, J. Grajal, C. G. Pérez-Moreno, and S. Pérez, "An Assessment of Available Models for the Design of Schottky-Based Multipliers Up to THz Frequencies," *IEEE Trans. Terahertz Sci. Technol.*, vol. 4, no. 2, pp. 277–287, 2014.
38. Mehdi, I., Siles, J., Lee, C. and Schlecht, E. (2017). THz Diode Technology: Status, Prospects, and Applications. *Proceedings of the IEEE*, 105(6), pp.990-1007.
39. Mueller, E. (2016). Optically Pumped Terahertz (THz) Lasers. *Wiley Encyclopedia of Electrical and Electronics Engineering*, pp.1-22.
40. Siegel, P. (2014). Terahertz Pioneers: A Series of Interviews With Significant Contributors to Terahertz Science and Technology. *IEEE Transactions on Terahertz Science and Technology*, 4(4), pp.409-409.
41. Griffiths, P.R. and de Haseth, J.A., (1986). 'Fourier Transform Infrared Spectrometry', Wiley Interscience, New York, 209–212
42. Golay, M. (1947). Theoretical Consideration in Heat and Infra-Red Detection, with Particular Reference to the Pneumatic Detector. *Review of Scientific Instruments*, 18(5), pp.347-356.
43. Sun, J. (2016). Field-effect Self-mixing Terahertz Detectors. Ch 1.3 THz Detectors, Springer
44. Dooley, D., (2010). Sensitivity of broadband pyroelectric terahertz detectors continues to improve., *Laser Focus World*, vol. 46, no. 5, pp. 49–53
45. Saeedkia, D. (2013). Handbook of terahertz technology for imaging, sensing and communications. Ch8.7 Overview of Other Focal-Plane Technologies for Terahertz Imaging, Oxford, England: WP Woodhead Publishing.
46. Pandya, S., Wilbur, J., Kim, J., Gao, R., Dasgupta, A., Dames, C. and Martin, L. (2018). Pyroelectric energy conversion with large energy and power density in relaxor ferroelectric thin films. *Nature Materials*, 17(5), pp.432-438.
47. <https://www.ophiropt.com/laser--measurement/beam-profilers/products/Beam-Profiling/Camera-Profiling-with-BeamGage/Pyrocam-IIIHR> [online], [Accessed 18 Dec. 2018].

48. Knap, W., Dyakonov, M., Coquillat, D., Teppe, F., Dyakonova, N., Łusakowski, J., Karpierz, K., Sakowicz, M., Valusis, G., Seliuta, D., Kasalynas, I., Fatimy, A., Meziani, Y. and Otsuji, T. (2009). Field Effect Transistors for Terahertz Detection: Physics and First Imaging Applications. *Journal of Infrared, Millimeter, and Terahertz Waves*.
49. Lisauskas, A., Boppel, S., Krozer, V. and Roskos, H. (2011). Silicon CMOS-based THz detection. *2011 IEEE SENSORS Proceedings*.
50. Hou, H., Liu, Z., Teng, J., Palacios, T. and Chua, S. (2017). High Temperature Terahertz Detectors Realized by a GaN High Electron Mobility Transistor. *Scientific Reports*, 7(1).
51. Suzuki, D., Oda, S. and Kawano, Y. (2013). GaAs/AlGaAs field-effect transistor for tunable terahertz detection and spectroscopy with built-in signal modulation. *Applied Physics Letters*, 102(12), p.122102.
52. Hack, E., Valzania, L., Gäumann, G., Shalaby, M., Hauri, C. and Zolliker, P. (2016). Comparison of Thermal Detector Arrays for Off-Axis THz Holography and Real-Time THz Imaging. *Sensors*, 16(2), p.221.
53. <https://www.flir.co.uk/products/tau-2/> [online], [Accessed 18 Dec. 2018].
54. <http://www.xenics.com/en/camera/gobi-640-series> [online], [Accessed 18 Dec. 2018].
55. <http://thruvision.com/products/ts4-c/> [online], [Accessed 18 Dec. 2018].
56. <https://cordis.europa.eu/project/rcn/111494/reporting/en?rcn=231593> [online], [Accessed 18 Dec. 2018].
57. Simoens, F., Dussopt, L., Meilhan, J., Nicolas, J., Monnier, N., Siligaris, A., Hiberty, B., Perraud, J., Mounaix, P., Lalanne-Dera, J. and Redon, O. (2018). Towards industrial applications of terahertz real-time imaging. *Terahertz, RF, Millimeter, and Submillimeter-Wave Technology and Applications XI*.
58. <https://www.i2s.fr/en/product/tzcam> [online], [Accessed 18 Dec. 2018].
59. J. Peatross and M. Ware, (2015). *Physics of Light and Optics*, Chapter 10
60. Chartier, G. (2005). *Introduction to Optics. Ch2 Electromagnetic Waves* New York, NY: Springer Science+Business Media, Inc.
61. <http://quantumhertz.com/index.php/home/hsc-physics-space/a-brief-history-of-light/> [online], [Accessed 18 Dec. 2018].

62. R.P. Feynman, R.B. Leighton, and M. Sands, The Feynman Lectures on Physics, Vol1: Mainly Mechanics, Radiation, and Heat first edition, Addison-Wesley Longman, Inc., Boston, MA (1977).
63. Pedrotti, L. (n.d.), (2008). Ch 4 Basic Physical Optics. Fundamentals of Photonics, pp.117-168, SPIE
64. Bass, M., Enoch, J. and Lakshminarayanan, V. (2010). Handbook of optics. New York: McGraw-Hill. Ch 5- Coherence Theory
65. Tikhonov, E. (2015). Measurement of radiation coherence by means of interference visibility in the reflected light. physics.optics.
66. Young, T. (1802). The Bakerian Lecture: On the Theory of Light and Colours Philosophical Transactions of the Royal Society of London Vol. 92
67. Gabor, D. (1946). Theory of Communication. Journal of Institution of Electrical Engineers, Vol. 93, No. 3, pp. 429-457.
68. Ratan, Akshay. (2015). Holography - Working Principle and Applications. 10.13140/RG.2.1.2688.4649.
69. Leith, E. and Upatnieks, J. (1962). Reconstructed Wavefronts and Communication Theory*. Journal of the Optical Society of America, 52(10), p.1123.
70. Goodman J. W., Introduction to Fourier Optics, [2^a ed.], McGraw-Hill (1996).
71. M. S. Heimbeck, M. K. Kim, D. A Gregory and H. O. Everitt, (2011). Terahertz digital holography using angular spectrum and dual wavelength reconstruction methods, Opt. Express 19(10), 9192
72. Q. Deng, W. Li, X. Wang, Z. Li, H. Huang, C. Shen and R. Zou, (2017). High-resolution terahertz inline digital holography based on quantum cascade laser, Optical Engineering 56(11), 113102
73. Poon, T. and Liu, J. (2013). Introduction to Modern Digital Holography.
74. Rong, L., Latychevskaia, T., Chen, C., Wang, D., Yu, Z., Zhou, X., Li, Z., Huang, H., Wang, Y., Zhou, Z. (2015). TI - Terahertz in-line digital holography of human hepatocellular carcinoma tissue Sci. Reports 5 8445

75. Locatelli, M. Ravaro, M. Bartalini, S. Consolino, L. Vitiello, M. S. Cicchi, R. and De Natale, P. (2015). Real-time terahertz digital holography with a quantum cascade laser, *Sci. Reports* 5(1) 13566
76. Pedrotti, L. (n.d.). *Basic Physical Optics. Fundamentals of Photonics*, pp.117-168.
77. Zuo, J. and Spence, J. (2017). *Advanced Transmission Electron Microscopy. Ch 2- Electron Waves and Wave Propagation*, New York, NY: Springer.
78. Born, M. and Wolf, E. (1999). *Principles of optics, Ch 8- Elements of Theory of Diffraction*, Cambridge: Cambridge University Press.
79. Schmidhammer, U. and Jeunesse, P. (2014). Pulsed THz imaging for non-destructive testing of adhesive bonds. 2014 39th International Conference on Infrared, Millimeter, and Terahertz waves (IRMMW-THz).
80. Taylor, Z., Singh, R., Brown, E., Bjarnason, J., Hanson, M. and Gossard, A. (2009). Analysis of Pulsed THz Imaging Using Optical Character Recognition. *IEEE Sensors Journal*, 9(1), pp.3-8.
81. Sun, Y. (2011). A promising diagnostic method: Terahertz pulsed imaging and spectroscopy. *World Journal of Radiology*, 3(3), p.55.
82. <https://www.edinst.com/us/products/295-stand-alone-fir-laser/> [online], [Accessed 18 Dec. 2018].
83. Scheps, R. (2002). *Introduction to laser diode-pumped solid state lasers, Ch 2.3 Laser resonator transverse modes* Bellingham, Wash.: SPIE Press.
84. http://enacademic.com/pictures/enwiki/76/Laser_gaussian_profile.svg
85. <http://www.uslasercorp.com/envoy/diverge.html> [online], [Accessed 18 Dec. 2018].
86. Schulmeister, K., Gilber, R., Edthofer, F., Seiser, B. and Veas, G. (2006). Comparison of different beam diameter definitions to characterize thermal damage of the eye. *Laser Beam Control and Applications*.
87. Picart, P. and Leval, J. (2008). General theoretical formulation of image formation in digital Fresnel holography. *Journal of the Optical Society of America A*, 25(7), p.1744.
88. Kruse, P.W. *Uncooled Thermal Imaging: Arrays, Systems, and Applications*; SPIE Press: Bellingham, WA, USA, 2001

89. Hack, E., Valzania, L., Gäumann, G., Shalaby, M., Hauri, C. and Zolliker, P. (2016). Comparison of Thermal Detector Arrays for Off-Axis THz Holography and Real-Time THz Imaging. *Sensors*, 16(2), p.221.
90. http://www.tydexoptics.com/products/thz_optics/thz_beam_splitter/ [online], [Accessed 18 Dec. 2018].
91. Roggenbuck, A., Schmitz, H., Deninger, A., Mayorga, I., Hemberger, J., Güsten, R. and Grüninger, M. (2010). Coherent broadband continuous-wave terahertz spectroscopy on solid-state samples. *New Journal of Physics*, 12(4), p.043017.
92. Poon, T. and Liu, J. (2013). Introduction to Modern Digital Holography.
93. Yu, L., Cai, L., (2001). Iterative algorithm with a constraint condition for numerical reconstruction of a three-dimensional object from its hologram. *Journal of the Optical Society of America A*, 18(5)
94. Bilinskis, I. (2007). Digital Alias-free Signal Processing
95. Qiu, P. (2017). The feasibility of automatic focusing in digital holography by using Fresnel transform as numerical holographic reconstruction algorithm, *Optik*, Volume 137,
96. Boreman, G. (2001). Modulation transfer function in optical end electro-optical systems. Bellingham, Washington: SPIE Optical Engineering Press.
97. Boreman, G. and Yang, S. (1995). Modulation Transfer Function Measurement Using Three- and Four-bar Targets. *Applied Optics*, 34(34), p.8050.
98. Girshovitz, P. and Shaked, N. (2014). Real-time quantitative phase reconstruction in off-axis digital holography using multiplexing. *Optics Letters*, 39(8), p.2262.
99. D'Angelo, F., Mics, Z., Bonn, M., and Turchinovich, D. (2014). "Ultra-broadband THz time-domain spectroscopy of common polymers using THz air photonics," *Opt. Express* 22, 12475-12485
100. Jin, Y., Kim, G.J., & Jeon, S.G. (2006). 'Terahertz dielectric properties of polymers'. *Journal of the Korean Physical Society*, 49(2), 513-517.
101. Wietzke, S., Rutz, F., Jördens, C., K, N., Vieweg, N., Jansen, C., Wilk, R., Koch, M. (2008). Applications of terahertz spectroscopy in the plastics industry - art. no. 68400V. *Proceedings of SPIE - The International Society for Optical Engineering*. 6840.

102. Valzania L, Zolliker P, Hack, E. (2017), 'Topography of hidden objects using THz digital holography with multi-beam interferences', *Optics Express*, Issue 10, pp. 11038-11047 (2017)
103. Treviño-Palacios, C. (2015). Unfolding wrapped phase. *Optical Engineering*, 54(11), p.110503.
104. Wagner, C. (2000). Direct shape measurement by digital wavefront reconstruction and multiwavelength contouring. *Optical Engineering*, 39(1), p.79.
105. Martinez-Carranza, J., Falaggis, K. and Kozacki, T. (2017). Fast and accurate phase-unwrapping algorithm based on the transport of intensity equation. *Applied Optics*, 56(25), p.7079.
106. Meneses, J., Gharbi, T. and Humbert, P. (2005). Phase-unwrapping algorithm for images with high noise content based on a local histogram. *Applied Optics*, 44(7), p.1207.
107. Fang, S., Meng, L., Wang, L., Yang, P. and Komori, M. (2011). Quality-guided phase unwrapping algorithm based on reliability evaluation. *Applied Optics*, 50(28), p.5446.
108. Asundi, A. (2013). Digital holography for mems and microsystem metrology. Ch 3.3.3 *Common-Path Digital Holographic Microscope*, Hoboken, N.J.: Wiley.